Solid solution strengthening and texture evolution in Mg-Y alloys

SOLID SOLUTION STRENGTHENING AND TEXTURE EVOLUTION IN MG-Y ALLOYS

BY

XIAOHUI JIA, B.Eng.

A THESIS

SUBMITTED TO THE DEPARTMENT OF MATERIALS SCIENCE AND ENGINEERING

AND THE SCHOOL OF GRADUATE STUDIES

OF MCMASTER UNIVERSITY

IN PARTIAL FULFILMENT OF THE REQUIREMENTS

FOR THE DEGREE OF

MASTER OF APPLIED SCIENCE

Master of Applied Science (2013) McMaster University

(Materials Science and Engineering) Hamilton, Ontario, Canada

TITLE:	Solid solution strengthening and texture evolution in Mg-Y alloys
AUTHOR:	Xiaohui Jia B.Eng, (Materials Science and Engineering) McMaster University, Hamilton, Canada
SUPERVISOR:	Dr. Marek Niewczas
NUMBER OF PAGES:	xv, 124

To my family and friends

Abstract

Tension and compression experiments have been carried out on a series of Mg-Y alloys with Y content up to 1.3 at. %, in a range of temperatures between 4.2K and 298K, to study the effect of Yttrium on mechanical properties and strain hardening. The alloys show strong difference in the hardening behavior under tension and compression attributed to the effect of texture. The yield strength scales with concentration of the solute as c^n, where c is the concentration of the solute in atomic percent and n$\sim$2/3. The results suggest that in addition to the atomic size and modulus misfit effects, the valence effect and prismatic slip system strengthening may be responsible for the enhanced strengthening of Y in Mg. Strain rate sensitivity measurements carried out under tension and compression reveal that Mg-Y alloys show decreasing SRS with increasing Y content at 298K and exhibit a negative SRS in highly concentrated alloys, which may be attributed to dynamic strain aging. At low temperatures the alloys show positive SRS increased with Y content. Texture measurements suggest that increasing Y content in alloys decreases the amount of basal component and enhances non-basal orientations. The reduced yield asymmetry between tension and compression observed in higher Y content alloys is being attributed to the weakening of the basal texture. The fracture mode shows dependence on deformation temperature. At 298K and 78K the failure is a mixture of ductile and cleavage type which is dominated by ductile and cleavage, respectively. At 4K, failure occurs predominantly by cleavage fracture.

Acknowledgements

First of all, the author would like to express her deepest gratitude and appreciation to her supervisor, Dr. Marek Niewczas, for his constant encouragement, guidance, patience in experiments training and valuable discussion throughout this master research work.

The author extends her heartiest thanks to Dr. Anna Kula, the Postdoctoral fellow in Dr.Niewczas group. Without her help during material production, tensile and compressive testing and sample polishing, this research work could not have ran smoothly. The author also appreciated her guidance and valuable discussion.

The author gratefully appreciated the assistance of Dr. Jim Britten and Victoria Jarvis in X-Ray measurements, software support and data analysis support. Their valuable discussions and basic knowledge tutorials deeply impressed the author and extended her knowledge on XRD analysis.

Special thanks are due to all of the technicians in Materials Science and Engineering department, who gave the author a substantial mount of experimental trainings and supports.

Last, but not the least, the author wish to thank her family and friends for their encouragement and understanding.

The author would like to thank all of the people mentioned or not mentioned here and she would like to dedicate this thesis to all of them.

Contents

List of Tables

List of Figures

Chapter 1

Introduction

1.1 Objective

Magnesium alloys are attractive materials for weight-sensitive applications in automotive and aerospace industries. The application of die-cast magnesium alloys is widespread, while the application of wrought magnesium alloys as structural materials is hindered by their poor room temperature formability. Consequently, there is extensive research going into wrought magnesium alloys containing rare earth elements (REs). Mg-RE alloys such as Mg-Gd alloys and Mg-Nd alloys exhibit better mechanical properties with respect to Mg alloys containing aluminum or zinc. Yttrium (Y) is considered to be one of the most effective rare earth elements to improve mechanical properties of Mg alloys. It is commonly believed that Y is an effective solid solution hardener and recrystallization texture modifier. Y has already been used as alloying element in a number of commercial alloys with high strength. However, it has not been very clear as to how Y element affects the mechanical properties of magnesium alloys during alloy processing and during application of a final product. Consequently, it is important to investigate the effect of Y on mechanical

properties of magnesium alloys and understand the deformation mechanisms. It has been reported that Mg-Y alloys show significantly enhanced room temperature ductility and increased strength with the increase of Y addition, compared to pure Mg and other classes of Mg-based wrought alloys. In the case of low-temperature deformation of Mg-Y alloys, no theoretical or experimental explanation has been available on the effect of Y on these properties. The objectives of the present research are: (i) to develop a better understanding of mechanical properties and deformation behavior in a series of Mg-Y alloys between 4K and 298K, (ii) to determine, in a qualitative way, the solid solution strengthening effect of Y in Mg-Y solid solutions (iii) to investigate texture evolution during tensile and compressive deformation in Mg-Y alloys (iv) to study fundamental mechanisms that control plastic flow and the asymmetry of the deformation behavior under tension and compression and (v) to understand the effect of temperature on mechanical properties of Mg-Y solid solutions between 4K and 298K.

1.2 Magnesium-Yttrium alloy

The Mg-Y based alloys are being developed as light structural materials with high strength at ambient and elevated temperatures, up to 575K. The alloys with Y show the highest strength at room temperature among other Mg-RE alloys containing cerium, lanthanum, praseodymium, thorium and neodymium (L.L.Rokhlin, 2003). This effect is believed to be connected to the Mg-Y phase diagram showing limited solubility of Y in solid Mg (Figure 1.1). As can be seen the solubility of Y decreases with decreasing temperature.

The Mg-Y phase diagram is depicted in Figure 1.1a. There are three binary compounds in the Mg-Y phase diagram, $Mg_{24}Y_5$, Mg_2Y and MgY. The Mg-rich side of the Mg-Y phase

diagram is depicted in Figure 1.1b according to the results of the Baikow Institute of Metallurgy (L.L.Rokhlin, 2003). The maximum solubility of Y in the solid solution with Mg occurs at the eutectic temperature of 565°C and at a composition of approximately 12.0 mass % (3.59 at. %). The solubility of Y decreases with decreasing temperature and at room temperature, about 7.0 mass % (2.02 at. %) remains in the solid solution (R.Muraliraja *et al.*, 2013).

A number of commercial magnesium alloys containing rare earth elements have been produced and used in industry for a long time. The alloy WE54A, containing Y as the dominant alloying element, is one of the latest Mg cast alloys. High strength at elevated temperature is the major advantage of WE54A alloy. Alloys from a group of WE43 were also developed and tried for industrial application. A series of new wrought magnesium alloys containing rare earth elements were developed in Russia for commercial applications, which are named IMV5, IMV6, IMV7 and IMV8. Y is the main alloying element in all alloys (L.L.Rokhlin, 2003).

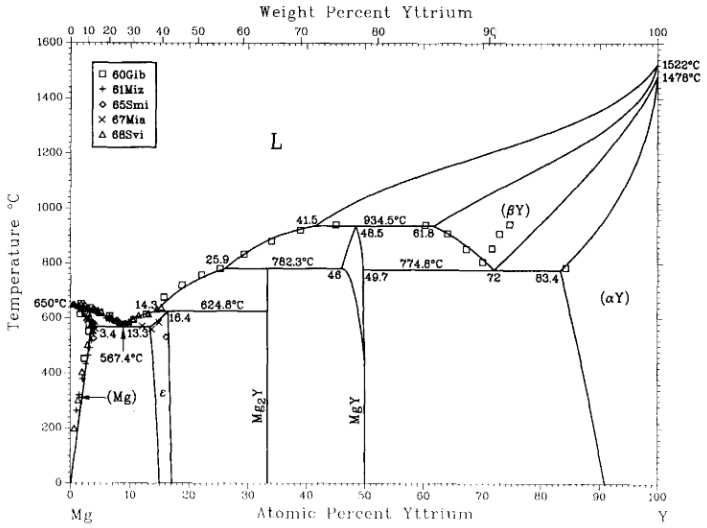

(a)

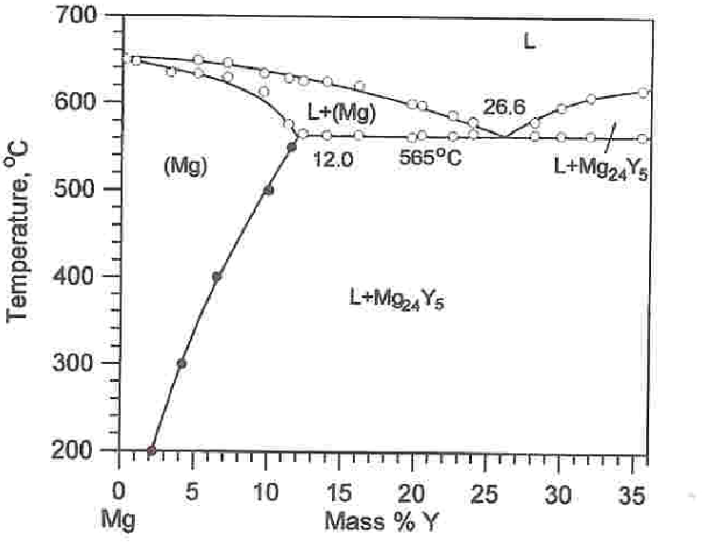

(b)

Figure 1.1: (a) Mg-Y phase diagram, (b) Mg-rich side of Mg-Y phase diagram.

1.3 Deformation mechanism

Deformation of magnesium and magnesium alloys at room temperature occurs by crystallographic slip and twinning. Mechanical properties of these alloys are significantly impacted by the interactions of these two mechanisms. Figure 1.2 shows four common slip systems for magnesium: basal <a> slip $\{0001\}$ $<11\bar{2}0>$, prismatic <a> slip $\{1\bar{1}01\}$ $<11\bar{2}0>$, 1^{st} order pyramidal <c+a> slip $\{1\bar{1}01\}$ $<\bar{1}2\bar{1}3>$ and 2^{nd} order pyramidal <c+a> slip $\{11\bar{2}2\}$ $<11\bar{2}\bar{3}>$. Crystallographic characteristics of these slip systems in Mg are summarized in Table 1.1.

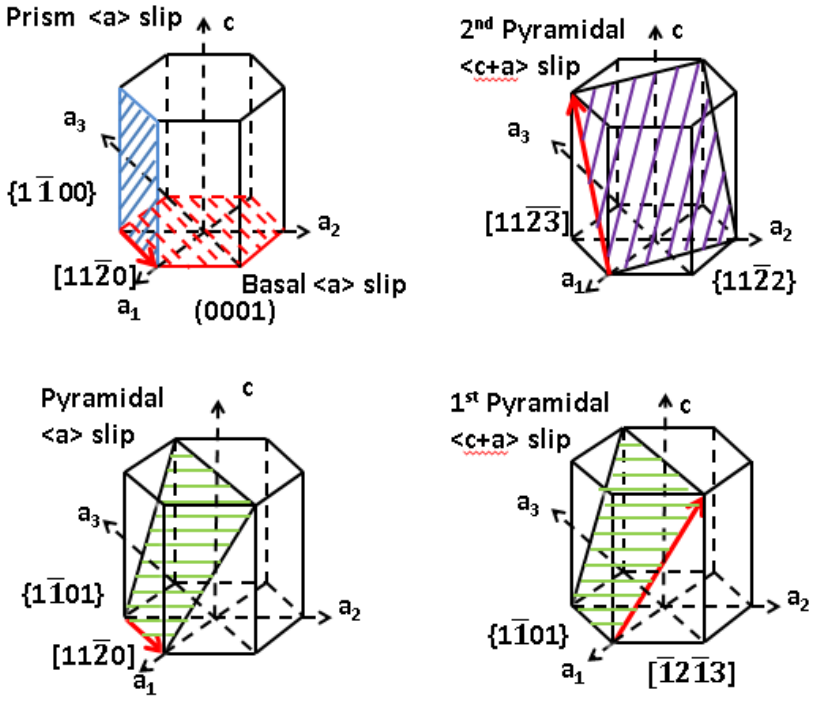

Figure 1.2: Crystallographic planes and directions for different slip systems in Mg.

Table 1.1: Crystallographic characteristics of slip systems in Mg

Slip plane	Slip direction	Crystallographic description	Number of independent slip systems
Basal	<a>	$\{0001\}<11\bar{2}0>$	2
Prismatic	<a>	$\{1\bar{1}01\}<11\bar{2}0>$	2
Pyramidal	<a>	$\{1\bar{1}01\}<11\bar{2}0>$	4
Pyramidal, 1^{st} order	<c+a>	$\{1\bar{1}01\}<\bar{1}2\bar{1}3>$	5
Pyramidal, 2^{nd} order	<c+a>	$\{11\bar{2}2\}<11\bar{2}\bar{3}>$	5

Figure 1.3 shows the temperature dependence of the critical resolved shear stress (CRSS) for basal <a> slip, prismatic <a> slip and 2^{nd} order pyramidal <c+a> slip in magnesium. At room temperature, basal slip is the dominant deformation mechanism due to its low CRSS. The CRSS of the non-basal slip systems, prismatic and pyramidal slip, is almost a hundredfold greater than that of basal slip, but these slip modes can also be activated as secondary slip under some conditions.

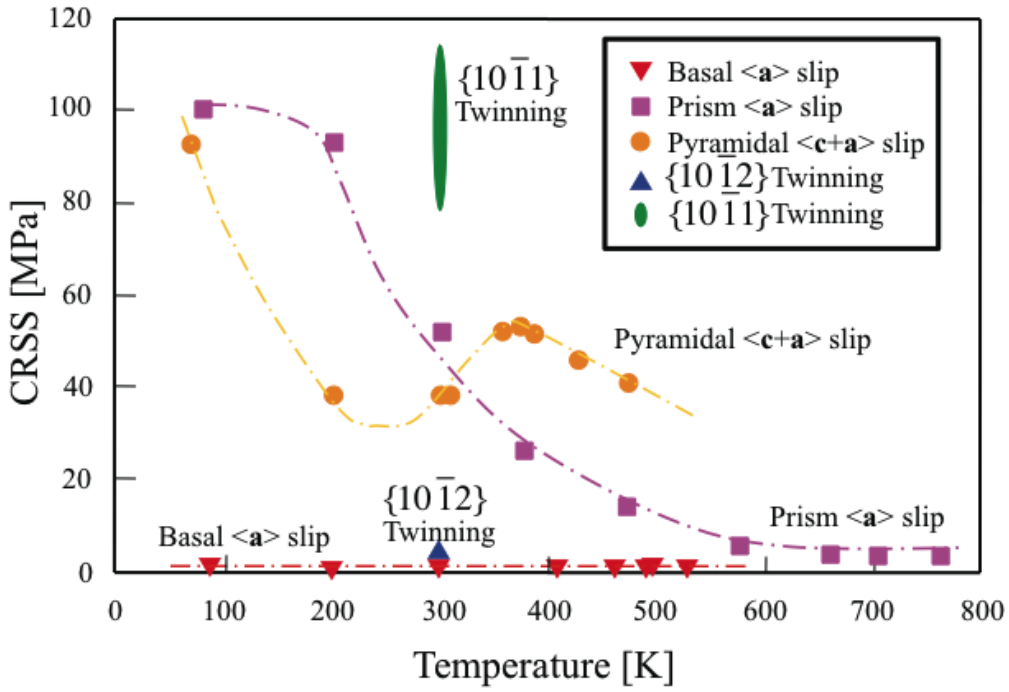

Figure 1.3: CRSS for Slip and Twinning Systems in Magnesium. Image provided by Fumiaki Hiura (F. Hiura, Master Thesis, McMaster University, 2008).

Table 1.2: Crystallographic characteristics of twinning modes in Mg

Twin type	Crystallographic description	Strain along c-axis	Rotation about $<11\bar{2}0>$ (deg.)
Single	$\{10\bar{1}2\}$ $<\bar{1}011>$	Extension	86
Single	$\{10\bar{1}1\}$ $<10\bar{1}\bar{2}>$	Contraction	56
Single	$\{10\bar{1}3\}$	Contraction	64
Double	$\{10\bar{1}1\}$-$<10\bar{1}2>$	Contraction	38
Double	$\{10\bar{1}3\}$-$<10\bar{1}2>$	Contraction	22

Due to the limited number of slip systems in magnesium, twinning is an important deformation mode to accommodate deformation along c-axis of hcp lattice. Crystallographic characteristics of twinning in pure Mg and its alloys are summarized in Table 1.2.

In magnesium and magnesium alloys, two types of twins are most commonly observed: Tension twin $\{10\bar{1}2\}$ and Compression twin $\{10\bar{1}1\}$. They are also called extension twin and contraction twin, respectively, because they result in the extension and the contraction of the crystal along the crystallographic c-axis of the unit cell. Tension twin should be formed when a tensile stress is applied along c-axis and Compression twin should be formed when a compressive stress is applied along c-axis (Figure 1.4).

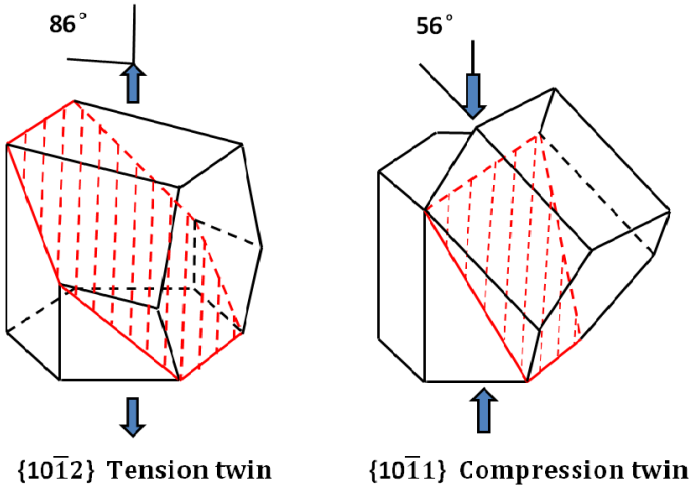

Figure 1.4: Schematic representation of Tension and Compression twin in magnesium.

1.4 Solid solution strengthening behavior

Mott and Nabarro (N.F.Mott & F.R.N.Nabarro, 1940) proposed a theory which attributes the average magnitude of the stress in the matrix of a dilute solid solution to the size misfit induced by the lager or smaller solute atoms. However, this theory does not include the interaction of screw dislocation with solute atoms and does not agree with experimental results. Fleischer (R.L.Fleischer., 1961, 1963) proposed another mechanism of solution hardening, modulus misfit. Fleischer assumed that every individual atom may induce a small elastically deformed region, where the solute atom results in hard or soft spots in the matrix. These regions act as obstacles to dislocation glide, both screw and edge dislocations. Labusch (R.Labusch, 1970) proposed another theory, which is similar to Fleischer's theory.

The relationship of alloying concentration and yield stress can be expressed as described by Fleischer (R.L.Fleischer., 1961, 1963)

$$\sigma_{ys} = \sigma_0 + Z_F G(|\delta| + \beta\,|\eta|)^{3/2} c^{1/2} \tag{1.1}$$

or according to Labusch (R.Labusch, 1970)

$$\sigma_{ys} = \sigma_0 + Z_L G(\delta^2 + \beta^2 \eta^2)^{2/3} c^{2/3} \tag{1.2}$$

Akhtar and Teghtsoonian (A.Akhtar & E.Teghtsoonian, 1969a,b) investigated the solid solution strengthening of both basal slip and prismatic slip using magnesium single crystals. Figure 1.5 shows that the CRSS of basal slip remains independent of alloying element up to 0.025 at. % Zn and then increases with $c^{1/2}$. Two linear stages are observed in Figure 1.5. The transition point, which is independent of temperature, is at 0.025 at. % Zn. The

slope of stage II is almost three fold higher than stage I. Akhtar and Teghtsoonian proposed that the increase in the forest dislocation density with solute content and the change in the thermally activated mechanism occurs from intersection to single solute atom dislocation pinning mechanism, are the reason for stage I and stage II, respectively. Figure 1.6 and Figure 1.7 show that at low temperatures the CRSS of prismatic slip decreases with solute concentration. At higher temperatures, the CRSS increases by a small amount with solute content, followed by a decrease as the solute content increases. They proposed that the increase in the athermal component and the decrease in the thermally activated component of the flow stress with solute content are the reasons for the observation. Cáceres et al., (C.H.Cáceres & D.M.Rovera, 2001; C.H.Cáceres & A.Blake, 2002) have studied the solid solution strengthening of Mg-Al and Mg-Zn alloys using polycrystalline magnesium alloys. For Mg-Al alloys (Al content between 0.87 and 7.44 at.%), proof strength increases linearly with c^n, where n =1/2 or 2/3. The results, which are consistent with Akhtar and Teghtsoonian's basal slip study for dilute Mg-Al single crystal alloy, suggest that basal slip strengthening dominates the solid solution strengthening in Mg-Al alloys. For Mg-Zn alloy (Zn contents between 0.21 and 2.66 at.%), proof strength does not change significantly with Zn additions up to 0.7 at.% Zn, followed by higher strengthening rate. They attributed the increasing strengthening rate to the formation of regions of short-range order during the solution heat treatment of the alloy. Stanford and Barnett (N.Stanford & M.R.Barnett, 2013) studied the solute strengthening of prismatic slip, basal slip and $\{10\bar{1}2\}$ twinning in Mg and Mg-Zn alloys. They observed solute softening of prismatic slip for grain sizes above 50 μm, while the CRSS of prismatic slip increases with Zn contents below this grain size. They also concluded that the activation stress of $\{10\bar{1}2\}$ twinning is independent of Zn content and the activation stress of basal slip increases with the reduction of grain size.

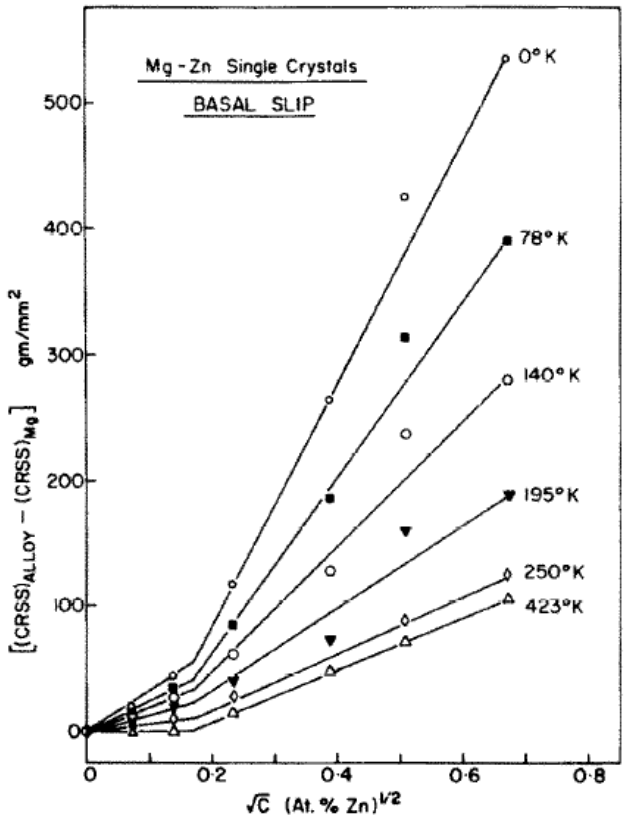

Figure 1.5: CRSS versus $c^{1/2}$ for Mg-Zn single crystals at different temperatures (A.Akhtar & E.Teghtsoonian, 1969a).

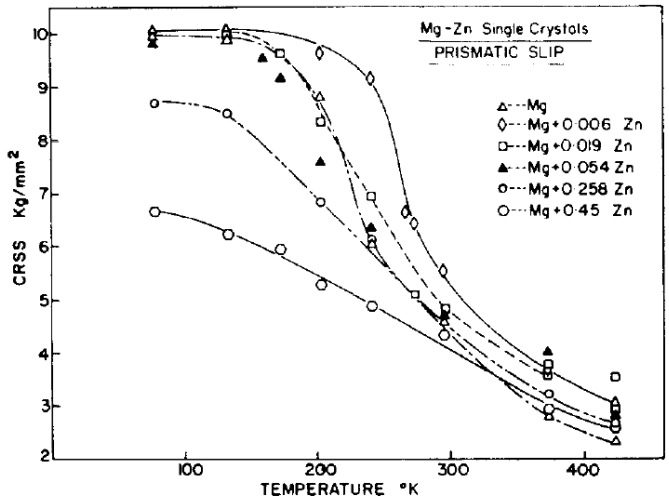

Figure 1.6: CRSS for prismatic slip as a function of temperature for Mg-Zn alloy crystals (A.Akhtar & E.Teghtsoonian, 1969b).

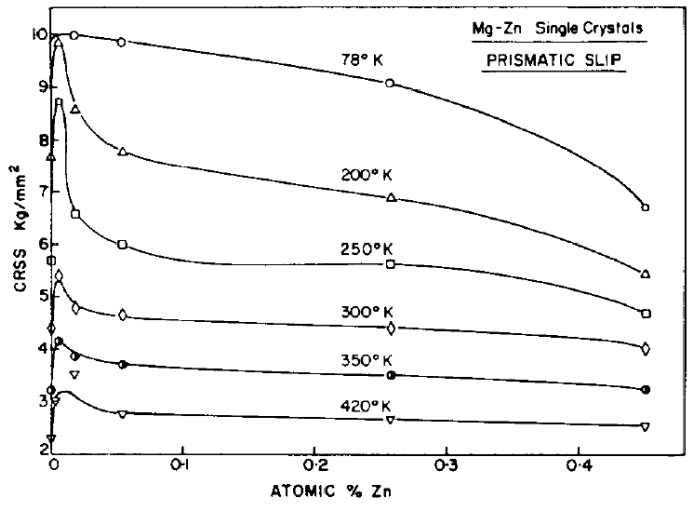

Figure 1.7: CRSS for prismatic slip as a function of Zn concentration for Mg-Zn alloy crystals (A.Akhtar & E.Teghtsoonian, 1969b).

Recently, some researchers studied the solid solution strengthening of Mg-RE alloys. Wu and Hu (Wu & Hu, 2008) compared solid solution properties of three Mg-RE (RE=Gd, Dy, Y) alloys. Figure 1.8 shows the bulk modulus of Mg alloys as a function of solute concentration. The increase of bulk modulus due to RE additions suggests that the strength of Mg alloys can be increased by additions of Gd, Dy, Y and especially additions of Gd. Gao et al., (L.Gao *et al.*, 2009b,a) and Stanford et al., (Stanford *et al.*, 2010) focused on solid solution strengthening behaviour of Mg-Y and Mg-Gd alloys. Gao et al. compared strengthening rate of Mg-Y, Mg-Al and Mg-Zn alloys (Figure1.9). They suggested that the significantly high solid solution strengthening rate of Mg-Y alloys may be due to the valence effect.

Stanford et al., (Stanford *et al.*, 2010) considered the texture effect in strengthening of Mg-Gd alloys. Figure1.10 displays the solute strengthening of prismatic slip. Presence of Gd contributes to the strengthening of the prismatic system, which is different from the behaviour of Al, Zn and Li.

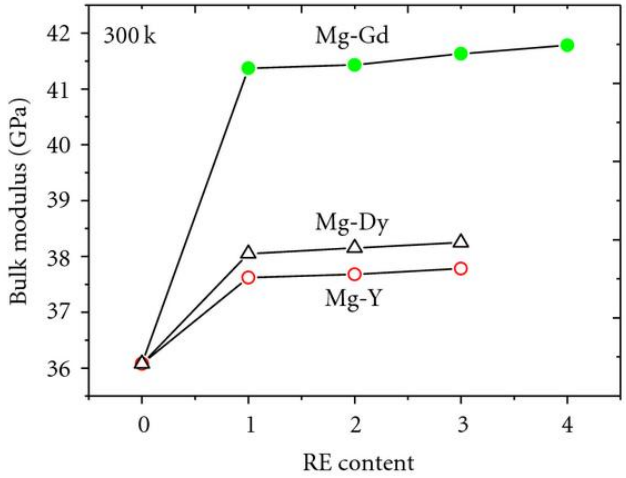

Figure 1.8: Comparison of the bulk modulus for Mg-RE alloys with different rare earth content at room temperature (Wu & Hu, 2008).

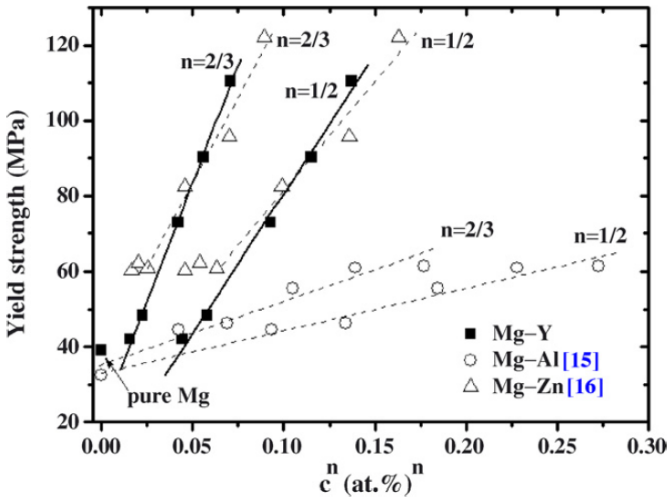

Figure 1.9: Solid solution strengthening of Mg-Y alloys compared with that of Mg-Al and Mg-Zn alloys (L.Gao *et al.*, 2009b).

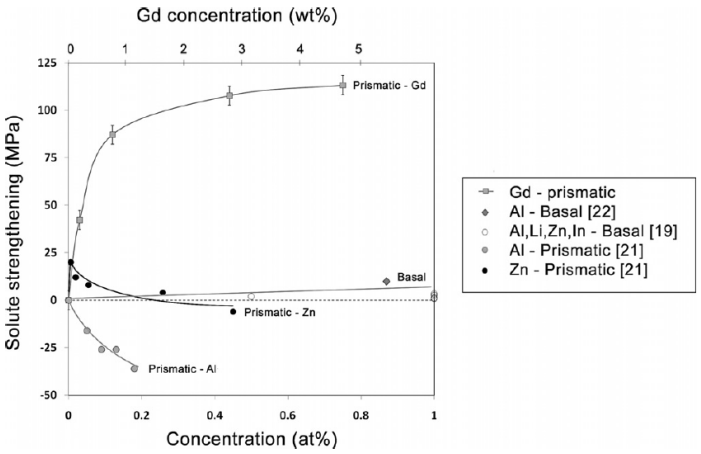

Figure 1.10: The effect of solute concentration on solute strengthening for different Mg-based solid solutions and slip systems (Stanford *et al.*, 2010).

1.5 Effect of strain rate

The strain rate during deformation tests can have a great effect on the flow stress. At a fixed strain and temperature, this effect can be expressed as per Equation 1.3:

$$\sigma = C\dot{\varepsilon}^m|_{\Sigma,T} \tag{1.3}$$

Where $\dot{\varepsilon}$ is the strain rate, C is a constant and the exponent, m, is called engineering strain rate sensitivity. There are two ways to obtain the value of m. One way is to test two samples at different strain rates and get the stress at the same strain (Figure 1.11a). The other way is to change the strain rate during the test and get the stress before and after the strain rate change (Figure 1.11b). So, m, can be calculated by

$$m = (\frac{\partial ln\sigma}{\partial ln\dot{\varepsilon}})_{\Sigma,T} \tag{1.4}$$

For most metals, the values of engineering strain rate sensitivity are between -0.005 and 0.015. Table 1.3 shows the m values of some typical engineering materials. For a multi-component system, Equation 1.4 can be rewritten as follows:

$$\frac{1}{T}(\frac{\partial ln\sigma}{\partial ln\dot{\varepsilon}})_{\Sigma,T} = \frac{1}{T}(\sigma_d m_d + \sigma_s m_s + \sigma_t m_t) \tag{1.5}$$

where d, s and t stand for dislocations, solutes and thermally activated species, respectively. In this equation, m_d represents dislocation-dislocation interactions, m_t represents interactions of dislocations with thermally activated species and m_s represents dislocation-solute interactions. Equation 1.5 can be expressed as Equation 1.6 for polycrystalline materials.

$$\frac{1}{T}(\frac{\partial ln\sigma}{\partial ln\dot{\varepsilon}})_{\Sigma,T} = \frac{1}{T}((\sigma - \sigma_0)m_d + \sigma_s m_s + \sigma_t m_t) \tag{1.6}$$

σ_0 is the yield stress of the material. A plot of $\frac{1}{T}(\frac{\partial ln\sigma}{\partial ln\dot{\varepsilon}})$ as a function of effective stress (σ - σ_0) is termed as Haasen Plot. Figure1.12 shows the schematics of a Haasen Plot. The Haasen Plot provides two important parameters. One is the y-axis intercept. A positive intercept represents the existence of thermally activated components. A negative intercept represents the existence of athermal components in the flow stress. When the intercept is zero, only dislocation-dislocation interactions dominate the flow stress. The other one is the value of engineering strain rate sensitivity, m. Engineering strain rate sensitivity, m, can be calculated by using the slope of the Haasen Plot multiplied by deformation temperature.

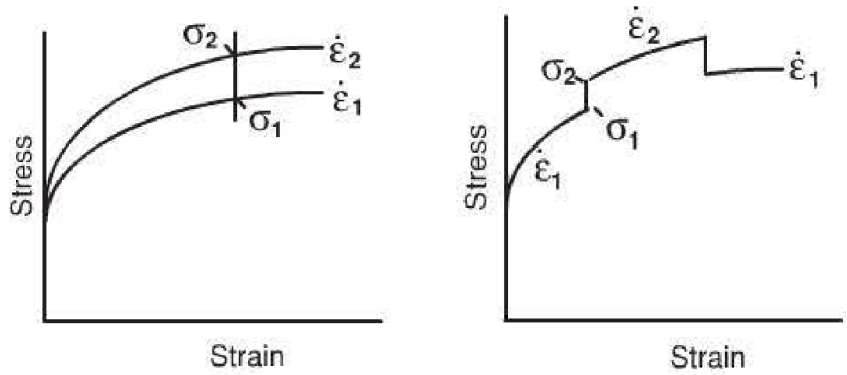

Figure 1.11: (a) Continuous stress-strain curves at different strain rates, (b) Sudden changes of strain rate.

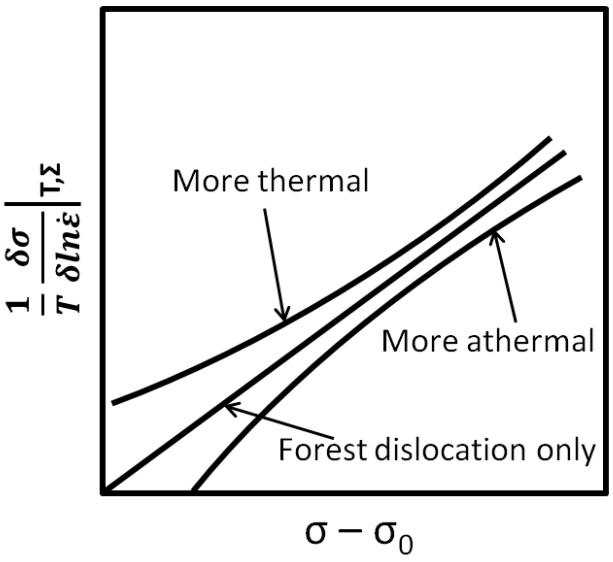

Figure 1.12: Schematic Haasen Plot.

Table 1.3: Typical values of the strain rate exponent, m, at room temperature (Hosford, 2009)

Material	m
Low-carbon streels	0.010-0.015
HSLA steels	0.005-0.010
Austenitic stainless steels	-0.005-0.005
Ferritic stainless steels	0.010-0.015
Copper	0.005
70/30 brass	-0.005-0
Aluminum alloys	-0.005-0.005
A-titanium alloys	0.01-0.02
Zinc alloys	0.05-0.08

Activation area, which is defined as the area of the slip plane swept by the dislocation during thermal activation overcoming the obstacle, can be expressed as:

$$\Delta a = \Delta a' + \int \frac{\partial \Delta a}{\partial \sigma}|_T d\sigma \tag{1.7}$$

Δa is the actual activation area, Δ a' is the apparent activation area, which is defined as the area swept by a dislocation during the glide between the unstable and stable equilibrium states at a given stress. The second term represents glide resistance induced by stress. The apparent activation area can also be expressed as:

$$\Delta a' = \frac{MkT}{b}\frac{\partial ln\dot{\varepsilon}}{\partial \sigma}|_{\Sigma,T} = \frac{MkT}{mb(\sigma - \sigma_0)} \tag{1.8}$$

where M is Taylor factor, k is Boltzmann constant, b is Burger's vector and m is engineering strain rate sensitivity. Equation 1.8 is used in this work to calculate the apparent activation area.

The apparent activation volume, which is defined as the volume swept by a dislocation during activation over the obstacles, can be calculated from:

$$\Delta V' = b\Delta a' = MkT\frac{\partial ln\dot{\varepsilon}}{\partial \sigma}|_{\Sigma,T} = \frac{MkT}{m(\sigma - \sigma_0)} \tag{1.9}$$

1.6 Texture weakening mechanisms

One way to modify the deformation behaviour of Mg alloys is to change the texture. Consequently, various studies have been focused on texture development in Mg alloy. Basal texture, in which the c-axis of most grains is parallel to the direction of compression strain, is usually observed after plastic deformation. The activation of basal slip and extension twinning is associated with the development of basal texture.

Recently, the texture weakening effect of some rare earth (RE) elements, such as yttrium and gadolinium, has been discovered (N.Stanford & M.R.Barnett., 2008; K.Hantzsche *et al.*, 2010; L.W.F.Machenzie *et al.*, 2007; S.A.Farzadfar *et al.*, 2011). Three main mechanisms of texture weakening have been proposed in previous studies. They are: particle-simulated nucleation (PSN) of recrystallization (L.W.F.Machenzie *et al.*, 2007; E.A.Ball & P.B.Prangnell, 1994), recrystallization at shear bands (N.Stanford & M.R.Barnett., 2008; K.Hantzsche *et al.*, 2010) and grain boundary mobility (Bohlen *et al.*, 2007; L.W.F.Machenzie *et al.*, 2007; N.Stanford, 2010; S.A.Farzadfar *et al.*, 2011).

1.6.1 Particle Simulated Nucleation

Particles exert a great effect on microstructure evolution during plastic deformation. During deformation, some hard particles do not deform, which induces the development of local strains and stresses. Strain relaxation is required to accommodate the shape difference between the hard particles and the plastically deformed matrix. For small particles and low strain, the strain relaxation occurs by the generation of prismatic loops. For large particles (diameter larger than 0.1 μm) and high strain, the strain relaxation occurs by local lattice rotations in the matrix adjacent to the particles. Such regions are known as particle deformation zones. The formation of particle deformation zones is associated with strain,

strain rate, temperature, particle size and particle distribution. The particle deformation zone can be the source of the nucleation during recrystallization. This is termed Particle Simulated Nucleation (PSN).

Ball and Prangnell (E.A.Ball & P.B.Prangnell, 1994) reported that little asymmetry in tension and compression deformation was observed in WE54 alloy deformed along extrusion direction. They attributed the little asymmetry to the weakened texture. Due to the relationship of the distribution of recrystallized grains and particles, they proposed that PSN could be a weakening mechanism of texture in WE54 alloy. Their results have been confirmed by Mackenzie et al., (L.W.F.Machenzie *et al.*, 2007). However, Mackenzie proposed that PSN was not the major mechanism of texture weakening in WE43. The nucleation of recrystallized grain was also associated with grain boundaries and deformation features.

1.6.2 Recrystallization at shear band

Stanford and Barnett (N.Stanford & M.R.Barnett., 2008) found a new texture peak with $<11\bar{2}1>$ parallel to the extrusion direction, which was termed Rare-Earth Texture in Mg alloys containing La and Gd. They reported that the single-phase Gd containing alloy does not contain precipitates, which suggests that Particle Simulated Nucleation theory is not the mechanism of weakened texture. They found that the recrystallized grains originating from shear bands, produce the weakened rare earth texture. Senn and Agnew (W.Senn & R.Agnew, 2008) observed shear bands in alloys with content of RE or Y. The recrystallized grains originating from the nuclei in the shear bands exhibit a weaker texture compared to the deformed grains. Hantzsche et al., (K.Hantzsche *et al.*, 2010) proposed that the weakened texture of Mg-RE alloys containing Ce, Nd and Y is connected with the appearance

of deformation bands containing deformation twins.

1.6.3 Grain Boundary Mobility

Under some conditions, grain boundaries of a particular character may have high mobility. Recrystallization nuclei originating from the high mobility boundaries may have a growth advantage as a result of their orientation, size, position or surrounding deformation substructure. Those recrystallized grains have a great effect on deformation texture.

Bohlen et al., (Bohlen *et al.*, 2007) proposed that the texture modification of RE/Y alloy may be attributed to the nature of the solid solution alloy matrix. Y atoms are large atoms which have low diffusivity. It is speculated that the strong influence of solute drag on grain boundary mobility of different grain boundary orientations and recrystallization kinetics are responsible for the texture weakening.

Mackenzie et al., (L.W.F.Machenzie *et al.*, 2007) studied the texture evolution of as extruded and annealed WE43 alloy. Although PSN appears to be a recrystallization mechanism, it does not govern the final texture. They found that the weakened texture was associated with an orientation selection in the early stages of recrystallization and grain growth. It is known that solute elements can change grain boundary behavior and orientation relationships for high boundary mobility. Consequently, they concluded that the weakened texture may be dominated by growth selection where alloying additions change the grain boundary behavior and orientation relationships for high boundary mobility.

Stanford (N.Stanford, 2010) investigated the texture evolution of Mg alloys containing Y, Ce, Gd and La after extrusion at 450°C. It is reported that a strong interaction of solute elements with dislocations and grain boundaries induced the weakened texture. Farzadfar et al., (S.A.Farzadfar *et al.*, 2011) found non-basal texture component in recrystallized grains

lager than 8.6 μm in Mg-2.9 wt.% Y alloys. It is suggested that the weakened texture is associated with the preferential growth of non-basal recrystallized grain whose advantage is due to the change in grain boundary mobility.

Chapter 2

Experimental procedure

2.1 Alloy development and thermo-mechanical processing

The binary Mg-Y alloys were produced in laboratory by mixing appropriate amount of 99.99% purity Magnesium with Mg-20.8 wt.% Y master alloy. Mg-Y alloys were cast in a cylindrical stainless steel mould cavity couted with boron nitride, using an induction furnace under argon atmosphere. High purity Magnesium and Mg-20.8 wt.% Y master alloy pieces were put into a graphite crucible placed above the mould. The chamber was evacuated with a vacuum pump and then backfilled with argon gas. This cycle was repeated three times. Using the induction furnace, the metal was heated to approximately 770°C and held for 6 minutes around this temperature. The melt was then cast and cooled down until the temperature had reached approximately 120°C. All these procedures were performed under argon atmosphere. The cast ingots which were cylindrical in shape and ϕ70mm x 45mm in size were homogenized at 520°C for 24 hours under argon atmosphere. The surface of the homogenized ingots was milled away to remove the oxide layer.

Table 2.1: Composition of Mg-Y Alloys

Chemical composition at.%	Nominal composition at.%	Grain size μm
0.29751	0.30	170
0.54905	0.55	170
0.81537	0.82	124
1.13467	1.13	132
1.29778	1.30	75
pure Mg	pure Mg	183

Homogenized ingots were annealed at 470°C for 1 hour in air. The ingots were cold-rolled with a 1mm reduction in a pass and annealed again at 470°C for 1 hour. This process was repeated until the desired thickness of 5mm was achieved in the as rolled sheet. Part of the rolled sheet was cut to prepare compression samples, while the rest of the materials was further processed by a combination of rolling and annealing to a final thickness of 3mm.

The compositional analysis of samples used in the present study was performed using inductively coupled plasma mass spectrometry (ICP-MS). The compositions of all Mg-Y alloys, which have been developed by this procedure, are given in table 2.1.

2.2 Deformation Procedure

Tensile test samples with gauge dimensions of 2 x 3 x 40 mm and compression test samples with ϕ5mm x 10mm were machined from the cold rolled sheet. The sample orientation is displayed in Figure 2.1. Before deformation, the samples were annealed at 500°C for 15 minutes to produce a recrystallized material and to relieve residual stresses in the sample after the rolling and machining process. Tensile and compressive tests were performed on samples at 298K, 78K and 4K using a homemade screw-driven single axis tensile test apparatus. The samples were deformed at a constant cross-head velocity corresponding to an initial strain rate of 2.8 x 10^{-4} s^{-1}. For room temperature tensile tests, the samples were open in air atmosphere; for 78K, samples were sealed in a chamber and immersed in a dewar filled with liquid nitrogen; for 4K, samples were sealed in a chamber which is immersed in a dewar filled with liquid helium and covered by a dewar with liquid nitrogen. This experimental setup is displayed in Figure 2.2.

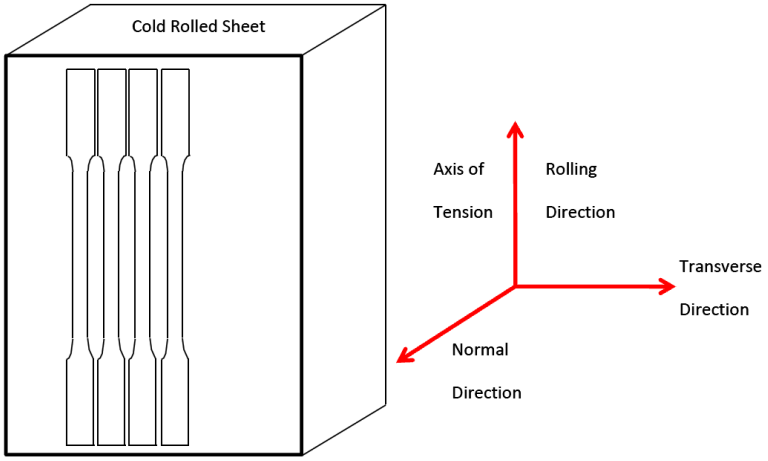

(a)

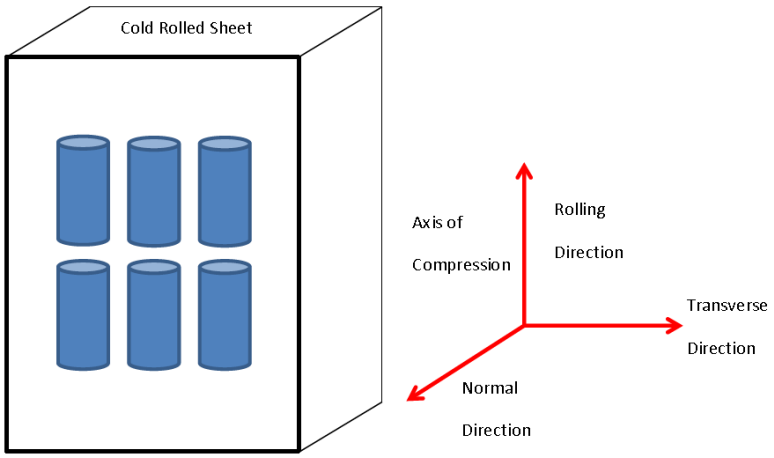

(b)

Figure 2.1: Orientation of machined samples with respect to the rolled sheet. (a) Orientation of tensile samples (b) Orientation of compression samples.

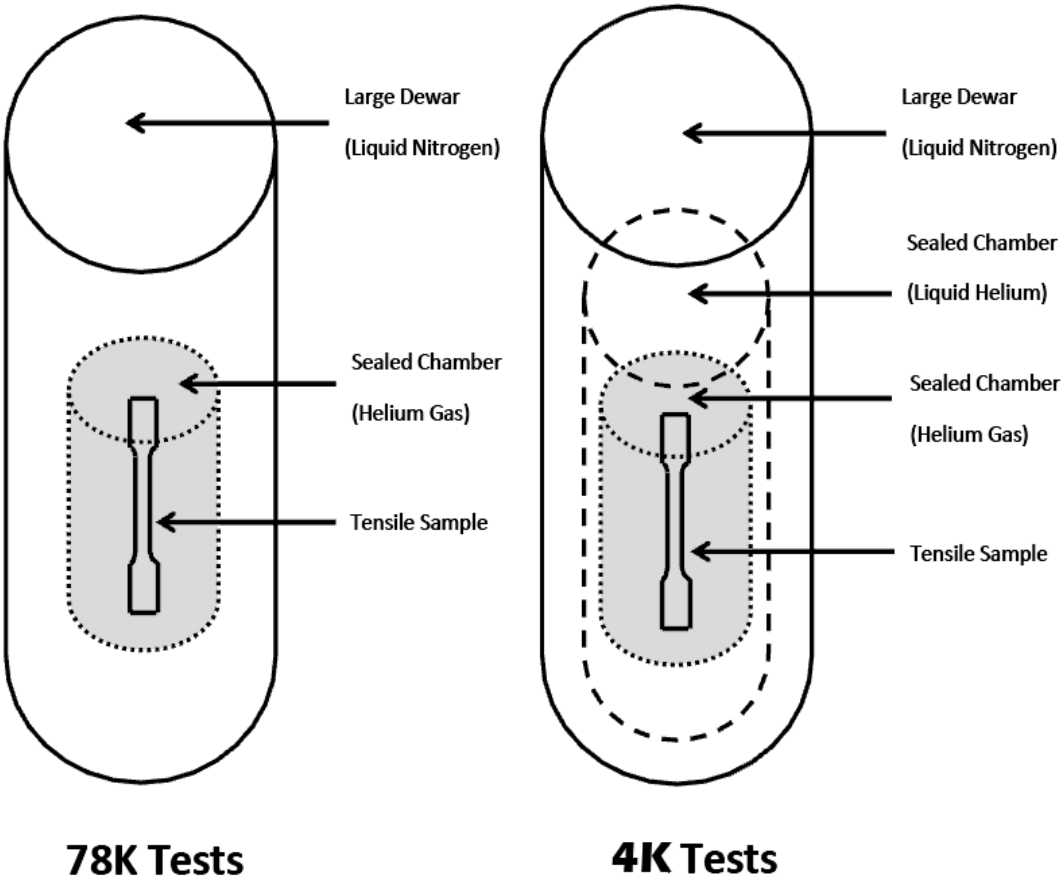

Figure 2.2: Schematics of the arrangement of dewars for 78K and 4K experiments.

2.3 Strain rate sensitivity measurement

Strain rate sensitivity (SRS) test were performed on samples under both tension and compression. The strain rate sensitivity jumps were carried out by repeating the instantaneous strain rate change between 2.8x10^{-4} s^{-1} and 2.8x10^{-5} s^{-1} during deformation. The experimental data of strain rate sensitivity measurements are analyzed by the Haasen Plot.

2.4 SEM

Fracture surfaces of Mg-0.55at.% Y and Mg-1.13 at% Y alloys deformed under tension and compression at three different temperatures were analyzed by using JEOL JSM-7000F Scanning Electron Microscope (SEM).

2.5 Texture measurements

The bulk texture of samples before deformation, during deformation and after deformation was measured by XRD using a Bruker D8 diffractometer with a Co Kα source. Transverse section was the plane from which X-ray data was taken (Figure 2.3). The pole figures were evaluated by using Bruker GADDS software. The distribution of basal planes was calculated from orientation distribution functions by using MTEX package in MATLAB software (S.A.Farzadfar *et al.*, 2011). The volume fraction of twinning was calculated using Bruker's MULTEX software.

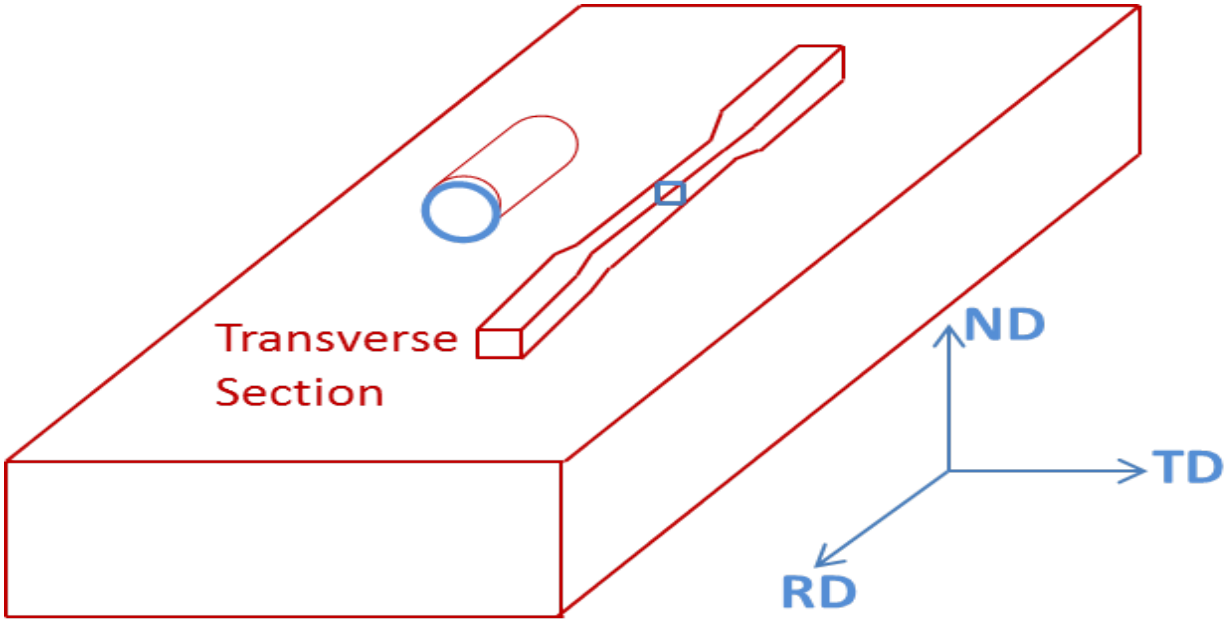

Figure 2.3: Orientation of tensile and compression samples used for texture measurements with respect to the orientation of the rolled sheet. ND-TD plane of the sheet. Thus, the rolling direction,RD, of the sheet coincides with the tensile or compression axis of the samples.

Chapter 3

Results

3.1 Mechanical testing

3.1.1 Tensile test at 298K, 78K and 4K

Figure 3.1 shows true stress - true strain characteristics of Mg-Y alloys at 298K, 78K and 4K. As the concentration of Y increases, the alloys show higher flow stress. The maximum flow stress of about 206 MPa, 333 MPa and 280 MPa is being observed in Mg-1.13at.%Y alloy at 298K, 78K and 4K, respectively. The elastic-plastic transition becomes more pronounced with the increase of Y content. For 298K and 78K, the strain at failure decreases with increasing solute content up to 0.82at.%, at which point there is an increase in strain at failure. Then, the strain at failure decreases again as the solute content increases. Additionally, the strain at failure of all alloys is larger than that of pure Mg. Tensile curves of Mg-Y alloys exhibit extensive serration at 4K (Figure 3.1c), which is associated with the adiabatic shear deformation. The adiabatic deformation is accompanied by characteristic

acoustic emission of clicks, easily detectable by human ear. The frequency and the amplitude of adiabatic stress drops increases with the flow stress and the concentration of Y in the alloys (Figure 1c). The stress drop of alloys, during adiabatic instabilities, increases as the flow stress increases, from approximately 3 MPa at the early stage of deformation to more than 10 MPa at the later stage of deformation. The onset of adiabatic instabilities shifts a little bit towards the lower stress with the increasing Y content.

Figure 3.2 shows deformation behaviour of individual Mg-Y alloys and pure Mg at three deformation temperatures. The yield strength increases as deformation temperature decreases for each alloy composition. It is seen that temperature has a strong effect on the flow stress; alloys deformed at lower temperatures exhibit higher flow stress and work-hardening rate, but lower ductility. For pure Mg, anomalous flow stress and yield stress behaviour are observed, expressed in the lower yield and the flow stress at 4K than that at 78K.

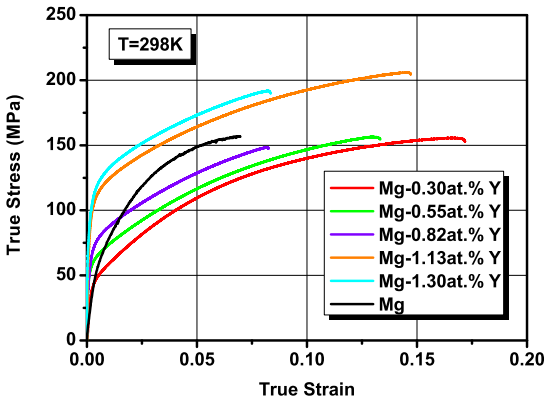

(a)

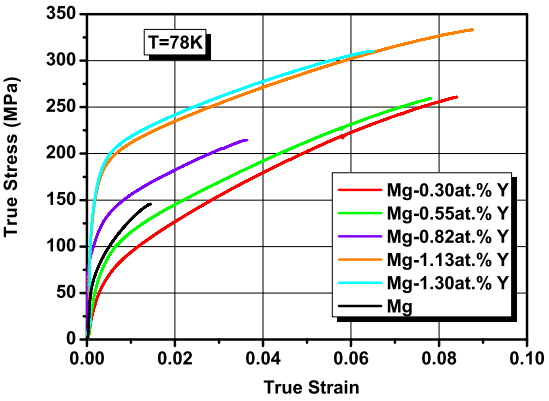

(b)

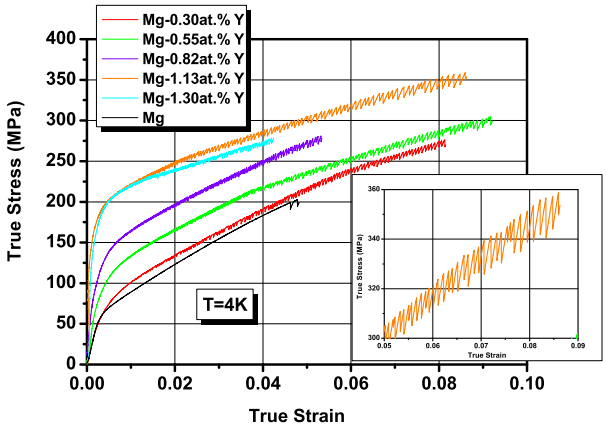

(c)

Figure 3.1: True stress vs. true strain characteristics for five compositions of Mg-Y alloys deformed under tension at deformation temperatures of: (a) 298K, (b) 78K and (c) 4K. Insert in figure (c) shows adiabatic instabilities observed in Mg-1.13at.%Y at 4K.

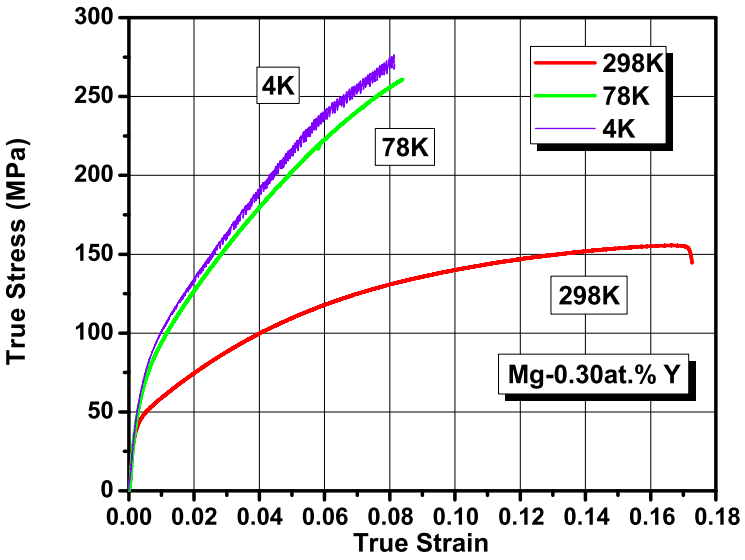
True Stress (MPa)
True Strain
298K
78K
4K
4K
78K
298K
Mg-0.30at.% Y
0
50
100
150
200
250
300
0.00
0.02
0.04
0.06
0.08
0.10
0.12
0.14
0.16
0.18

(a)

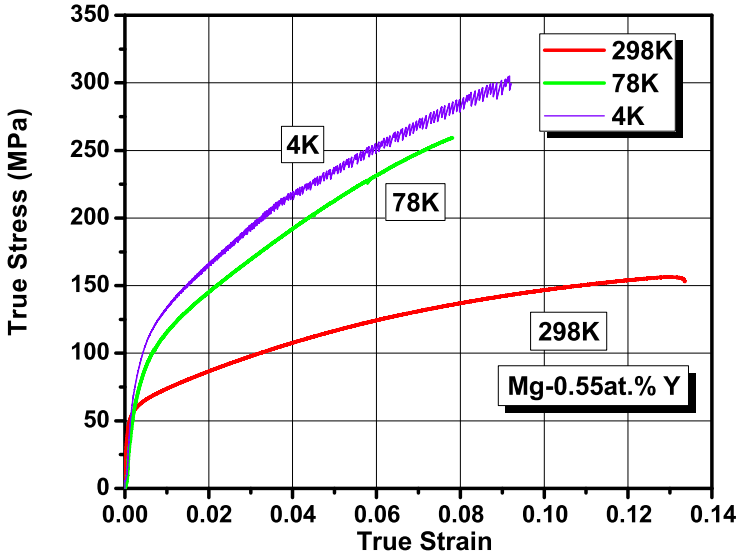
True Stress (MPa)
True Strain
298K
78K
4K
4K
78K
298K
Mg-0.55at.% Y
0
50
100
150
200
250
300
350
0.00
0.02
0.04
0.06
0.08
0.10
0.12
0.14

(b)

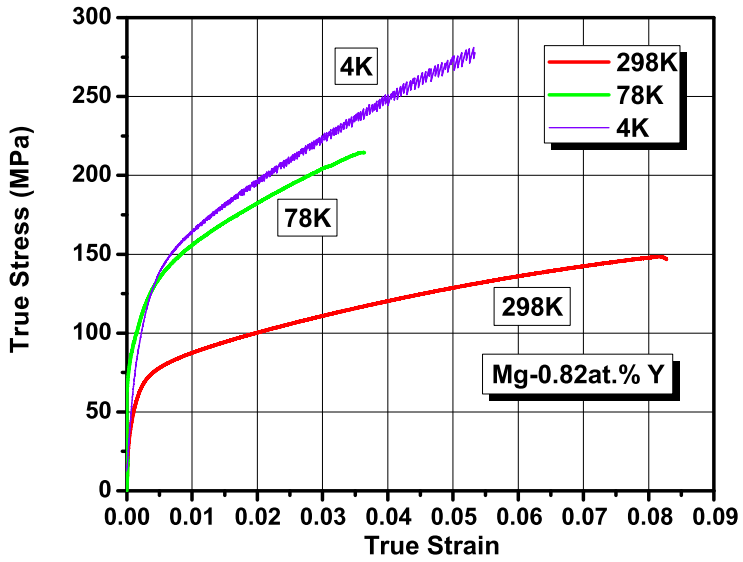
True Stress (MPa)
True Strain
4K
78K
298K
298K
78K
4K
Mg-0.82at.% Y

(c)

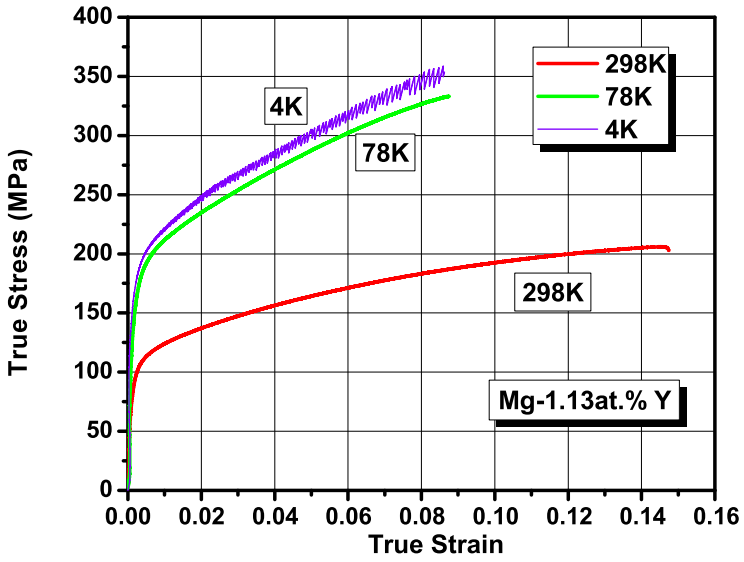
True Stress (MPa)
True Strain
4K
78K
298K
298K
78K
4K
Mg-1.13at.% Y

(d)

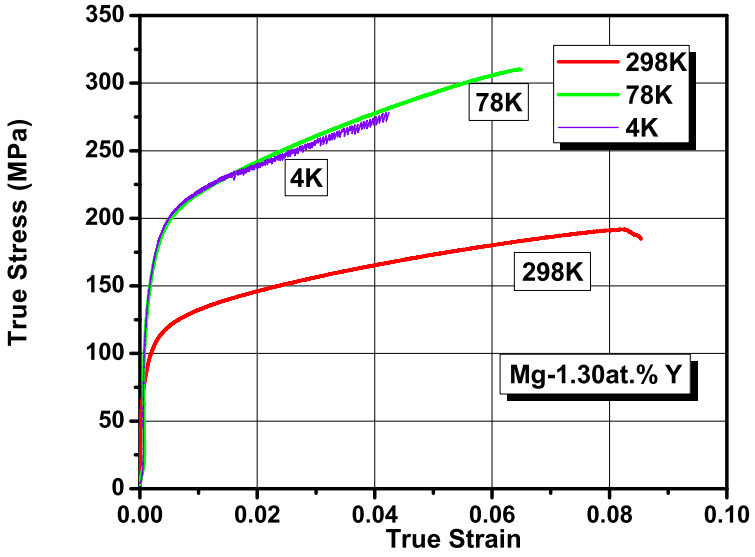

(e)

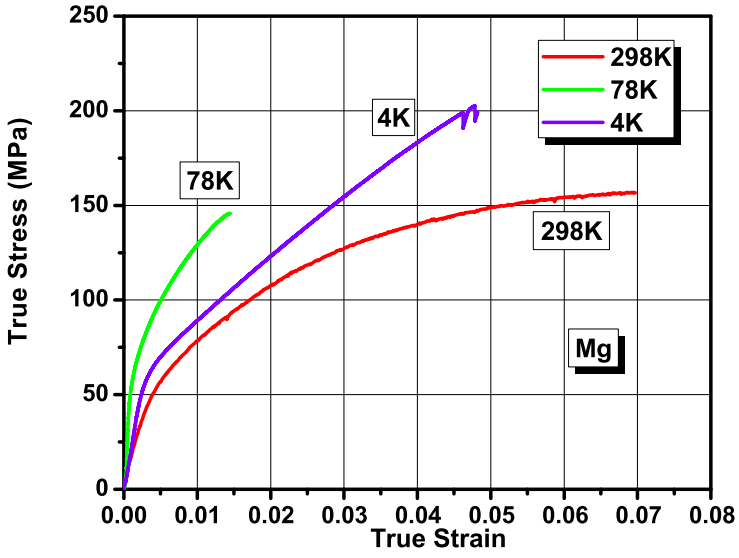

(f)

Figure 3.2: Comparison of true stress vs. true strain characteristics of Mg-Y alloys deformed under tension at 298K, 78K and 4K for different alloy compositions: (a) Mg-0.30at.% Y, (b) Mg-0.55at.% Y, (c) Mg-0.82at.% Y, (d) Mg-1.13at.% Y, (e) Mg-1.30at.% Y, (f) pure Mg.

Figure 3.3 provides the summary of tensile yield stress for different alloy compositions at different deformation temperatures. The yield strength increases approximately linearly with Y content up to 1.13 at.% beyond which the yield strength still increases with Y concentration, but with a lower rate. The yield stress show well pronounced temperature dependence; it increases by about 40 - 80 MPa between room temperature and 4K in every alloy.

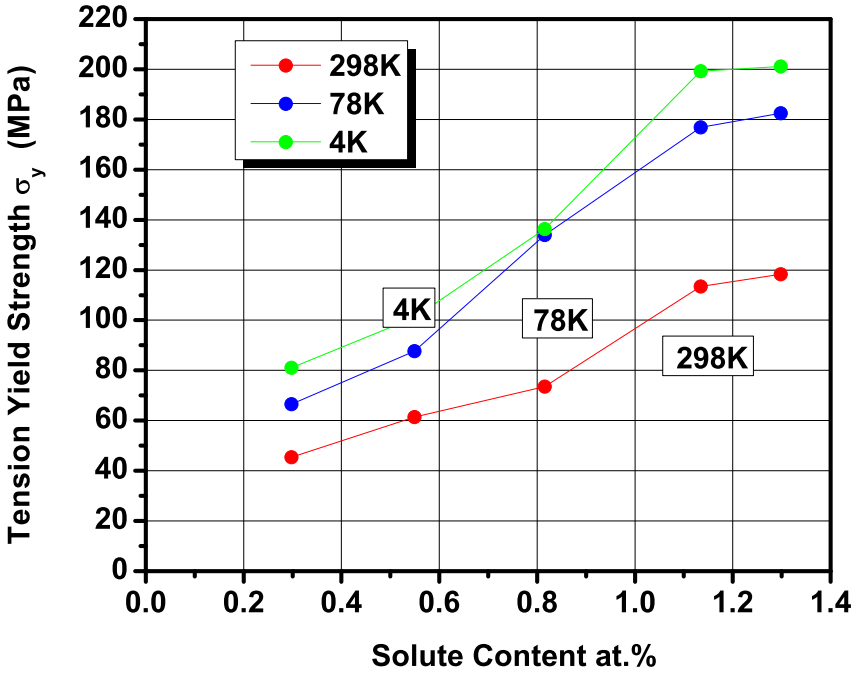

Figure 3.3: Tension yield strength as a function of Y content at three deformation temperatures of 298K, 78K and 4K.

Figure 3.4 shows the variations of the flow stress as a function of alloy composition at 298K, 78K and 4K at different strain levels marked on the figures. At all deformation temperatures the flow stress increases approximately linearly with increasing Y content, reflecting the kinetics of the work-hardening process in these alloys.

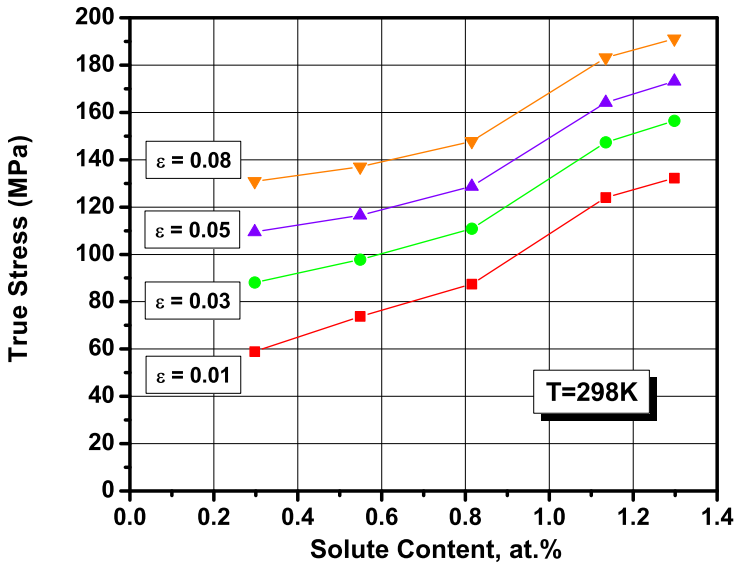

(a)

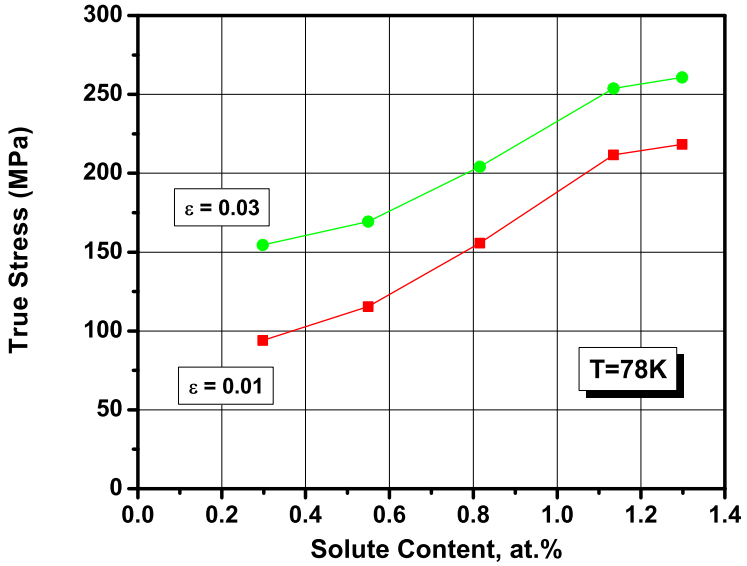

(b)

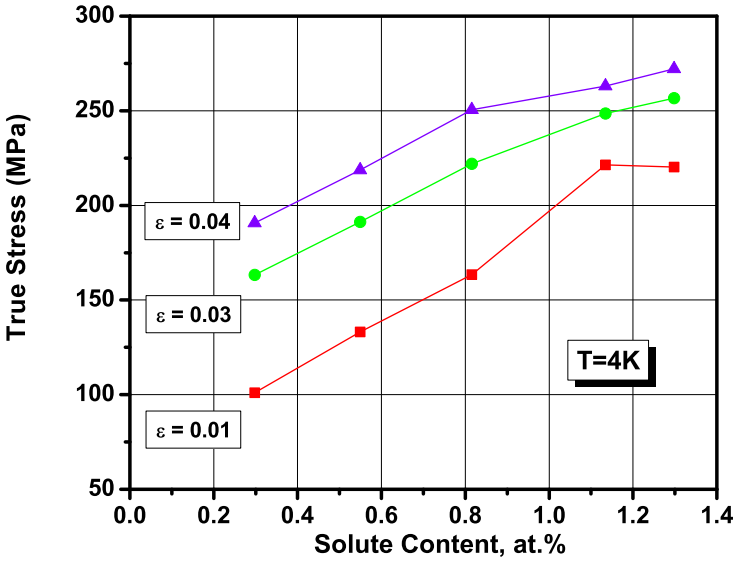

(c)

Figure 3.4: Strengthening effect in Mg-Y alloys, measured as the value of tensile true stress at different strain levels as a function of Y content at: (a) 298K, (b) 78K and (c) 4K.

3.1.2 Compression test at 298K, 78K and 4K

Figure 3.5 shows true stress - true strain characteristics of Mg-Y alloys and pure Mg deformed under compression at 298K, 78K and 4K. Compression characteristics of Mg-Y alloys show substantial differences than tension curves discussed previously. For pure Mg, the plastic flow is initiated by plateau-like behaviour followed by increase of the flow stress. When the yttrium content increases, the initial plateau behaviour gradually disappears. For the lowest concentration alloy, Mg-0.30 at.% Y alloy, the flow stress behaviour is still similar to pure Mg. As the concentration of Y increases, the flow stress still increases, but at a lower rate. Also, the transition from elastic to plastic becomes more pronounced.

The instability observed in tensile testing at 4K was also observed in compression testing at 4K. The amplitude of the adiabatic stress drop is independent of Y content, but still increases with the flow stress, even though it is not as pronounced as during tensile test. The stress drops of alloys increase from approximately 2 MPa at the early stage of deformation to about 10 MPa at the later stage of deformation. The onset of adiabatic instabilities shifts towards the lower stress with the increasing Y content.

Figure 3.6 shows the deformation behaviour under compression of individual Mg-Y alloys at three deformation temperatures. The yield strength in every alloy increases with decreasing deformation temperature. The difference in flow stress between 298K and 78K increases with the increase of Y content. Temperature has a pronounced influence on the deformation behaviour of Mg-Y alloys; the alloys show systematically the higher flow stress, the higher work-hardening rate and the lower ductility at lower deformation temperatures.

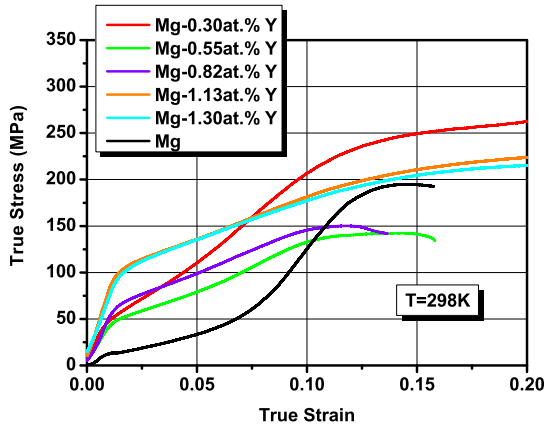

(a)

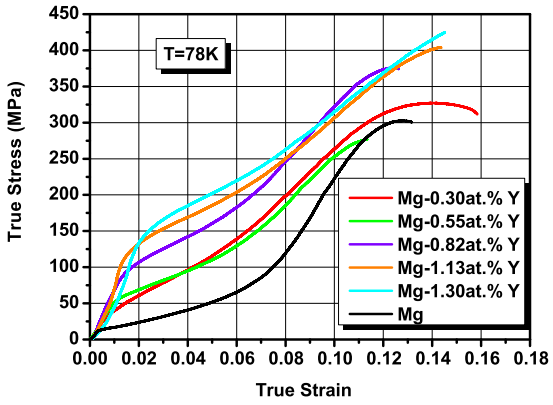

(b)

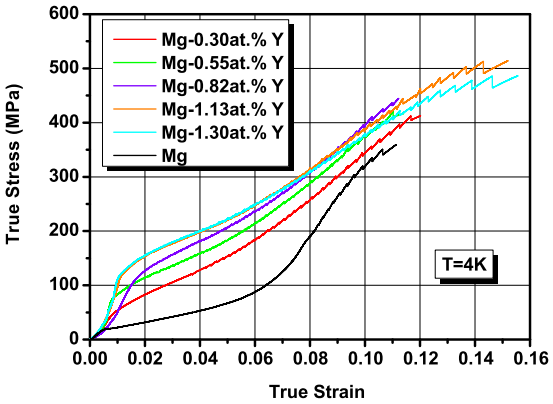

(c)

Figure 3.5: True stress vs. true strain characteristics for five compositions of Mg-Y alloys deformed under compression at deformation temperatures of: (a) 298K, (b) 78K and (c) 4K.

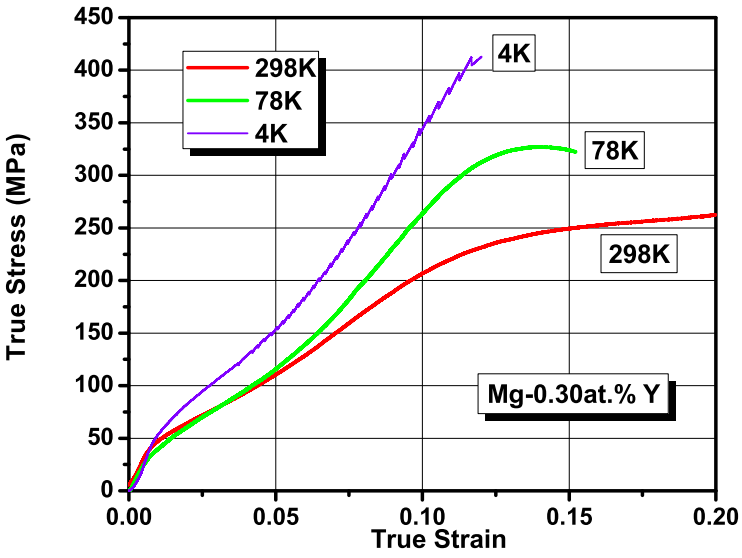
True Stress (MPa)
True Strain
298K
78K
4K
4K
78K
298K
Mg-0.30at.% Y
0
50
100
150
200
250
300
350
400
450
0.00
0.05
0.10
0.15
0.20

(a)

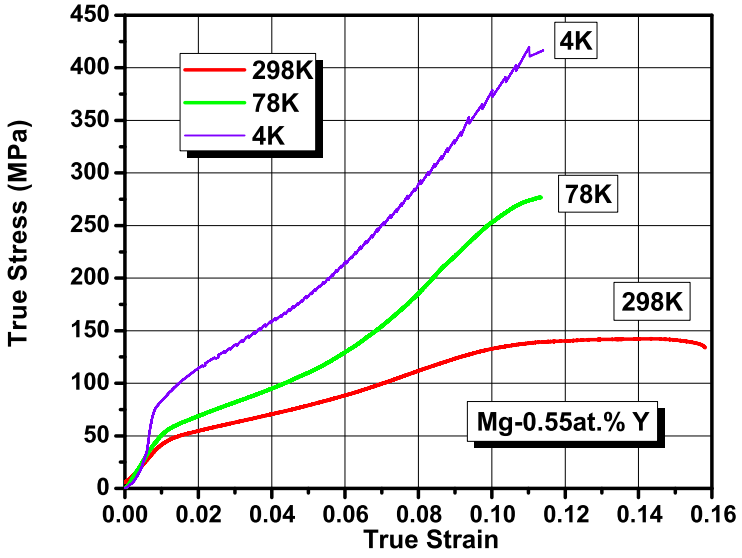
True Stress (MPa)
True Strain
298K
78K
4K
4K
78K
298K
Mg-0.55at.% Y
0
50
100
150
200
250
300
350
400
450
0.00
0.02
0.04
0.06
0.08
0.10
0.12
0.14
0.16

(b)

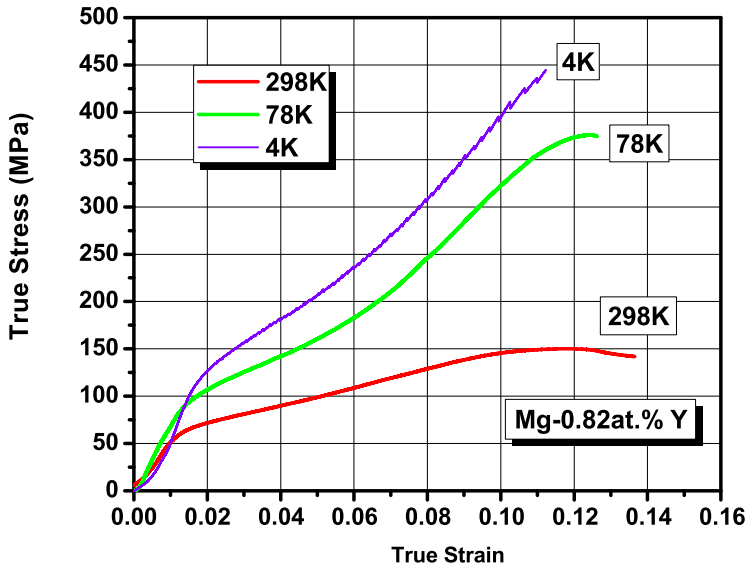
True Stress (MPa)
True Strain
298K
78K
4K
4K
78K
298K
Mg-0.82at.% Y

(c)

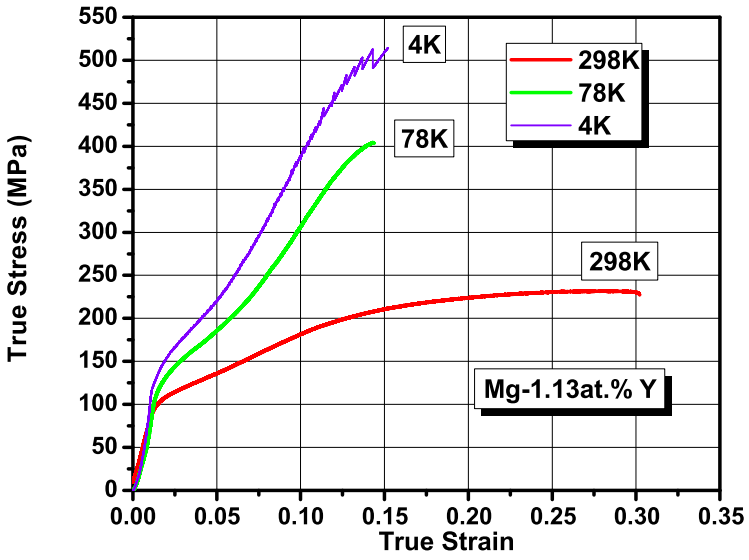
True Stress (MPa)
True Strain
4K
78K
298K
78K
4K
298K
Mg-1.13at.% Y

(d)

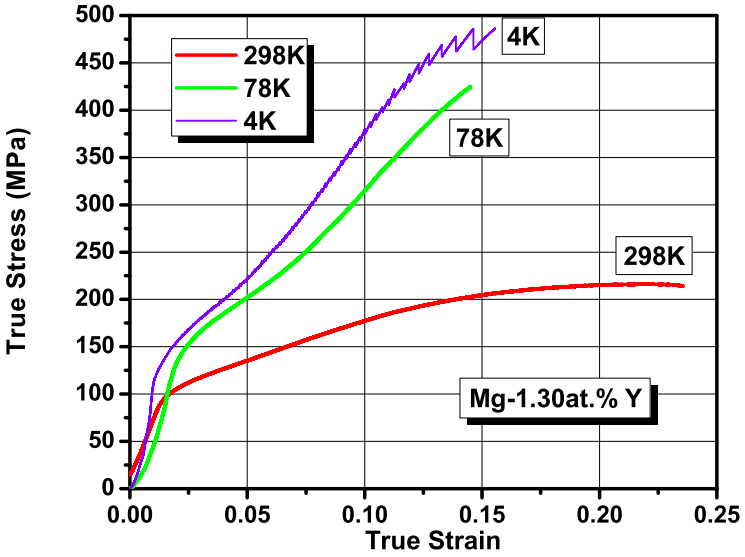

(e)

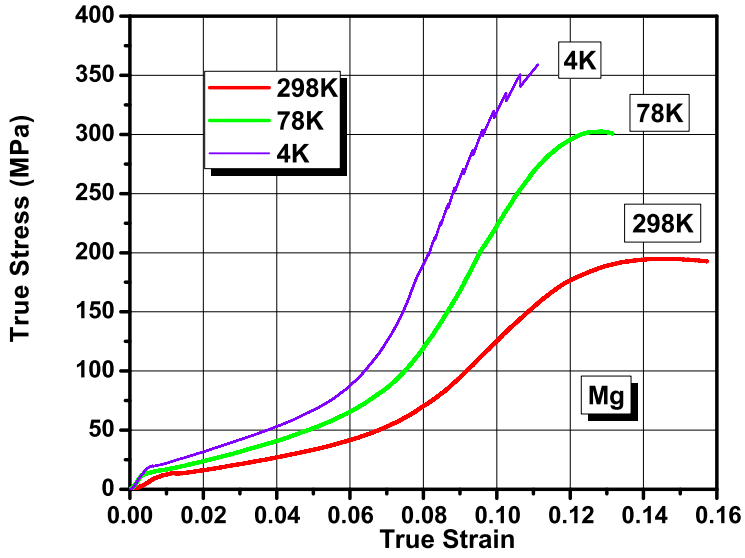

(f)

Figure 3.6: Comparison of true stress vs. true strain characteristics of Mg-Y alloys deformed under compression at 298K, 78K and 4K for different alloy compositions: (a) Mg-0.30at.% Y, (b) Mg-0.55at.% Y, (c) Mg-0.82at.% Y, (d) Mg-1.13at.% Y, (e) Mg-1.30at.% Y, (f) pure Mg.

Figure 3.7 provides the summary of compression yield stress for different alloy compositions at different deformation temperatures. The yield strength increases with Y content and shows well pronounced temperature dependence; it increases by about 20 - 70 MPa between room temperature and 4K in every alloy. Table 3.1 summarizes the tensile and compression yield stress at temperatures of 298K, 78K and 4K. It is seen that the yield stress during compression is lower than in tension.

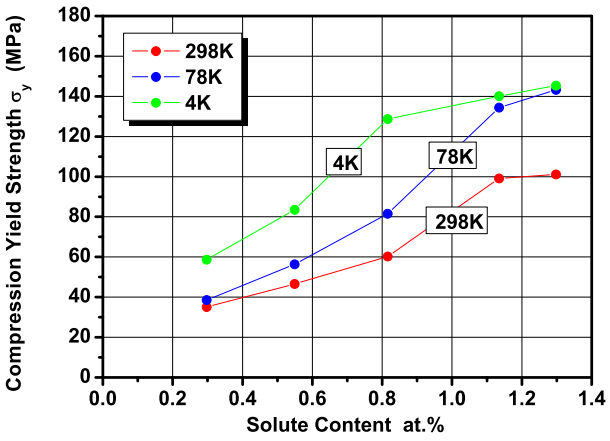

Figure 3.7: Compression yield strength evolution as a function of Y content at three deformation temperatures of 298K, 78K and 4K.

Table 3.1: Yield Stress of Mg-Y Alloys

Composition at.%	$298K(MPa)$		$78K(MPa)$		$4K(MPa)$	
	Tension	Compression	Tension	Compression	Tension	Compression
Mg	70.7	11.1	80.8	15.5	69.6	20.1
0.30	45.4	35.1	66.5	38.6	81.1	58.7
0.55	61.4	46.6	87.7	56.3	101.0	83.5
0.82	73.5	60.2	133.9	81.5	136.3	128.7
1.13	113.4	99.1	176.8	134.4	199.2	140.1
1.30	118.3	101.1	182.5	143.2	201.1	145.3

Figure 3.8 shows the variations of the flow stress as a function of alloy composition deformed under compression at 298K, 78K and 4K at different strain levels marked on the figures. For 298K, the flow stress of Mg-0.30at. %Y alloy is higher than Mg-0.55at. % Y alloy. Then, the flow stress increases with Y content up to 1.13at. % Y, followed by a small decrease. The high flow stress of Mg-0.30at. %Y alloy is very similar to the flow stress of pure Mg which exhibits high work hardening rate during plastic region. For 78K, the flow stress of Mg-0.30at. % Y alloy is still higher than Mg-0.55at. % Y alloy, but not as much as that at 298K. Then, the flow stress increases with increase of Y content. For 4K, the flow stress increases with the increasing Y concentration till the concentration of Mg-1.1at. %Y and it stabilizes at the same level.

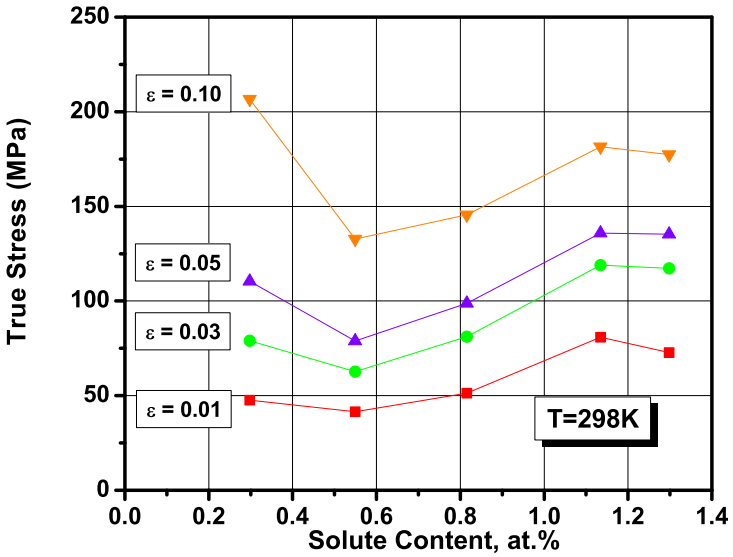

(a)

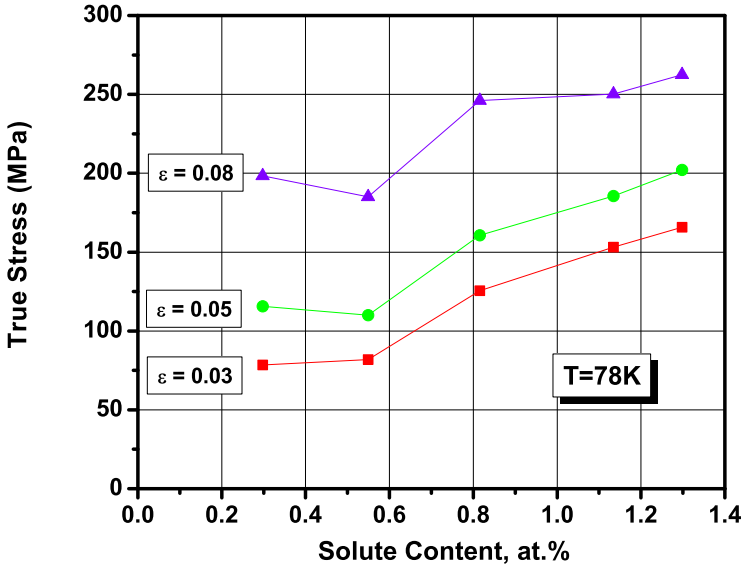

(b)

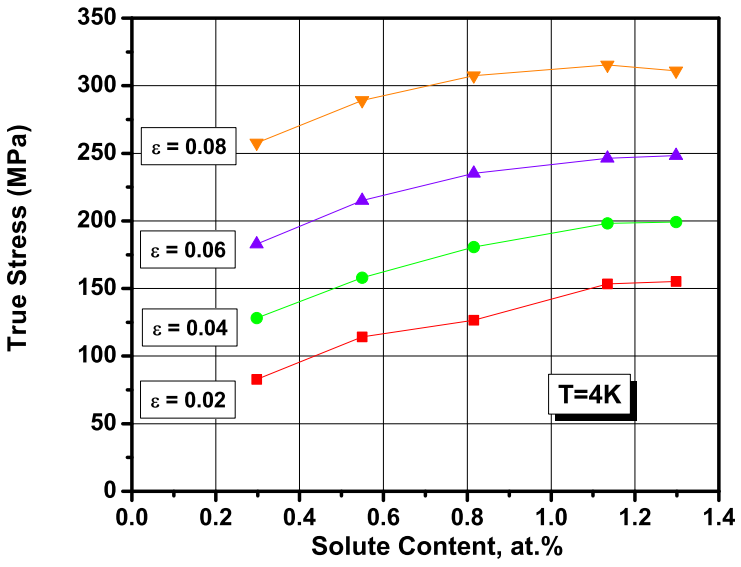

(c)

Figure 3.8: Strengthening levels under compression, measured as the value of the true stress at different strain levels marked on the figures, as a function of Y content at: (a) 298K, (b) 78K and (c) 4K.

3.2 Work-hardening results

3.2.1 Work-hardening behaviour in tension

Figure 3.9 shows the characteristics of work-hardening rate, $d\sigma/d\varepsilon$, as a function of effective stress (σ - σ_0) deformed under tension at different deformation temperatures. All alloys show stage III of continuous decrease of work-hardening rate from the initial value Θ_0 until the fracture. Pure Mg exhibits very high work-hardening rate at the beginning of deformation as a result of elastic-plastic transition, which decreases rapidly with the flow stress. Comparing to pure Mg, Mg-Y alloys exhibit more gradual exhaustion of work-hardening capacity. The solute atoms change the kinetics of the dynamic recovery process. When Y is present in the alloy, the Y atoms segregate to dislocations, forming solute atmospheres that exert a drag effect on dislocations and inhibit dislocation glide, cross slip and climb. At low temperatures, one observes that work-hardening decreases at a much lower rate for all alloys, which exhibit similar work-hardening behaviour indicating that the effect of solute on hardening capacity is diminished as the temperature decreases. Figure 3.10 shows work-hardening rate as a function of effective stress for an individual alloy and pure Mg deformed under tension at 298K, 78K and 4K. In all cases, work-hardening capacity at low temperature is larger than that at 298K, suggesting that more effective dislocation storage occurs at low temperature than at room temperature.

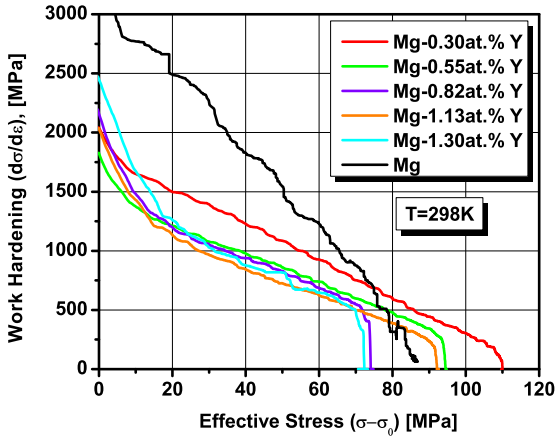

(a)

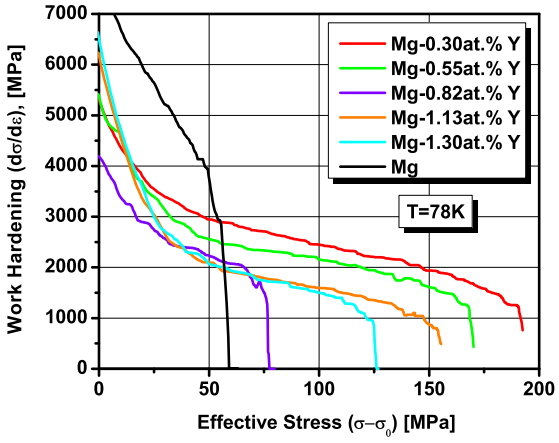

(b)

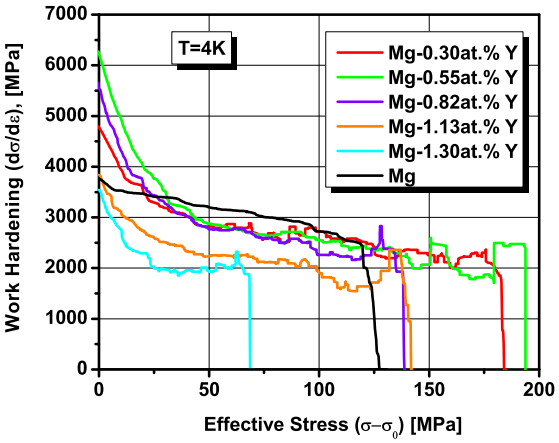

(c)

Figure 3.9: Work-hardening rate as a function of effective stress for Mg-Y alloys and pure Mg deformed under tension at: (a) 298K, (b) 78K and (c) 4K.

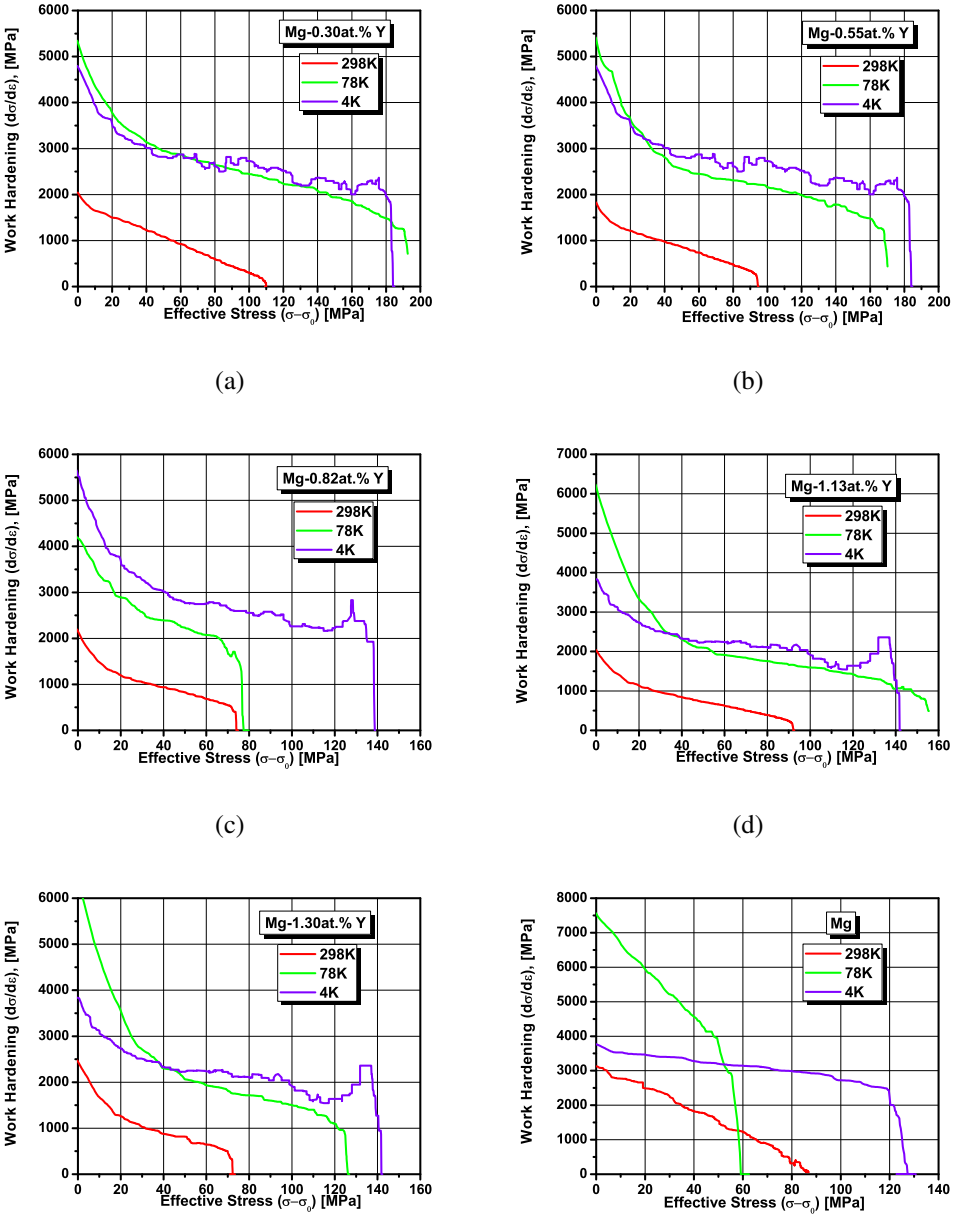

Figure 3.10: Work-hardening rate as a function of effective stress for Mg-Y alloys and pure Mg deformed under tension at 298K, 78K and 4K for different alloy compositions: (a) Mg-0.30at.% Y, (b) Mg-0.55at.% Y, (c) Mg-0.82at.% Y, (d) Mg-1.13at.% Y, (e) Mg-1.30at.% Y, (f) pure Mg.

3.2.2 Work-hardening behaviour in compression

Figure 3.11 shows characteristics of the work-hardening rate as a function of effective stress for Mg-Y alloys deformed under compression at 298K, 78K and 4K. Work-hardening compression characteristics show substantial differences than tension curves. The Y content changes the kinetics of work-hardening. For pure Mg, the work-hardening rate increases from the beginning of plastic deformation, forms a plateau at some value of the effective stress and then decreases. For Mg-Y alloys, the behaviour of work-hardening rate is qualitatively similar, although three stages are less pronounced than in pure Mg. Nevertheless, it is also observed that work-hardening decreases from the initial value, forms a plateau and then increases gradually at higher stresses, followed by decreasing work-hardening rate.

This behaviour will be discussed later, but it is attributed to the activity of twinning. For both pure Mg and Mg-Y alloys, twinning starts from the beginning of the plastic deformation. For Pure Mg, twins interact with other twins and slip dislocations almost from the beginning of plastic deformation and the work-hardening rate increases right from the beginning. For Mg-Y alloys, deformation is accommodated by more slip systems. Twins do not interact with other twins at the beginning of plastic deformation and the initial work-hardening rate decreases under this condition. When twins start interacting with other twins and slip dislocations, the work-hardening rate increases. It is seen that the behaviour of the work-hardening rate is related to Y content. Figure 3.12 shows the work-hardening rate as a function of effective stress for an individual alloy and pure Mg deformed under compression at 298K, 78K and 4K. In all cases, both initial work-hardening rate and work-hardening capacity increase with the decrease of deformation temperature, indicating that dislocation storage at low temperatures is more effective than at high temperatures.

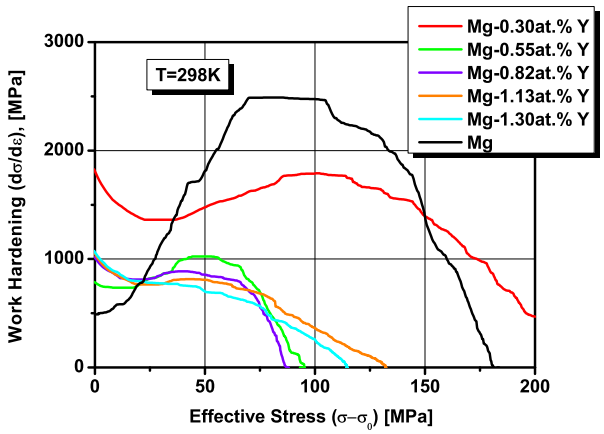

(a)

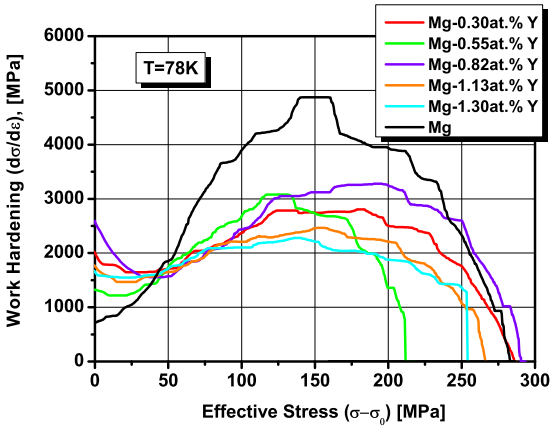

(b)

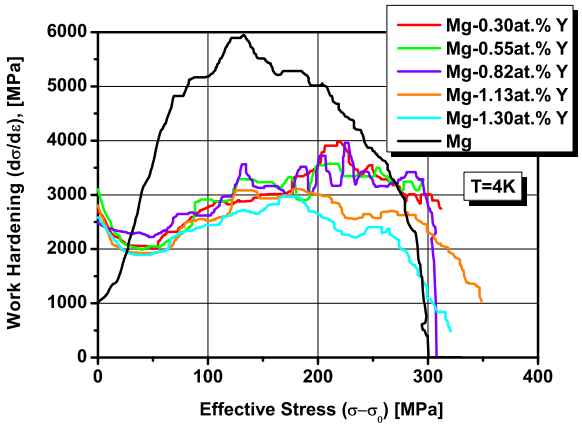

(c)

Figure 3.11: Work-hardening rate as a function of effective stress for Mg-Y alloys and pure Mg deformed under compression at (a) 298K, (b) 78K and (c) 4K.

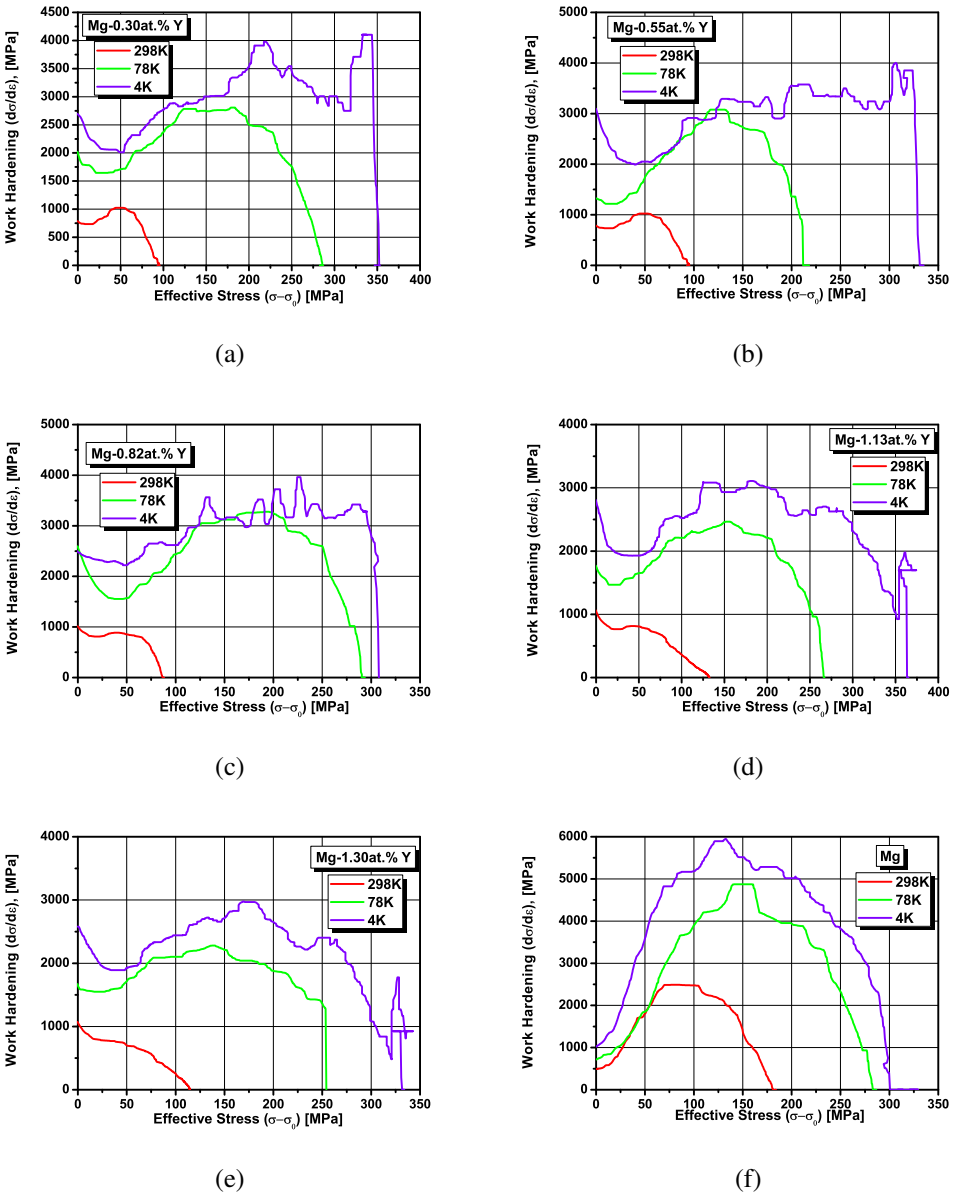

Figure 3.12: Work-hardening rate as a function of effective stress for Mg-Y alloys and pure Mg deformed under compression at 298K, 78K and 4K for different alloy compositions: (a) Mg-0.30at.% Y, (b) Mg-0.55at.% Y, (c) Mg-0.82at.% Y, (d) Mg-1.13at.% Y, (e) Mg-1.30at.% Y, (f) pure Mg.

3.3 Strain Rate Sensitivity Measurements

3.3.1 Strain Rate Sensitivity of Mg-Y alloys under tension.

The strain rate sensitivity (SRS) jumps were carried out by repeating the instantaneous rate change between 2.8x10^{-4} s^{-1} and 2.8x10^{-5} s^{-1} during deformation. The experimental data of strain rate sensitivity measurements are analyzed by the Haasen Plot. There are two important parameters determined from the Haasen Plot: (1) the engineering SRS parameter obtained from the slope of a given characteristic and (2) the thermal component of the flow stress given by the intercept of Haasen Plot with the Y-axis.

Figure 3.13 shows the tension Haasen Plot at 298K and 78K determined from stress down and stress rise jumps. The experimental data points have been fitted with a line to obtain the average values of the slopes and corresponding intercepts. The engineering strain rate sensitivity (ESRS) parameter, m, has been determined as the slope of these characteristics multiplied by deformation temperature. The variance of y-intercept and ESRS in regards to stress drop and stress rise are depicted in Figure 3.14. For 298K, the ESRS decreases from positive to negative as the solute content increases. The negative ESRS is attributed to dynamic strain aging. When the dislocation is arrested at solute atoms or solute clusters, solute atoms will diffuse along dislocations and create solute atmospheres. When the strain rate increases, dislocations escape from the atmospheres. Without the drag of solute atmospheres, less stress is required for continuous deformation. The negative ESRS is obtained under these conditions. The y-intercept for all Mg-Y alloys is positive, suggesting that solute-dislocation interactions greatly affect the flow stress behaviour. The intercept value is relatively unchanged as the solute content increases.

For 78K, the ESRS increases as the solute content increases. When the deformation

temperature decreases to 78K, the diffusion rate of Y is not enough to create solute atmospheres during the arrest time and positive ESRS arises under these conditions. The intercept values increase with increasing solute content, suggesting that the solute-dislocation interactions become more effective as the solute content increases.

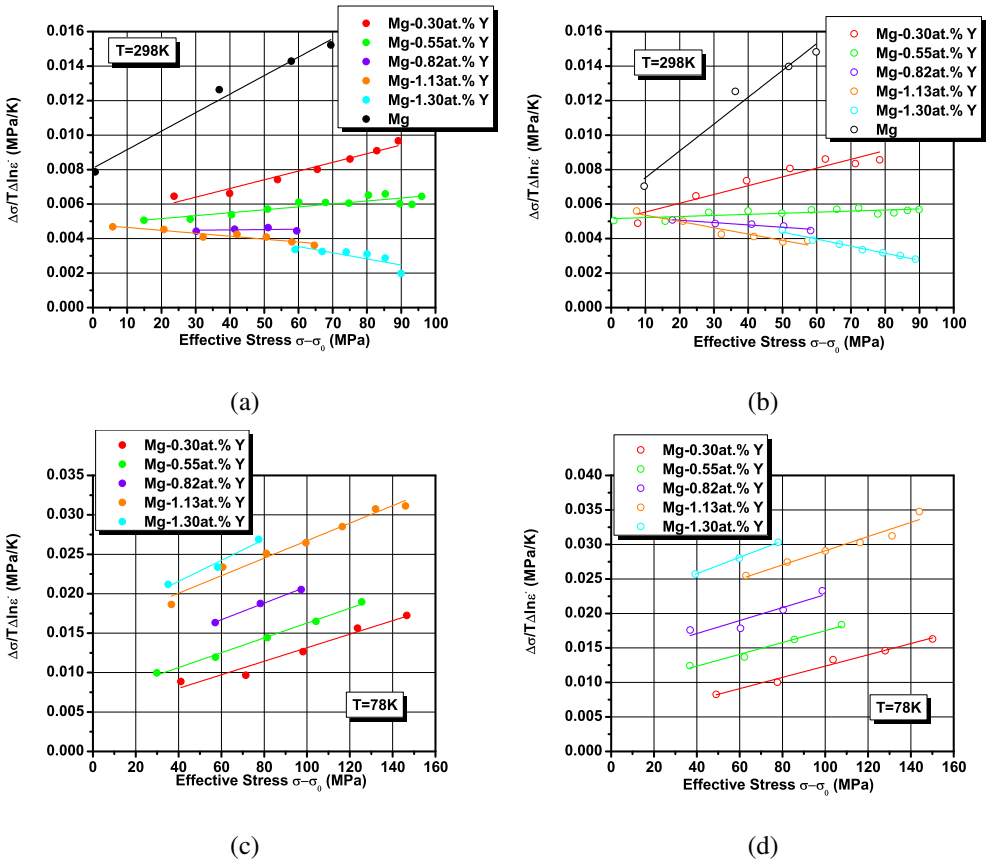

Figure 3.13: Haasen Plot characteristics obtained from ‘‘ jump down ” strain rate sensitivity tests under tension at (a) 298K and (c) 78K. Haasen Plot characteristic obtained from ‘‘ jump up ” strain rate sensitivity tests under compression at (b) 298K and (d) 78K.

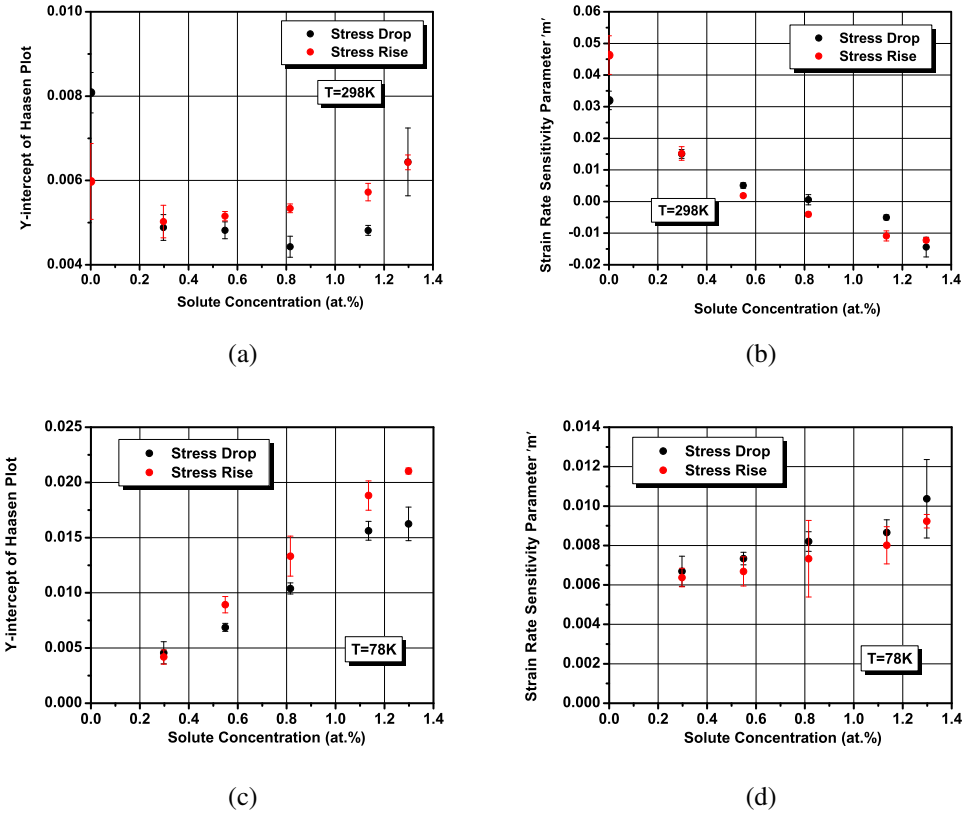

Figure 3.14: Haasen intercept values evaluated from ‘‘stress drop” and ‘‘stress rise” jumps at (a) 298K and (c) 78K. Engineering strain Rate Sensitivity parameter, m, of Mg-Y alloys obtained from ‘‘stress drop” and ‘‘stress rise” jumps under tension at (b) 298K and (d) 78K.

3.3.2 Strain Rate Sensitivity of Mg-Y alloys under compression.

Figure 3.15 shows the compression Haasen Plot at 298K, 78K and 4K determined from ‘‘stress down” and ‘‘stress rise” jumps. Figure 3.16 shows the variance of y-intercept and ESRS in regards to stress drop and stress rise.

For 298K, the ESRS decreases linearly from positive to negative as the solute content increases. The mechanism of the negative ESRS is the same as discussed above for alloys deformed under tension. The y-intercept increases with increasing solute content, suggesting that the solute-dislocation interactions become more effective as the solute content increases. For 78K and 4K, the ESRS for all alloys is positive and increases with increasing Y content. It is seen that also the intercept increases with increasing solute content.

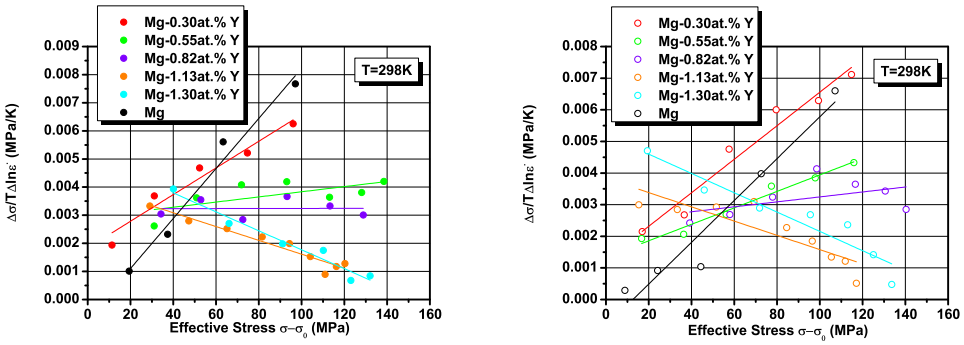

(a)

(b)

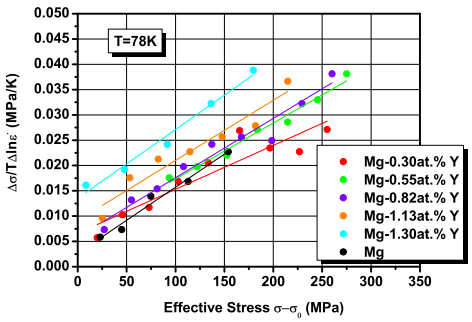

(c)

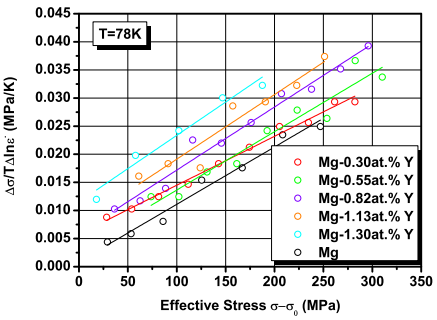

(d)

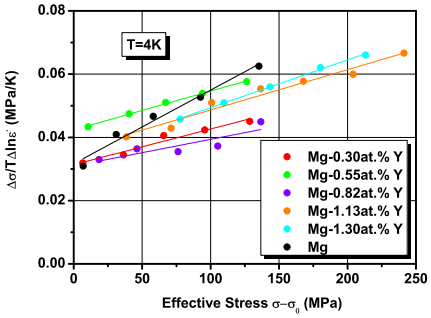

(e)

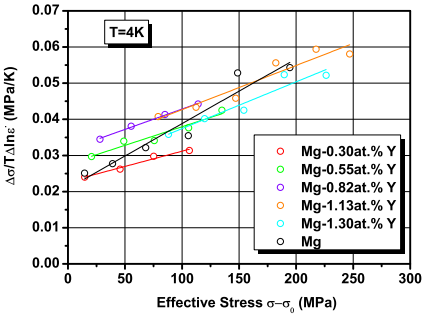

(f)

Figure 3.15: Haasen Plot characteristics obtained from ‘‘ jump down ” strain rate sensitivity tests under compression at (a) 298K, (c) 78K, (e) 4K. Haasen Plot characteristic obtained from ‘‘ jump up ” strain rate sensitivity tests under compression at (b) 298K, (d) 78K, (f) 4K.

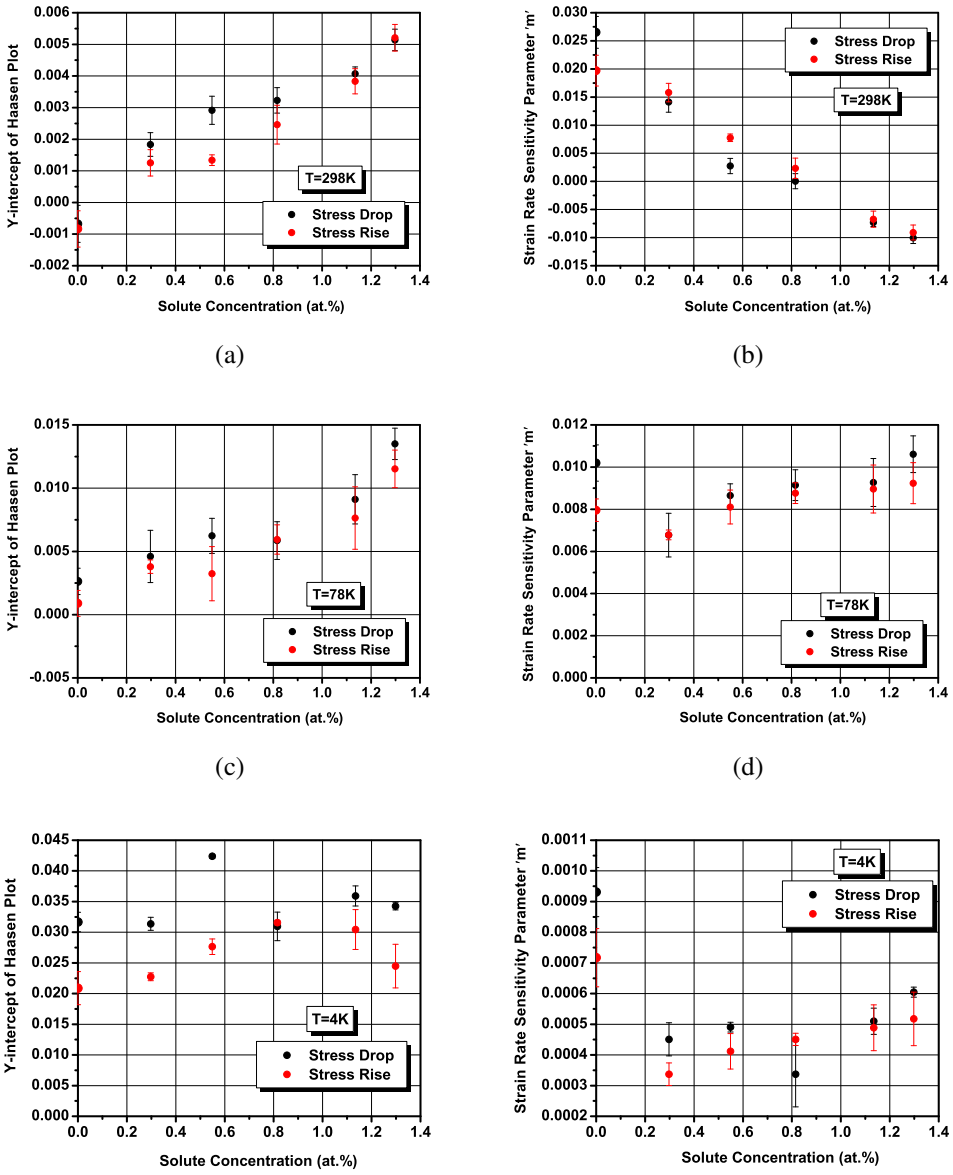

Figure 3.16: Haasen intercept values obtained from ‘‘stress drop” and ‘‘stress rise” jumps during compression test at (a) 298K, (c) 78K and (e) 4K. Engineering strain Rate Sensitivity parameter, m, of Mg-Y alloys obtained from ‘‘stress drop” and ‘‘stress rise” jumps under compression at (b) 298K, (d) 78K and (f) 4K.

3.4 Fracture Surface Analysis

Fracture surface analysis was performed on Mg-0.55at. %Y deformed under tension and compression. Figure 3.17 shows fracture surface of Mg-0.55 at. % Y alloys deformed under tension at 298K, 78K and 4K and compression at 298K and 78K (sample deformed under compression at 4K was not fractured).

The fracture surface of Mg-0.55 at. % Y alloy deformed at 298K (Figure 3.17a) exhibits a predominantly ductile character with a high density of micro-void areas present on the surface and some areas of the fracture occurring by cleavage. Both the high density micro-voids area and the sharp tearing ridges indicate that this quasi cleavage fracture mode is dominated by ductile fracture. When the deformation temperature decreases to 78K (Figure 3.17c), the fracture surface is still a mixture of micro-void areas and cleavage facets, but the density of voids decreases and the cleavage facets become flatter, suggesting that in this case, the fracture mode is dominated by cleavage mode. At 4K (Figure 3.17e), the fracture surface shows a brittle character with evidence of cleavage dominating the fracture surface. Particles are not apparent on the fracture surfaces of the samples, which indicate that particles do not initiate the fracture.

Fracture surfaces of Mg-0.55at. %Y deformed under compression show substantial differences than tensile fracture surfaces. The fracture surfaces of Mg-0.55 at. % Y alloy deformed under compression at 298K and 78K exhibit brittle character with cleavage facets (Figure 3.17 b and d). Even at 298K, no micro-voids area is observed. Ductile character of tearing range is observed in both 298K and 78K. The fracture surface of alloy deformed at 298K shows more layers (tearing ridges) in the cleavage facets. The sharper tearing ridges observed at higher deformation temperature indicates that the ductility decreases with the decreasing deformation temperature.

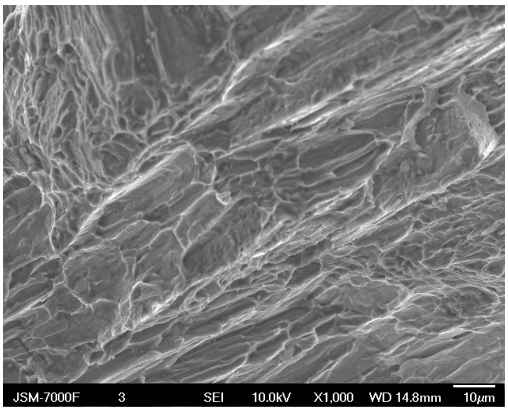

(a) Tension 298K

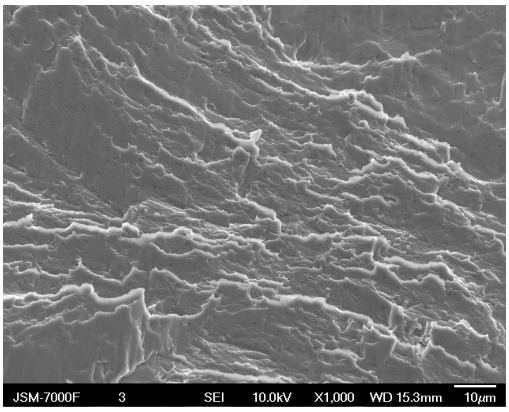

(b) Compression 298K

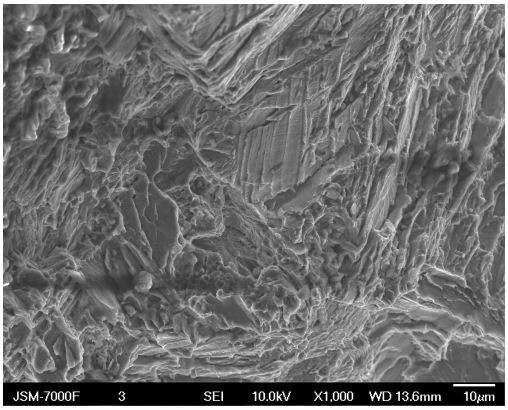

(c) Tension 78K

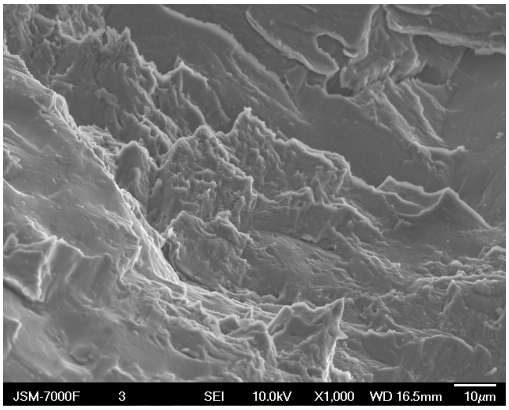

(d) Compression 78K

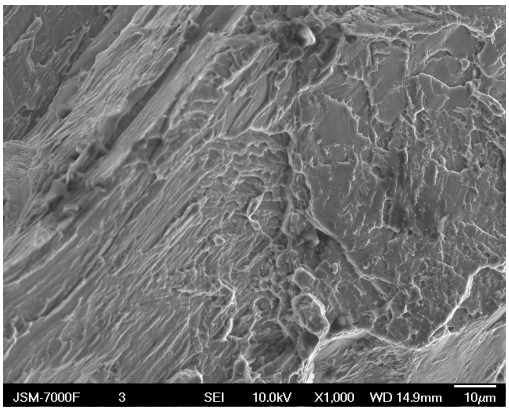

(e) Tension 4K

Figure 3.17: SEM observations of the fracture surface of Mg-0.55 at. % Y alloy series deformed under tension at (a) 298K (c) 78K (e) 4K and compression at (b) 298K and (d) 78K, at X1000 magnification.

3.5 Texture

Texture measurements were performed on the transverse section (Figure 2.3) of annealed and deformed samples. As mentioned in section 2.2, the samples were machined from the sheet with deformation axis parallel to rolling direction and the normal direction (ND) of the projection plane is parallel to the rolling direction of the sheet. The pole figure is indexed with respect to sheet axis systems as given in Figure 2.3.

The results of X-ray texture measurement for annealed Mg-Y alloys and pure Mg are presented by basal pole figures (Figure 3.18). It is seen that the texture formed during rolling procedure is retained in the sample subjected to recrystallization annealing. The intensity peaks appear around RD, indicating that c-axis is nearly perpendicular to ND, which is parallel to the rolling direction and deformation direction. This is the initial texture of the samples before deformation.

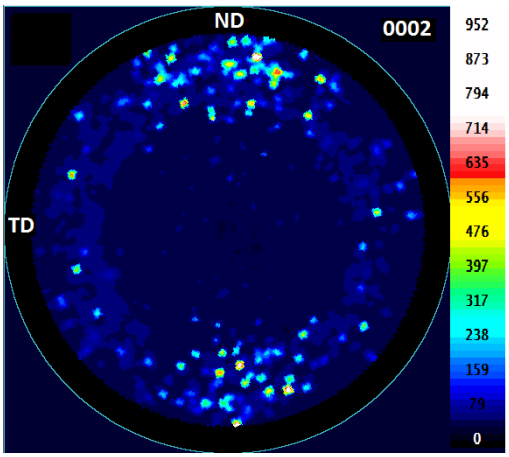

(a) Pure Mg

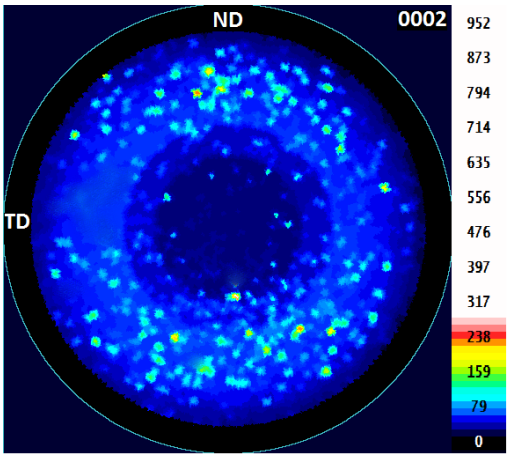

(b) Mg-0.30at.% Y alloy

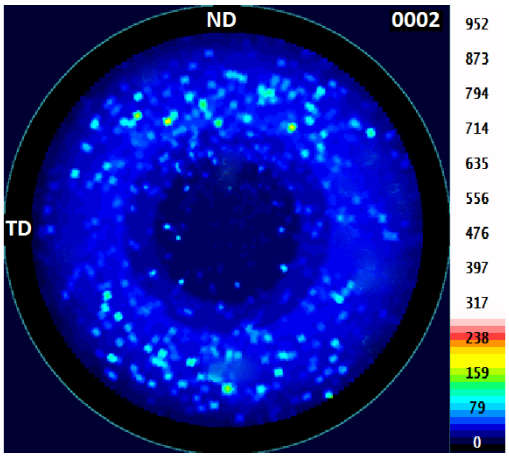

(c) Mg-0.55at.% Y alloy

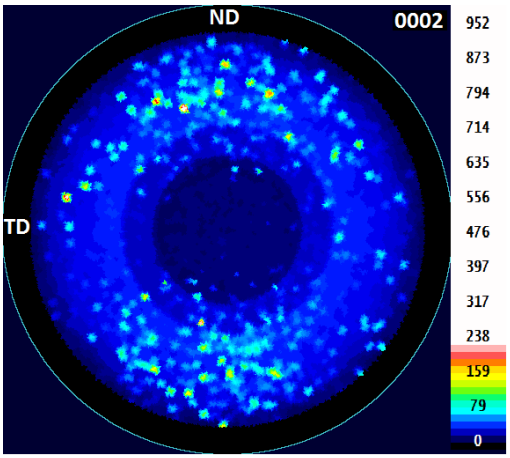

(d) Mg-0.82at.% Y alloy

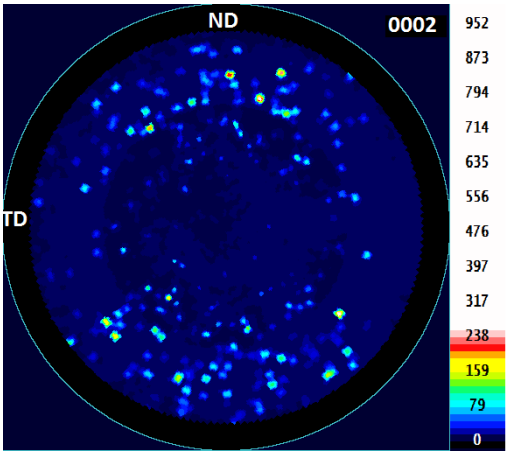

(e) Mg-1.13at.% Y alloy

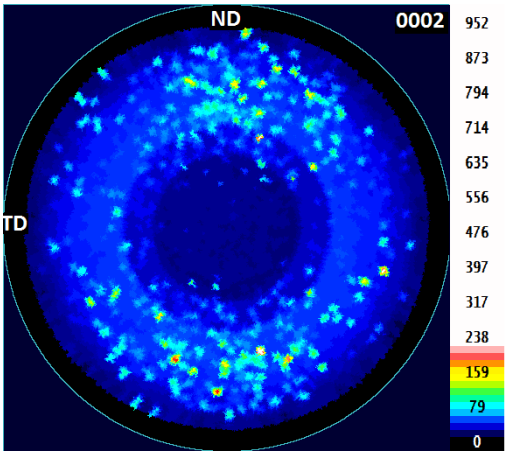

(f) Mg-1.30at.% Y alloy

Figure 3.18: Basal pole figures for pure Mg and Mg-Y alloys in as recrystallized state. Orientation of ND and TD directions is defined with respect to sheet axis system.

Figure 3.19 shows the basal pole figures of pure Mg and Mg-Y alloys deformed under tension at 298K. After the maximum tensile deformation, the intensity peaks around RD still exist, while the additional peaks in the neighbourhood of TD are observed. The additional intensity peak which is almost 90° rotated from the initial intensity peaks around RD, may be due to the $\{10\bar{1}2\}$ tension twins, whose misorientation angle is 86°.

For pure Mg, the intensity peaks along TD are almost as strong as the intensity peaks along RD, suggesting that certain amount of tension twins is formed during the tensile deformation. For Mg-Y alloys, the intensity peaks around RD are much stronger than those close to TD, indicating that the volume fraction of tension twins formed during tensile deformation is smaller than that observed in pure Mg.

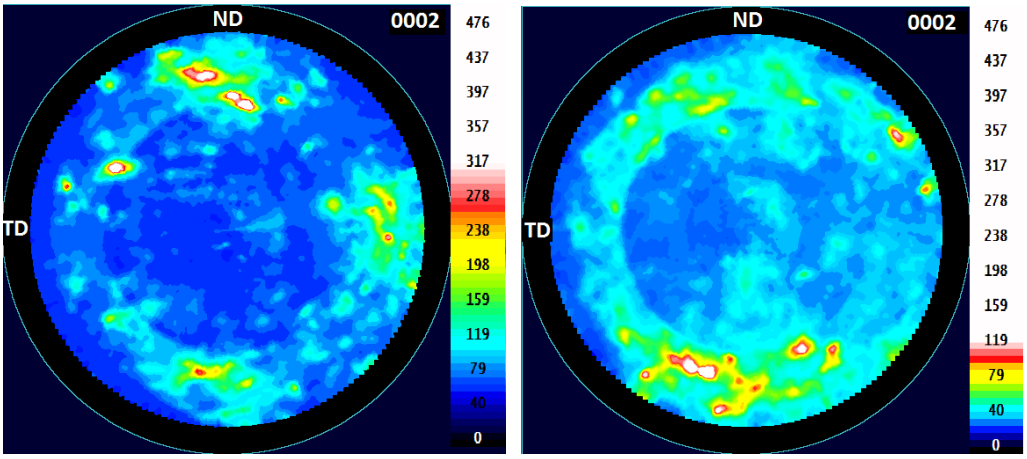

(a) Pure Mg

(b) Mg-0.30at.% Y alloy

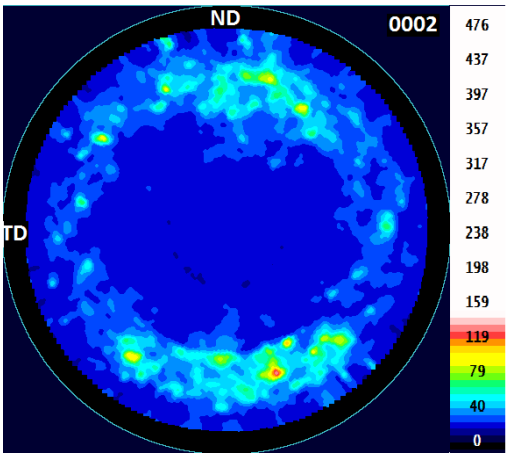

(c) Mg-0.55at.% Y alloy

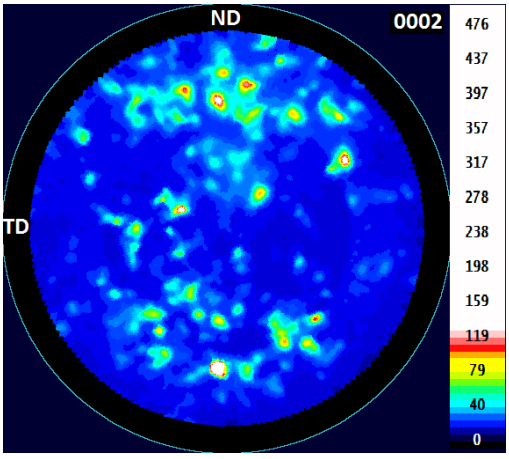

(d) Mg-0.82at.% Y alloy

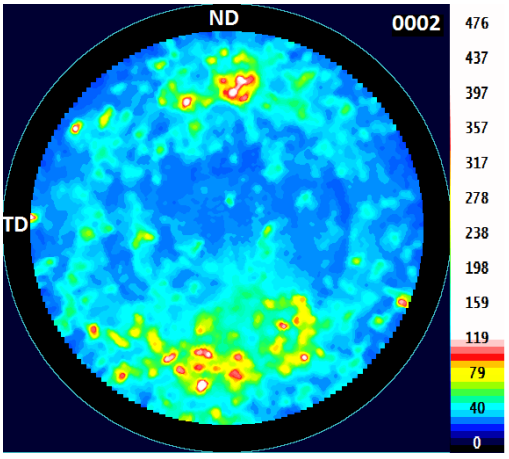

(e) Mg-1.13at.% Y alloy

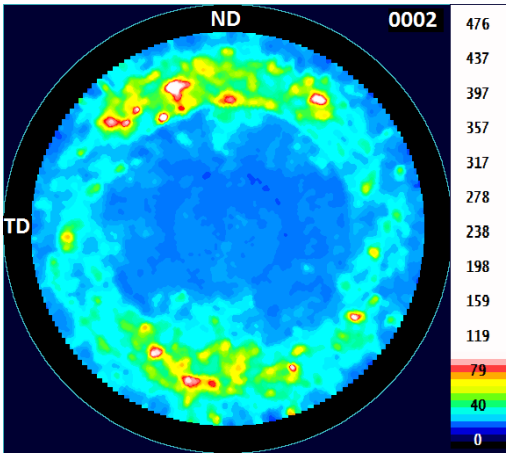

(f) Mg-1.30at.% Y alloy

Figure 3.19: Basal pole figures for pure Mg and Mg-Y alloys deformed under tension at 298K. Orientation of ND and TD directions is defined with respect to sheet axis system.

Figure 3.20 shows the basal pole figures of pure Mg and Mg-Y alloys deformed under compression at 298K. The basal pole figures for compression samples show substantial differences when compared with the pole figures of annealed samples or samples after tensile test. Basal texture was observed in all alloys and pure Mg after advanced deformation by compression, indicating that the c-axis is aligned almost parallel to ND. During compression deformation, c-axis is rotated nearly 90° from initially being perpendicular to ND to being parallel to ND. Under both tension and compression, pure Mg exhibits the strongest intensity among all samples, even though the deformation of pure Mg is the lowest, indicating that Y content weakens the texture by broadening the distribution of basal planes.

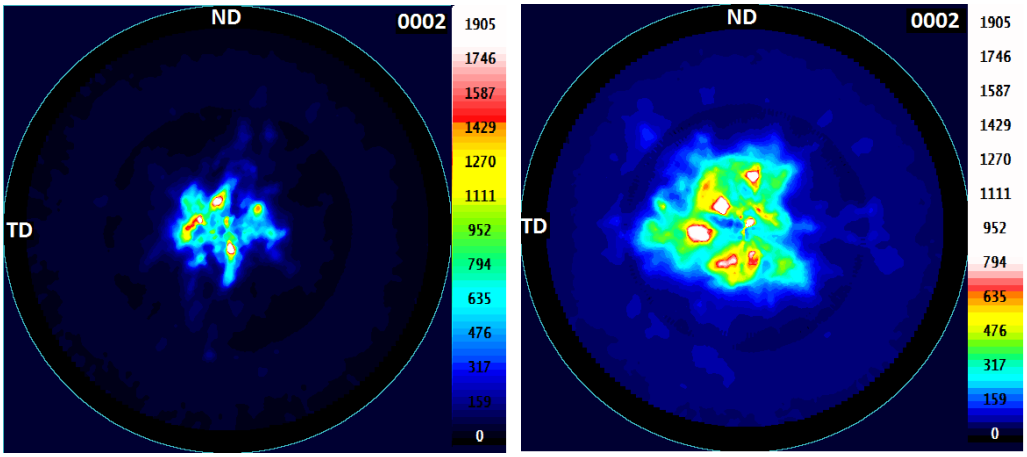

(a) Pure Mg

(b) Mg-0.30at.% Y alloy

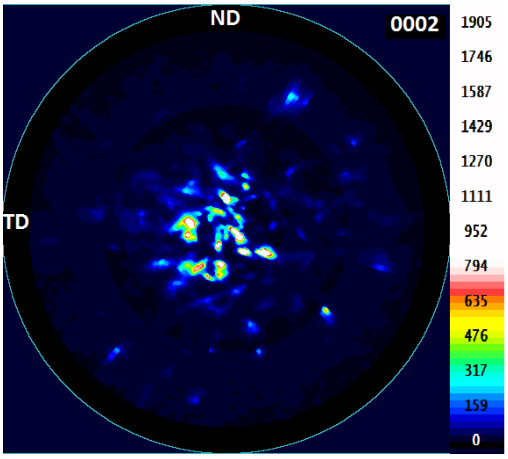

(c) Mg-0.55at.% Y alloy

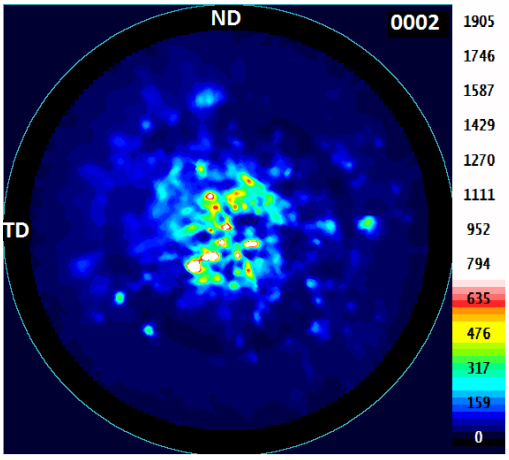

(d) Mg-0.82at.% Y alloy

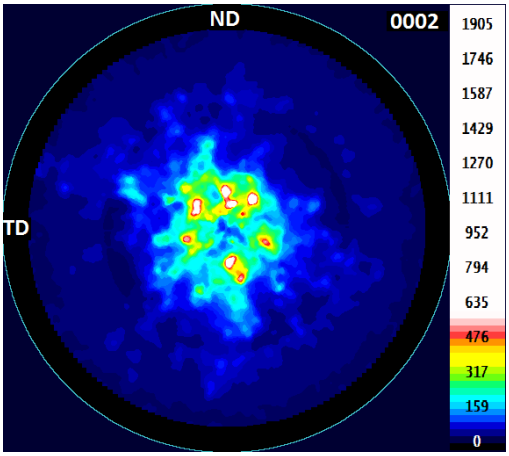

(e) Mg-1.13at.% Y alloy

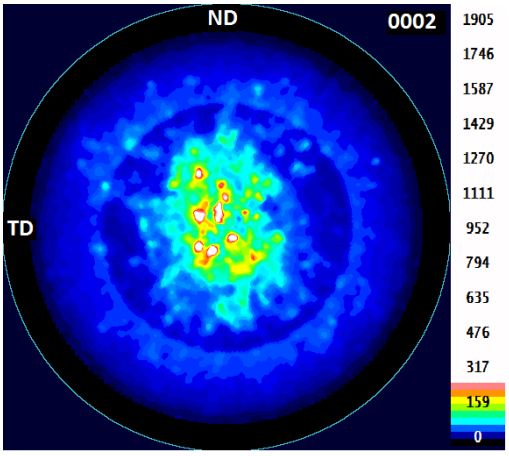

(f) Mg-1.30at.% Y alloy

Figure 3.20: Basal pole figures for pure Mg and Mg-Y alloys deformed under compression at 298K. Orientation of ND and TD directions is defined with respect to sheet axis system.

Figure 3.21 and Figure 3.22 show the basal pole figures of Mg-0.55 at.%Y alloys and Mg-1.13 at. %Y alloys compressed at different strains, respectively. After 3% compression, the texture has already changed (Figure3.21b and Figure3.22b). The intensity peaks along ND indicate that the orientation of some grains rotated 90° after only 3% deformation. This may be attributed to $\{10\bar{1}2\}$ tension twins. After 8% compression, strong intensity peaks around ND in addition to intensity peaks between RD and ND were observed (Figure 3.21c and Figure 3.22c). For 3% compression, the texture of Mg-0.55 at. % Y alloy and Mg-1.13 at.% Y alloy are similar. The texture of these two alloys shows differences after 8% deformation. The basal component seems stronger in Mg-0.55 at. % Y alloy than in Mg-1.13 at. % Y alloy.

Table 3.2 shows the volume fraction of twinning for Mg-Y alloys deformed under tension and compression at different strain levels. The volume fraction of twinning values show substantial differences in tension and compression. For tension, the volume fraction of twinning increases with increasing strain at the beginning of deformation, after 8% deformation, the volume fraction of twinning stays at the same level. For compression, the volume fraction of twinning increases rapidly with the increase of strain from the beginning of deformation to the end. For every strain level, the volume fraction of twinning for compression sample is larger than that of tension sample.

To determine the effect of Y on recrystallization texture, texture measurements were performed on another Mg-0.55 at. % Y alloy sample deformed under compression followed by annealing at 350°C for 5 min, 30 min and 1h. Figure 3.23 shows the basal pole figures for samples before annealing and after annealing for different times. After annealing for 5 min, the maximum intensity of the basal pole figure decreases a bit, while a large decrease of maximum intensity was observed after annealing for 30min. Further annealing does not

Table 3.2: Volume fraction of twinning in Mg-Y alloys.

Composition at.%	$3\%deformation$		$8\%deformation$		$Max deformation$	
	Tension	Compression	Tension	Compression	Tension	Compression
0.30	—	—	—	—	26%	82%
0.55	12%	27%	20%	85%	20%	93%
0.82	—	—	—	—	22%	95%
1.13	—	14%	—	24%	22%	85%
1.30	—	—	—	—	21%	56%

change the texture intensity. The results suggest that Y content weakens the texture during recrystallization process.

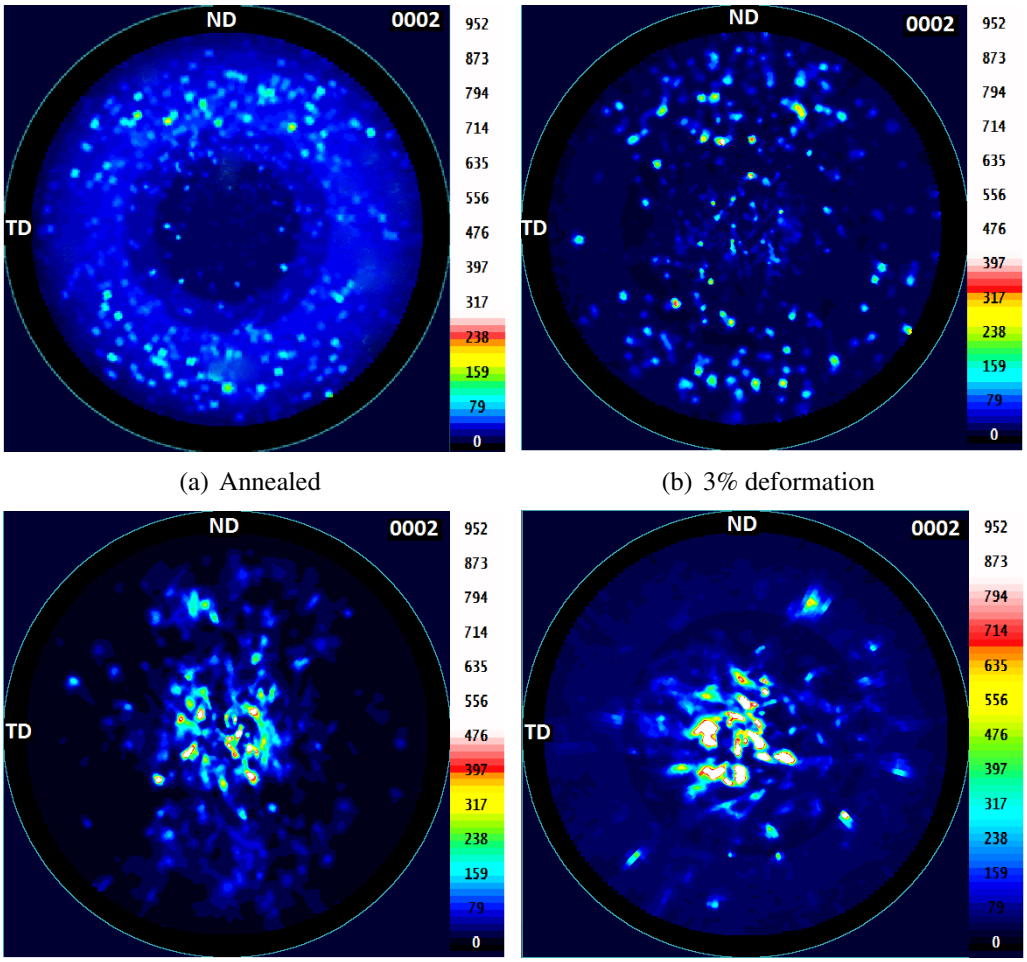

(a) Annealed (b) 3% deformation

(c) 8% deformation (d) Maximum (16%) deformation

Figure 3.21: Basal pole figures for Mg-0.55 at. % Y alloy deformed under compression at different strains at 298K. Orientation of ND and TD directions is defined with respect to sheet axis system.

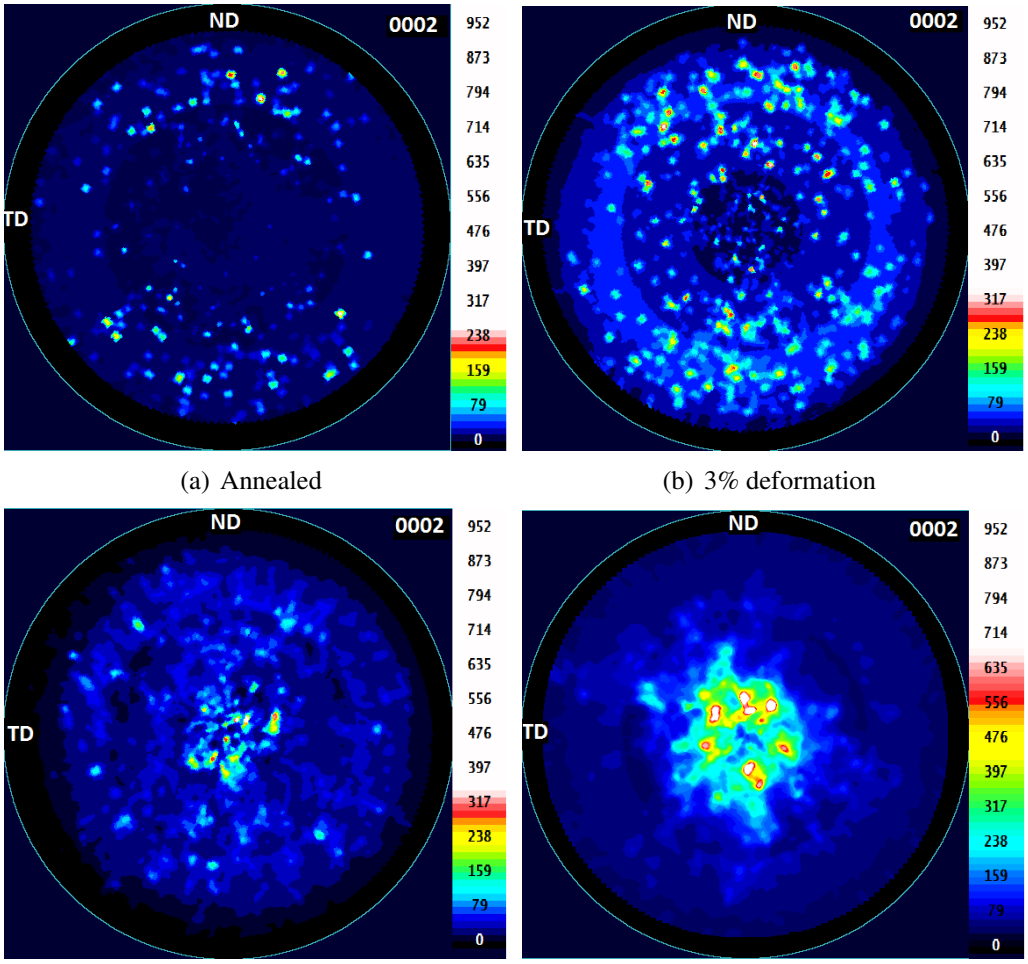

(a) Annealed (b) 3% deformation

(c) 8% deformation (d) Maximum (30%) deformation

Figure 3.22: Basal pole figures for Mg-1.13 at. % Y alloy deformed under compression at different strains at 298K. Orientation of ND and TD directions is defined with respect to sheet axis system.

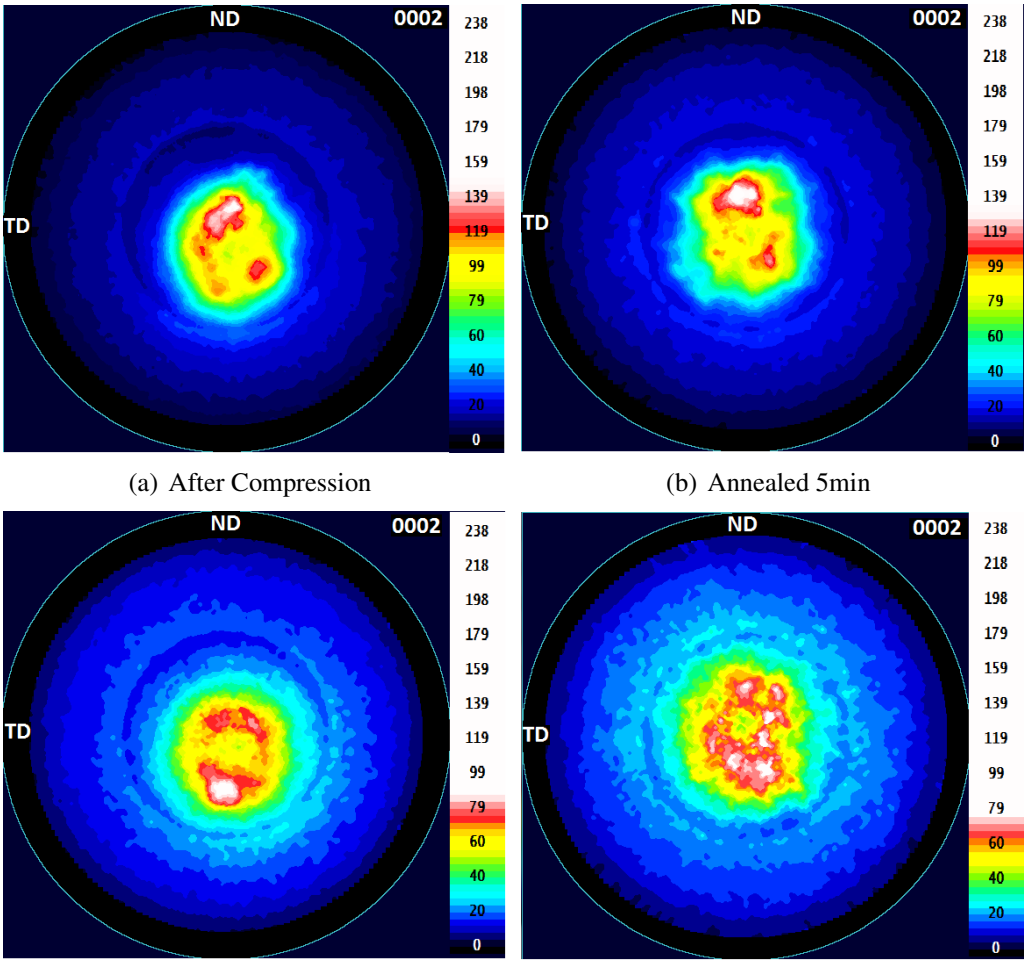

(a) After Compression (b) Annealed 5min

(c) Annealed 30min (d) Annealed 1h

Figure 3.23: Basal pole figures for Mg-0.55 at. % Y alloy deformed under compression at 298K followed by annealing for 5 min, 30 min and 1 h at 350°C. Orientation of ND and TD directions is defined with respect to sheet axis system.

Chapter 4

Discussions

4.1 Mechanical properties

4.1.1 Solid solution strengthening

There are several strengthening mechanisms in polycrystalline materials. The factors influencing the yield strength can be expressed by following equation:

$$\tau_y = \tau_0 + \tau_{gb} + \tau_{ss} + \tau_D + \tau_{ppt} + \tau_{texture} \tag{4.1}$$

τ_0 is intrinsic strengthening, which is related to atomic bond nature; τ_{gb} is grain boundary strengthening, τ_{gb} = k*$d^{-1/2}$, where k is a constant for a given material and d is the grain size of the material; τ_{ss} is solid solution strengthening, τ_{ss} = k*c^n (n = 2/3 (R.Labusch, 1970)); τ_D is dislocation strengthening, $\tau_D = \alpha Gb\rho^{1/2}$ (α = 0.3 (Ashby, 1970)), where G is shear modulus, b is Burgers vector and ρ is dislocation density; τ_{ppt} is precipitation strengthening, τ_{ppt} = Gb/2R, where R is radius of precipitate; $\tau_{texture}$ is texture strengthening. In order to focus on the effect of solid solution strengthening, the other contributions

must be controlled as much as possible.

The tensile yield strength of Mg-Y alloys studied in this work is presented in Figure 3.3. The tensile yield strength increases with the amount of solute content Y. The volume fraction of precipitates in Mg-Y alloys in this work is very small, so the major strengthening mechanisms are grain boundary strengthening and solid solution strengthening. In our system, the solid solution strengthening can be isolated by:

$$\Delta\sigma_s = \sigma_y - \Delta\sigma_{gb} \tag{4.2}$$

The grain boundary strengthening can be calculated by the Hall-Petch law:

$$\Delta\sigma_{gb} = \sigma_0 + kd^{-1/2} \tag{4.3}$$

σ_0 and k are parameters determined for the polycrystalline material, σ_0 = 11 MPa suggested by Hauser for pure Mg ((Hauser *et al.*, 1956)) will be used in the analysis. No detailed studies of Hall-Petch effects are available for Mg-Y alloys. According to the experiment, k values for pure Mg and AZ91 alloy range between 220 MPaμm$^{1/2}$ and 370 MPaμm$^{1/2}$; k = 300 MPaμm$^{1/2}$ suggested by Cáceres et al., (C.H.Cáceres & D.M.Rovera, 2001) will be used in the following analysis.

Table 4.1: Solid solution strengthening rate of Mg-Y alloys at 298K, 78K and 4K

Deformation Temperature	Strengthening rate $d\sigma/dc^{2/3}$
298K	1885
78K	3303
4K	3489

Figure 4.1 shows the experimental 0.2% proof strength and solid solution components of the strength of the Mg-Y alloys as a function of c^n at three different deformation temperatures. According to Fleischer and Labusch, n = 1/2 or 2/3, respectively. Based on the plot of $\ln(\Delta\sigma_s)$ as a function of ln(c), it is found that n = 2/3 is more appropriate for Mg-Y alloys studied in this work.

The solid lines of best fit and solid symbols represent the experimental 0.2% proof strength. The dashed lines and open symbols represent the solid solution component of strength. It is seen that the solid solution strength increases linearly with $c^{2/3}$. At low temperatures, the data points follow the $c^{2/3}$ better than at room temperature. The solid solution strengthening rate, which is the slope of the dashed lines of best fit, increases with the decreasing temperature. Table 4.1 summarizes the solid solution strengthening rate of Mg-Y alloys at three different temperatures.

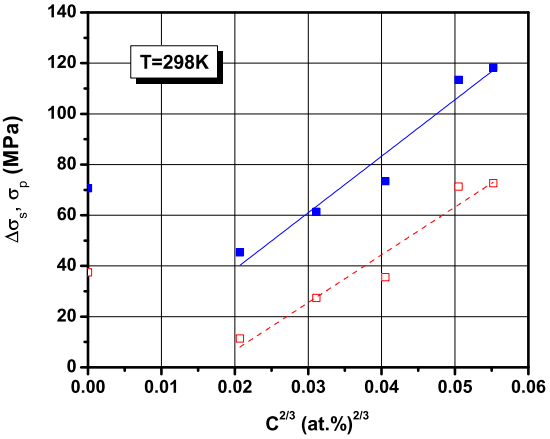

(a)

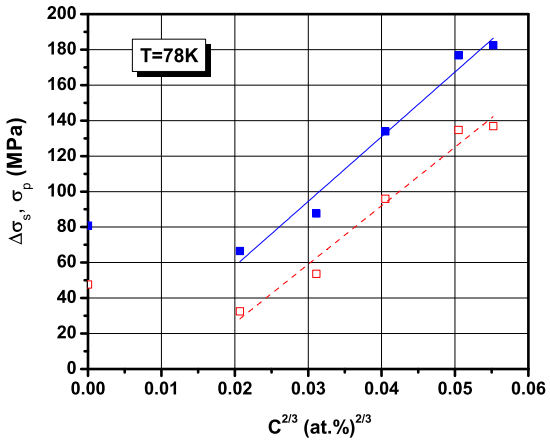

(b)

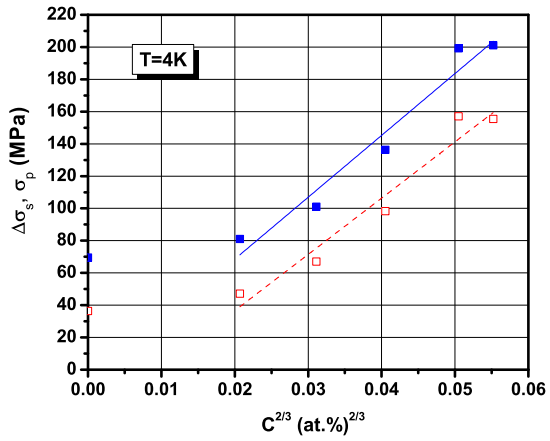

(c)

Figure 4.1: Experimental 0.2% proof strength (solid blue symbols) and solid solution strength (open red symbols) of the Mg-Y alloys as a function of $c^{2/3}$ at (a) 298K, (b) 78K and (c) 4K.

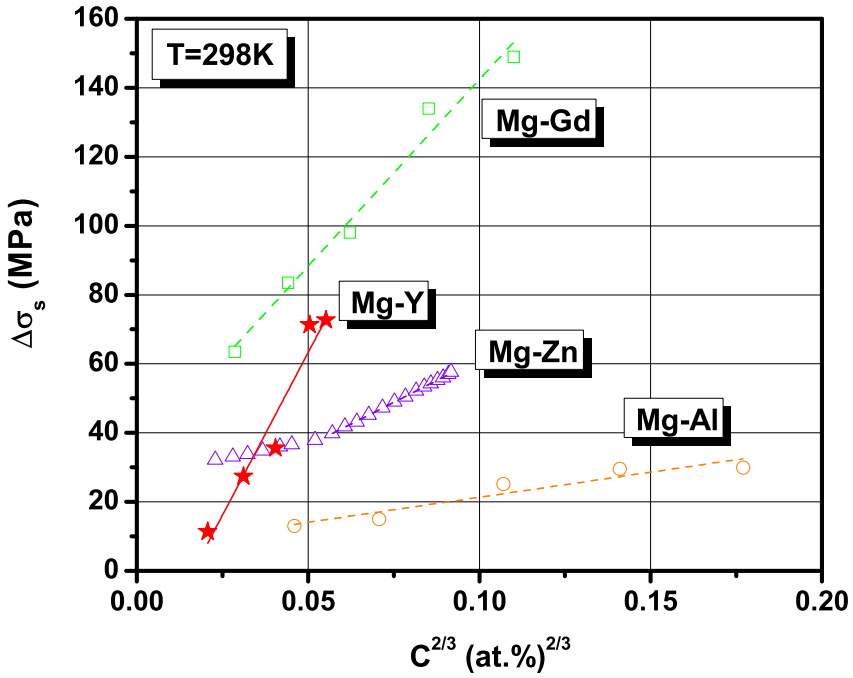

Figure 4.2: Solid solution strength of Mg-Y alloys compared with that of Mg-Gd alloys, Mg-Zn alloys and Mg-Al alloys as a function of $c^{2/3}$ at 298K.

Figure 4.2 shows the solid solution strength of Mg-Y alloys compared with that of Mg-Gd alloys, Mg-Zn alloys and Mg-Al alloys as a function of $c^{2/3}$. It is seen that the solid solution strengthening rate of Mg-Y is higher than that of Mg-Gd, Mg-Zn and Mg-Al alloys, suggesting that Y atoms are more efficient strengthening constituents than other elements.

As mentioned in section 1.4, the major contributions to the solid solution strengthening induced by random distribution of solute are: (a) size misfit, suggested by Mott and Nabarro (N.F.Mott & F.R.N.Nabarro, 1940) (b) modulus misfit, suggested by Fleischer (R.L.Fleischer., 1961) and Labusch (R.Labusch, 1970). According to Labusch, the relationship of alloying concentration and yield strength can be expressed as:

$$\sigma_{ys} = \sigma_0 + Z_L G(\delta^2 + \beta^2\eta^2)^{2/3} c^{2/3} \tag{4.4}$$

In this equation, σ_{ys} is yield strength, σ_0 is the yield strength of pure Mg, Z_L is a constant, G is shear modulus of pure Mg, δ is size misfit, β is a value between 1/20 and 1/16, η is modulus misfit. η can be approximately calculated by:

$$\eta = \frac{2(G_1 - G)}{G_1 + G} \tag{4.5}$$

where G_1 is the shear modulus of Mg-Y alloy and G is the shear modulus of pure Mg.

Table 4.2 summarizes the solid solution strengthening parameters for Y (this work), Gd (L.Gao *et al.*, 2009a), Zn (C.H.Cáceres & A.Blake, 2002) and Al (C.H.Cáceres & D.M.Rovera, 2001) atoms in Mg. The misfit parameters of Y and Gd are smaller than that of Al and Zn, which suggests that the solid solution strengthening rate of Y and Gd should be smaller than that of Al or Zn. However, the present results show the opposite trend. So the size misfit and modulus misfit cannot explain the solid solution strengthening induced by Y and some other rare earth elements, such as Gd. Chen and Boyle (Chen & P.Boyle, n.d., 2012) calculated the bond strength of some Mg-based alloys, including Y, Al, Zn, Gd and some other rare earth elements. Electron localized function (ELF) evaluations show that the bonds between Mg and Y are more localized and stronger than between Al and Zn. They suggested that the bond strength enhancement may be attributed to the hybridization between the d-orbital of Y and the p-orbital of Mg atoms. Stanford et al., (Stanford *et al.*, 2010) found the effect of Gd on strengthening prismatic slip systems in Mg-Gd alloys by modelling. They proposed that the rare earth element, Gd, has a tendency to increase the CRSS for prismatic slip in magnesium. Sandlöbes (S.Sandlöbes *et al.*, 2012) found the effect of Y on decreasing the intrinsic stacking fault I_1 energy (I_1SFE). So, there will be more stacking faults formed on prismatic plane, which is strong obstacles. The stacking fault will also resist dislocations cross slip from basal plane to prismatic plane. Consequently, the prismatic slip system strengthening may be attributed to the strengthening effect of stacking fault and the reduced cross slip of basal dislocations into the prismatic plane. It is suggested that the enhanced solid solution strengthening of Y in Mg may be attributed to valence effect and prismatic slip systems strengthening. The simulations incorporating the prismatic slip systems strengthening effects are in progress in our research group.

Table 4.2: Solid solution strengthening parameters for Y, Gd, Zn and Al atoms in Mg

Solute	$Misfits$		Strengthening rate
	δ	η	$d\sigma/dc^{2/3}$
Y	+11%	0.404	1885
Gd	+11%	0.247	1168
Zn	-17%	0.867	905
Al	-14%	0.419	196

Figure 4.3 shows the effect of Y on the hardness of Mg-Y alloys, the data for Mg-Al alloys are also included in the figure (C.H.Cáceres & D.M.Rovera, 2001). It is seen that the hardness increases approximately linearly with the increase of Y content. The increasing rate of hardness for Mg-Y alloys, which is the slope of the line of best fit, is significantly higher than that of Mg-Al alloys. According to the line of best fit, the relationship between concentration of Y and hardness can be expressed as:

$$H_{v0.1} = 43.59 + 21.33Y \tag{4.6}$$

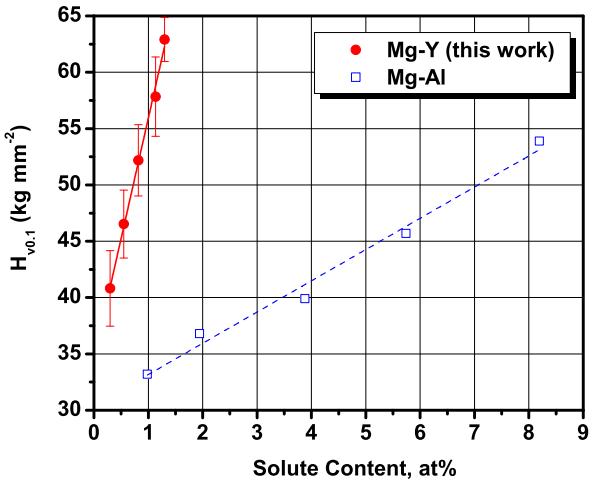

Figure 4.3: Effect of concentration of Y on the hardness of Mg-Y alloys. The data for Mg-Al alloys from Cáceres and Rovera are also included in the graph (C.H.Cáceres & D.M.Rovera, 2001).

4.1.2 Work-hardening behaviour

The work- hardening of engineering materials can often be expressed in terms of the Voce law

$$\Theta = \Theta_0(1 - \frac{\sigma}{\sigma_V}) \tag{4.7}$$

where Θ is work-hardening rate, Θ_0 is the athermal constant hardening term, σ is true stress and σ_V is Voce stress. According to Kocks and Mecking (U.F.Kocks & H.Mecking, 2003), various methods are available to determine σ_V. In this work, σ_V is determined from work-hardening vs. true stress plot by extrapolating the Stage III work-hardening to Θ=0. This corresponding intersection with true stress axis is the Voce stress, σ_V.

Figure 4.4 shows work-hardening rate normalized with respect to the shear modulus as a function of true stress normalized with respect to the Voce stress for individual alloys deformed under tension at different temperatures. Shear modulus, μ=1.64GPa, 1.84GPa, 1.86GPa for 298K, 78K and 4K are used in this work. Qualitatively, work-hardening behaviour for each alloy deformed at different temperatures is similar. It is evident that all the hardening curves for three temperatures fall into a quite narrow band for a wide range of stresses. The work-hardening behaviour can be expressed by one master curve, suggesting that the hardening behaviour can be predicted from two parameters: Θ_0 and σ_V, which may have important technological implications in the processing applications of these alloys.

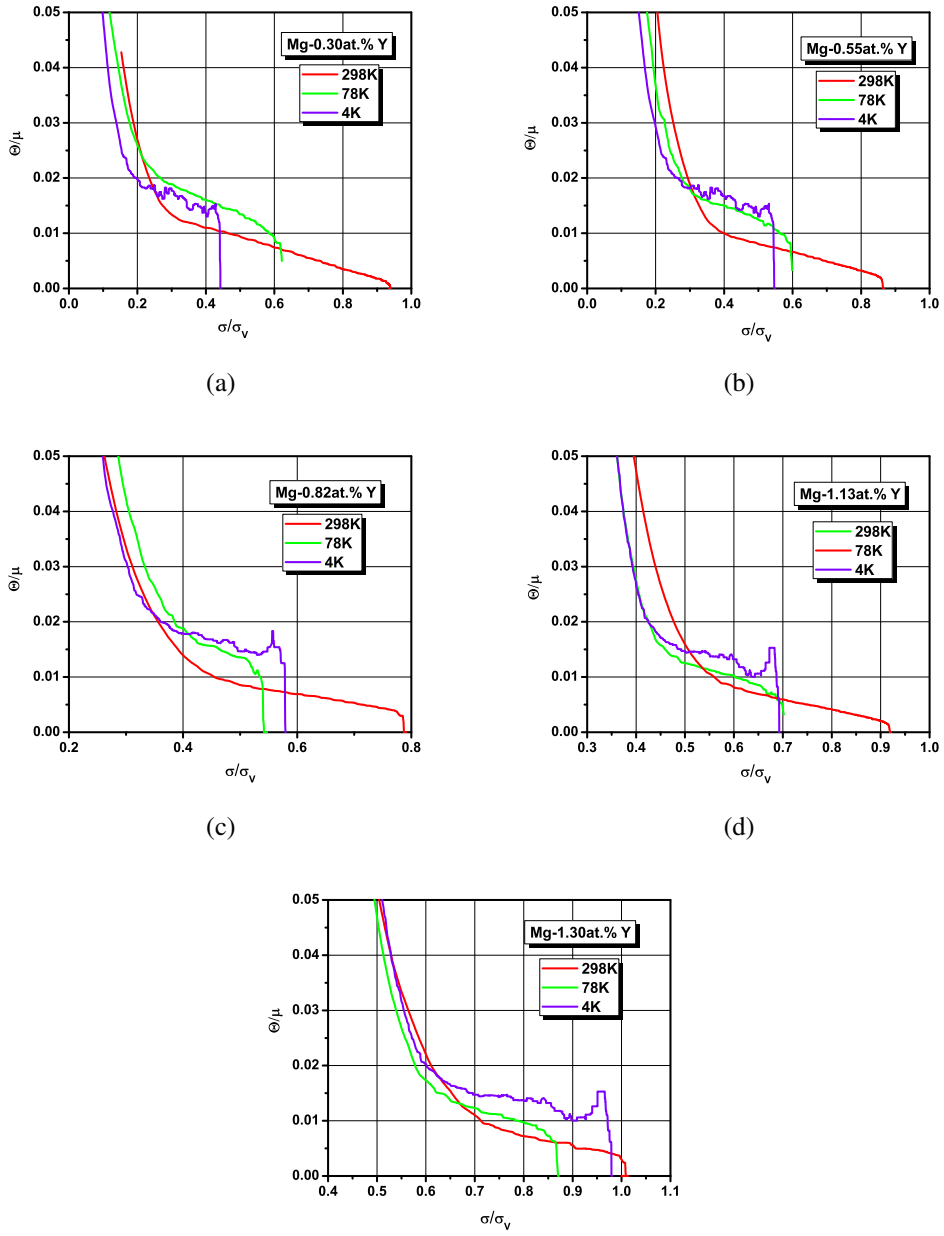

Figure 4.4: Normalized Θ-σ plots for Mg-Y alloys deformed under tension at 298K, 78K and 4K for different alloy compositions: (a) Mg-0.30at.% Y, (b) Mg-0.55at.% Y, (c) Mg-0.82at.% Y, (d) Mg-1.13at.% Y, (e) Mg-1.30at.% Y.

To account for the decrease of the work-hardening rate during plastic flow, Kocks and Mecking (U.F.Kocks & H.Mecking, 2003; H.Mecking & U.F.Kocks, 1981) suggested the mechanism of dynamic recovery which assumes thermally activated annihilation of dislocations dynamically during deformation. According to Kocks and Mecking the strain hardening rate encompasses two mechanisms:

$$\Theta = \Theta_0 - \Theta_r(\dot{\gamma}, T) \tag{4.8}$$

where Θ is the macroscopic-hardening rate, Θ_0 is the athermal constant hardening term, Θ_r is the dynamic recovery term, $\dot{\gamma}$ is shear rate and T is temperature. These two mechanisms operate from the beginning of deformation to the end. The first athermal term, giving constant contribution to the hardening, governs the work-hardening behaviour at low strains. The second term depends strongly on the temperature and mildly on strain rate and it is dominant at large strains.

For polycrystalline materials, Equation 4.8 can be re-written as:

$$(\sigma - \sigma_0)\Theta = (\sigma - \sigma_0)[\Theta_0 - \Theta_r(\sigma, \dot{\varepsilon}, T)] \tag{4.9}$$

where σ is the flow stress, σ_0 is yield stress and $\dot{\varepsilon}$ is strain rate. Figures 4.5 show Kocks-Mecking plots of all alloys deformed under tension at different temperatures. Kocks-Mecking plot is generated by using Equation 4.9. It is seen that the curves cut through the origin and show an approximately linear initial stage. The downwards curvature, observed at higher stress, follows the linear stage. The downwards curvature indicates the onset of dynamic recovery dominated deformation process. The downwards curvature occurs far before the ultimate tensile strength of these alloys, so it is not caused by nucleation

Table 4.3: Initial slope Θ_0 of Kocks-Mecking plots for Mg-Y Alloys under tension.

Composition at.%	298K (GPa)	78K (GPa)	4K (GPa)
Mg	3.3	5.5	3.0
0.30	1.5	3.0	3.1
0.55	2.2	3.1	3.7
0.82	2.3	3.5	3.8
1.13	2.1	4.3	5.3
1.30	2.6	4.5	4.7

of voids but it is likely that recovery is accelerated at a certain level of dislocation density.

Athermal storage of dislocation, Θ_0, can be measured as the initial slope of curves in the Kocks-Mecking plot. Table 4.3 shows the Θ_0 values of all alloys deformed under tension at 298K, 78K and 4K. The Θ_0 value increases with both the increase of Y content and the decrease of deformation temperature, indicating that the ability of dislocation storage increases with increasing Y content and decreasing deformation temperature. The larger Θ_0 value indicates more effective accumulation of dislocations in the substructure.

Figure 4.6 shows Kocks-Mecking plots for individual alloys at three different temperatures. The initial slopes of hardening curves for low deformation temperatures are much larger than those for the high deformation temperature, suggesting that the accumulation of dislocations is more effective at low deformation temperature. As deformation temperature decreases, the linear stage and downwards curvature shifts to higher stress, indicating that dynamic recovery process is suppressed at low deformation temperatures.

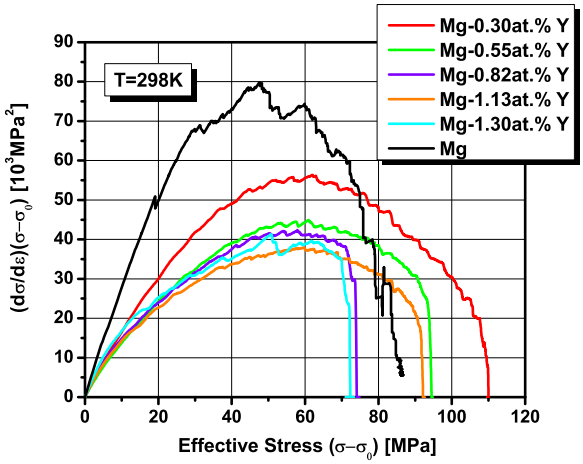

(a)

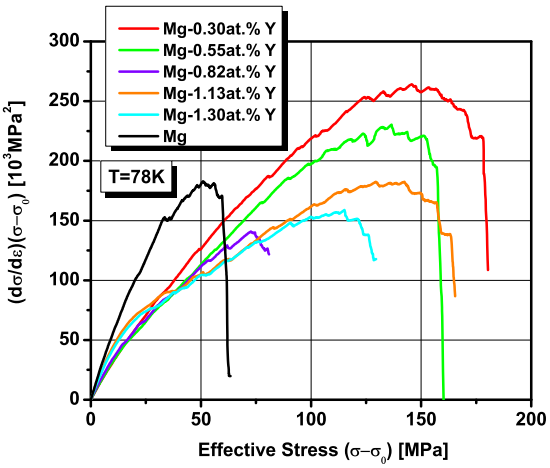

(b)

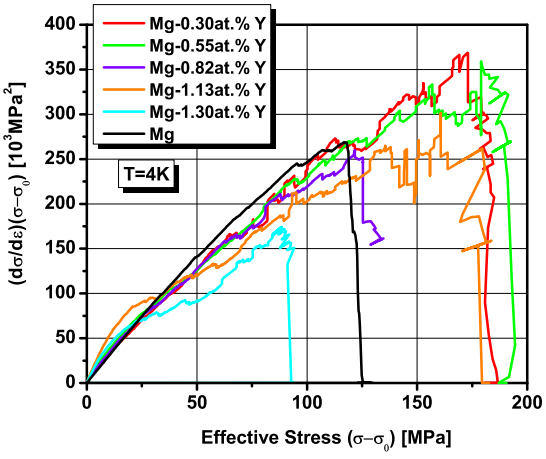

(c)

Figure 4.5: (σ - σ_0) Θ versus effective stress (σ - σ_0) characteristics for Mg-Y alloys deformed under tension at (a) 298K, (b) 78K and (c) 4K.

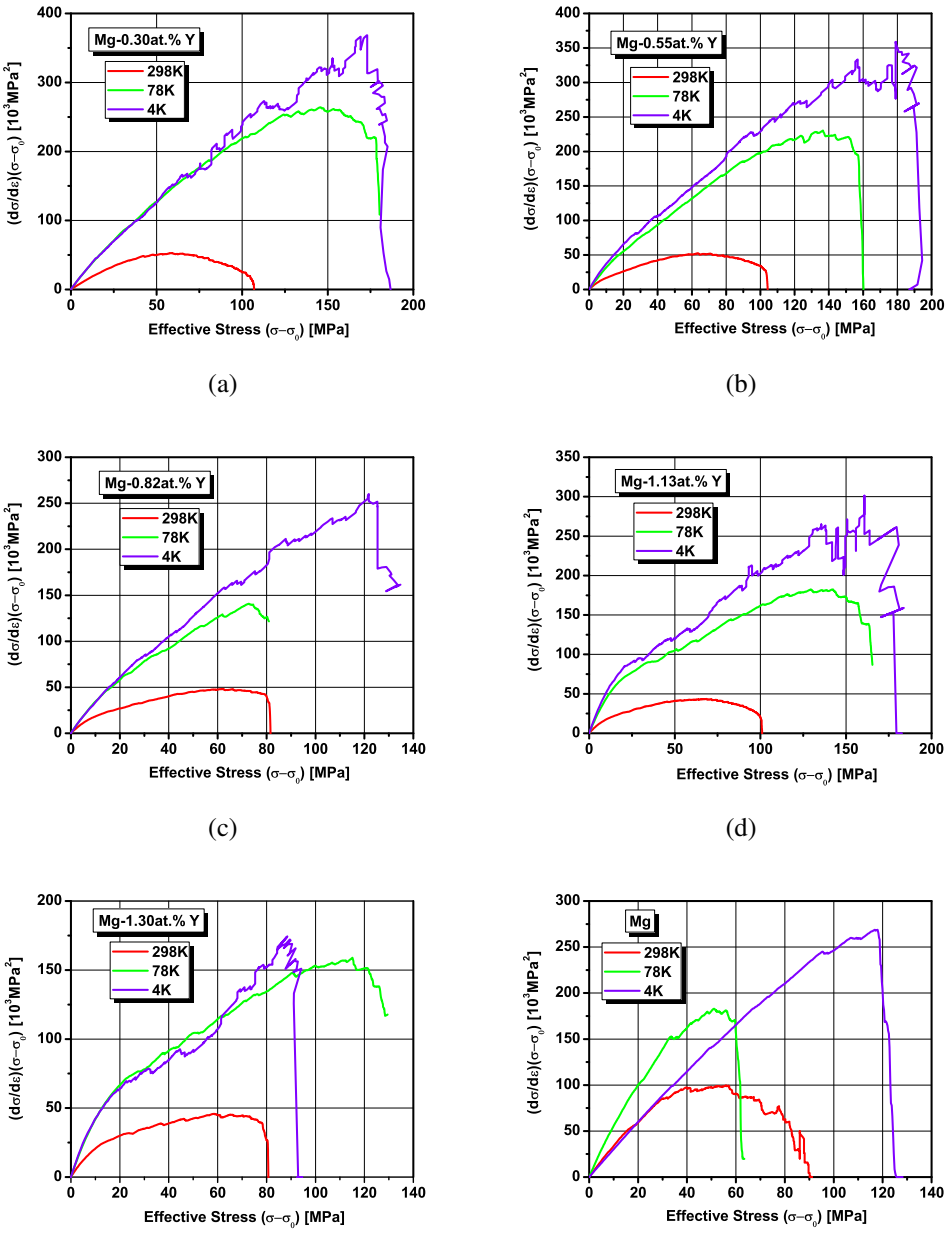

Figure 4.6: Comparison of (σ - σ_0) Θ versus effective stress (σ - σ_0) characteristics of Mg-Y alloys deformed under tension at 298K, 78K and 4K for different alloy compositions: (a) Mg-0.30at.% Y, (b) Mg-0.55at.% Y, (c) Mg-0.82at.% Y, (d) Mg-1.13at.% Y, (e) Mg-1.30at.% Y, (f) pure Mg.

Lukác and Balík (P.Lukác & J.Balík, 1994) proposed a model for evolution of work-hardening during deformation as a function of dislocation density in the following form:

$$\frac{d\sigma}{d\varepsilon} = K_1 + K_2\rho^{1/2} - K_3\rho - K_4\rho^2 \tag{4.10}$$

In this model, the multiplication of dislocation inducing strain hardening occurs due to the interaction between primary dislocation and forest dislocations, grain boundaries and precipitates. K_1 is associated with interaction of primary dislocations with grain boundaries and precipitates and K_2 is connected with interaction between primary dislocation and forest dislocations. The annihilation of dislocation inducing softening occurs due to cross slip and dislocation climb. K_3 relates to dislocation cross slip and K_4 is connected with dislocation climb. For polycrystalline materials, the stress dependence of work hardening rate can be re-written as:

$$\Theta = A/(\sigma - \sigma_0) + B - C(\sigma - \sigma_0) - D(\sigma - \sigma_0)^3 \tag{4.11}$$

where A relates to interaction between primary dislocations and non-dislocation obstacles; B is connected with the interaction of primary dislocation with forest dislocations; C relates to recovery induced by cross slip; D is associated with dislocation climb.

From Equation 4.11, we can get Equation 4.12:

$$\Theta(\sigma - \sigma_0) = A + B(\sigma - \sigma_0) - C(\sigma - \sigma_0)^2 - D(\sigma - \sigma_0)^4 \tag{4.12}$$

A is mainly influenced by precipitates. In this case, the volume fraction of precipitates in alloys is very small. From Kocks-Mecking plots, A is close to 0. Therefore, A = 0 is applied in this work. The climb of dislocations for Mg and Mg alloys deformed at room

temperature and lower temperatures can safely be neglected. In order to simplify the model, D = 0 is used in this work. Therefore, the relationship between $\Theta(\sigma - \sigma_0)$ and $(\sigma - \sigma_0)$ can be expressed as:

$$\Theta(\sigma - \sigma_0) = B(\sigma - \sigma_0) - C(\sigma - \sigma_0)^2 \tag{4.13}$$

As mentioned before, C relates to the annihilation of dislocations. C is affected by grain size, texture type, twinning and alloying elements. In this work, pure Mg and all Mg-Y alloys exhibit the same type of texture, rolling texture, and twinning is active in all samples. So, the effect of twinning and texture type can be neglected as independent variables. Dislocation multiplication and dislocation annihilation easily occur at grain boundaries. If a grain size is the major factor, high concentrated Mg-Y alloys with small grain size should have larger C values. According to table 4.4, the present work shows the opposite trend. The results indicate that alloying element strongly affects C values.

Figure 4.4 shows the simulation results of Kocks-Mecking plots for 298K and Table 4.4 summarizes the C values for pure Mg and all Mg-Y alloys deformed under tension at different temperatures. C values for alloys are much smaller than that of pure Mg. For Mg-Y alloys, C values decrease with the increasing Y content. The substitutional Y atoms inhibit the motion of dislocations. Therefore, dislocation annihilation process is retarded. The large decrease in work-hardening rate for pure Mg are due to the large C values.

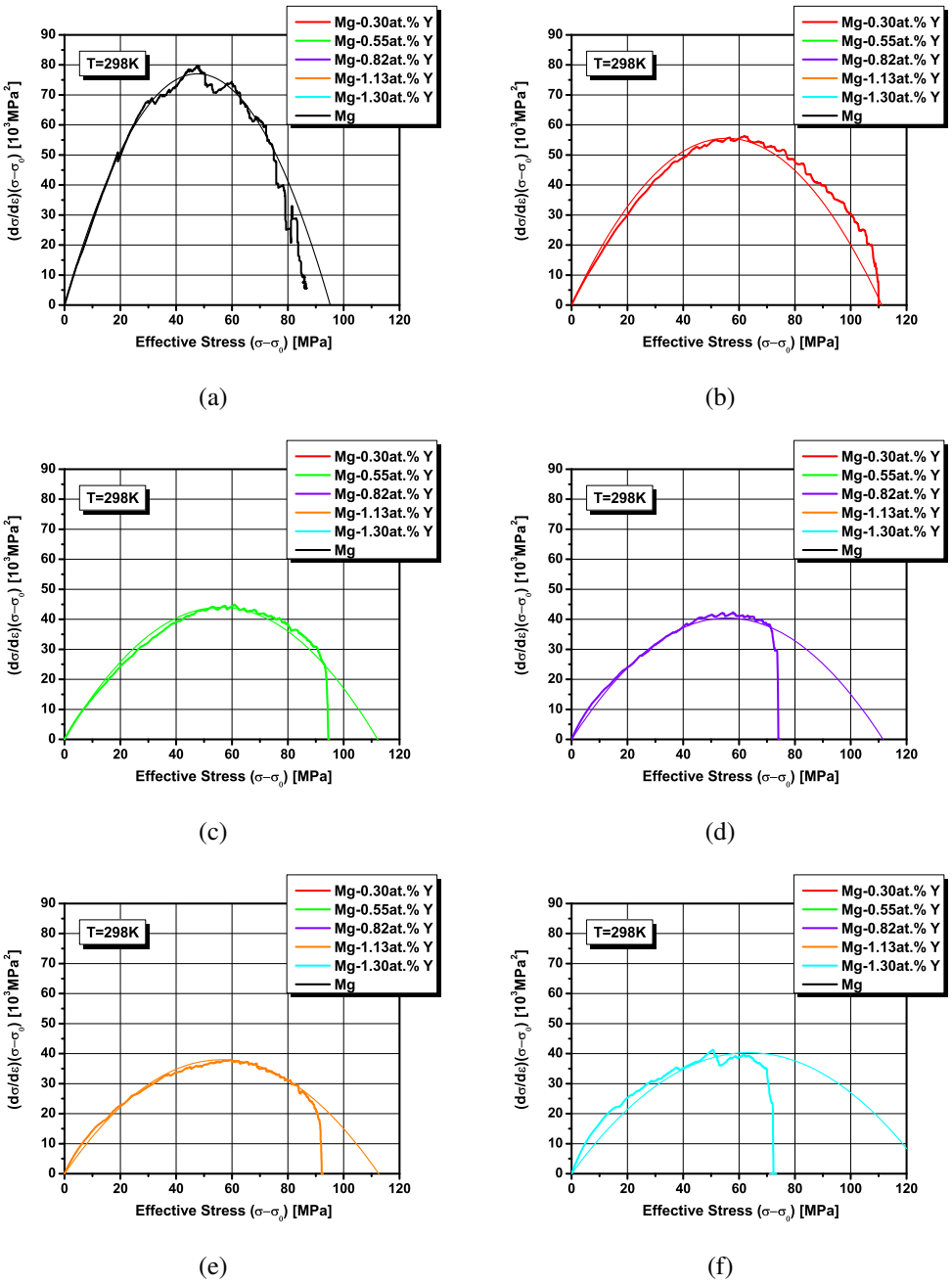

Figure 4.7: Simulated (σ - σ_0) Θ versus effective stress (σ - σ_0) characteristics for Mg-Y alloys deformed under tension at 298K.

Table 4.4: Parameter C for Mg-Y alloys deformed under tension at different temperatures.

Composition at.%	C (298K) MPa	C (78K) MPa	C (4K) MPa
Mg	34	70	24
0.30	18	14	12
0.55	14	13	11
0.82	13	12	10
1.13	12	9	8
1.30	10	8	7

Figure 4.8 shows Kocks-Mecking plots of all alloys deformed under compression at different temperatures. Compression characteristics show substantial differences than tension characteristics at low stress regions. Instead of one linear stage, compression curves intercept the origin, show first a linear stage and transition to a second linear stage with higher slope than the first one. Deviation from second linear stage is followed by downwards curvature at large stress.

X-ray data in Table 3.2 indicate that the second stage of high work hardening under compression is due to twinning process. Twinning happens at the beginning of compression deformation for both pure Mg and Mg-Y alloys. For pure Mg, the interaction of new-formed twins with existing twins and dislocations is very strong and the twin boundaries introduce strong barriers to the propagating dislocations and twining fronts. This increases work-hardening. Instead, in Mg-Y alloys, where the twinning activity is reduced and the slip occurs more frequently, the twin boundaries introduce less obstacles to the propagating dislocations and other twins. As a result, the slope of the second stage for pure Mg is larger than that of Mg-Y alloys.

Figure 4.9 shows comparison of tension and compression curves in Kocks-Mecking plots for individual alloys and pure Mg. The compression curves, depicted with C label, are shifted systematically to larger stresses than corresponding tension curves. The slope of the linear stage of tension curves is larger than the first linear stage of compression curves, but it is smaller than that of the second stage. The relationship between effective stress, σ - σ_0, and dislocation density, ρ, can be expressed as

$$\sigma - \sigma_0 = M\alpha\mu b\sqrt{\rho} \tag{4.14}$$

where: M is Taylor factor, μ is shear modulus and α is the constant. The athermal storage

of dislocation, Θ_0, can be expressed in terms of dislocation density and dislocation mean free path by Equation 4.15:

$$\Theta_0 = \frac{\alpha\mu}{2\Lambda\sqrt{\rho}} \tag{4.15}$$

where, as before α is the constant, μ is shear modulus, ρ is dislocation density and Λ is the dislocation mean free path. According to Equation 4.14, flow stress is determined by the dislocation density, ρ, stored in the sample, therefore, if two different alloys are deformed to the same stress level they expect to contain approximately the same dislocation density. Thus, Λ and Θ_0 scales as $\Lambda \sim 1/\ \Theta_0$. For compression, the Θ_0 is low at the beginning of deformation, indicating that the dislocation mean free path, Λ, is large at the beginning. The large Θ_0 observed at higher stresses indicates that Λ decreases with the increase of strain. Decreasing Λ correlates well with the twinning activity observed during this stage in compression and the fact that twinning introduces to the structure very effective obstacles, in the form of twin boundaries, that impede the motion of mobile dislocations.

Three independent mechanisms were proposed for the effect of twinning on strain hardening: (i) quasi Hall-Petch effect (A.A.Salem *et al.*, 2002; Niewczas *et al.*, 2001), (ii) texture effect (Kalidindi *et al.*, 2003; C.H.Cáceres *et al.*, 2008; Kaschner *et al.*, 2006), and (iii) Basinski et al. hardening mechanism (Basinski *et al.*, 1997; C.H.Cáceres *et al.*, 2008). For tension, X-ray measurements on Mg-Y alloys reveal that samples deformed until fracture contain a volume fraction of twinning in the range of 20%-26% (Table 3.2).Volume fraction of twinning increases with strain at the beginning of deformation, however, after 8% deformation, the volume fraction of twinning retains the same value. 20% volume fraction of twinning would be expected to change the work-hardening behaviour by increasing work-hardening rate after initial decrease. However, a continuously decreasing stage III work-hardening behaviour was observed in all Mg-Y alloys, suggesting

that none of the three hardening mechanisms for twinning has a strong effect on work-hardening behaviour for Mg-Y alloys deformed under tension, which is consistent with Bhattacharya (B.Bhattacharya, 2006) and Cáceres (C.H.Cáceres *et al.*, 2008) results. For compression, X-ray measurements on Mg-Y alloys reveal that samples deformed until fracture (or crack) contain a volume fraction of twinning in the range of 56%-95%, which is much larger than the volume fraction of twin phase produced under tension. The work-hardening rate for compression samples decreases slightly at the beginning of deformation, which is a common behaviour observed during propagation of twins, and then increases gradually at higher stresses. Based on Cáceres' analysis (C.H.Cáceres *et al.*, 2008), quasi Hall-Petch effect and Basinski et al. hardening mechanism do not have a strong contribution to the strain hardening during compression. Consequently, the increase of work-hardening rate is due to the texture hardening effect induced by twinning. In this case, both tensile and compressive stress are applied perpendicular to c-axis, indicating that slip and twinning is the dominant deformation mode for tension and compression, respectively.

Based on texture measurement, results it is seen that tension twinning rotates the c-axis of the twinned grains around ND direction towards TD direction (eg. Figure 3.19a) during tensile deformation. In this case, the tensile stress is still applied perpendicular to the c-axis of these grains and the newly-formed twins can be further deformed by dislocation glide. However, for compression samples, twinning transforms c-axis of the the twinned grains from ND direction to RD direction (Figure 3.20a-f), resulting in a compressive stress being applied parallel to c-axis of these grains. This requires a larger stress to deform the newly-formed twins under compression. In other words, large volume fraction of twins formed during compression act as hard particles in the polycrystalline sample and significantly increase the work-hardening rate after initial deformation. On the other hand, twins formed

under tension are most likely accommodation twins that are produced to accommodate the Poisson strain perpendicular to the tensile axis of the samples and they do not contribute to the work-hardening.

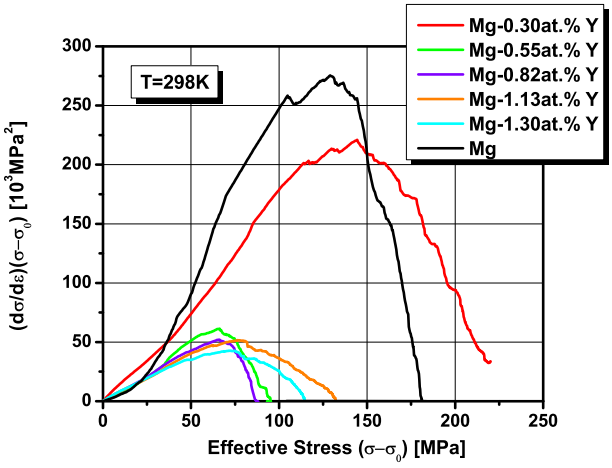

(a)

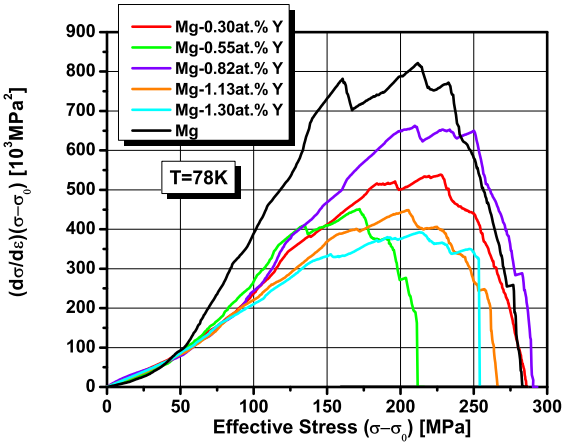

(b)

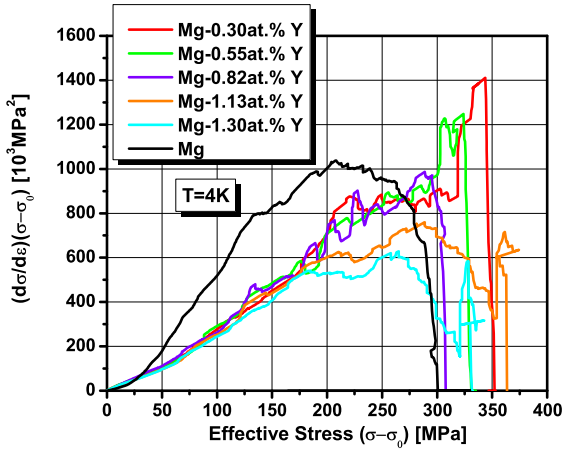

(c)

Figure 4.8: (σ - σ_0) Θ versus effective stress (σ - σ_0) characteristics for Mg-Y alloys deformed under compression at (a) 298K, (b) 78K and (c) 4K.

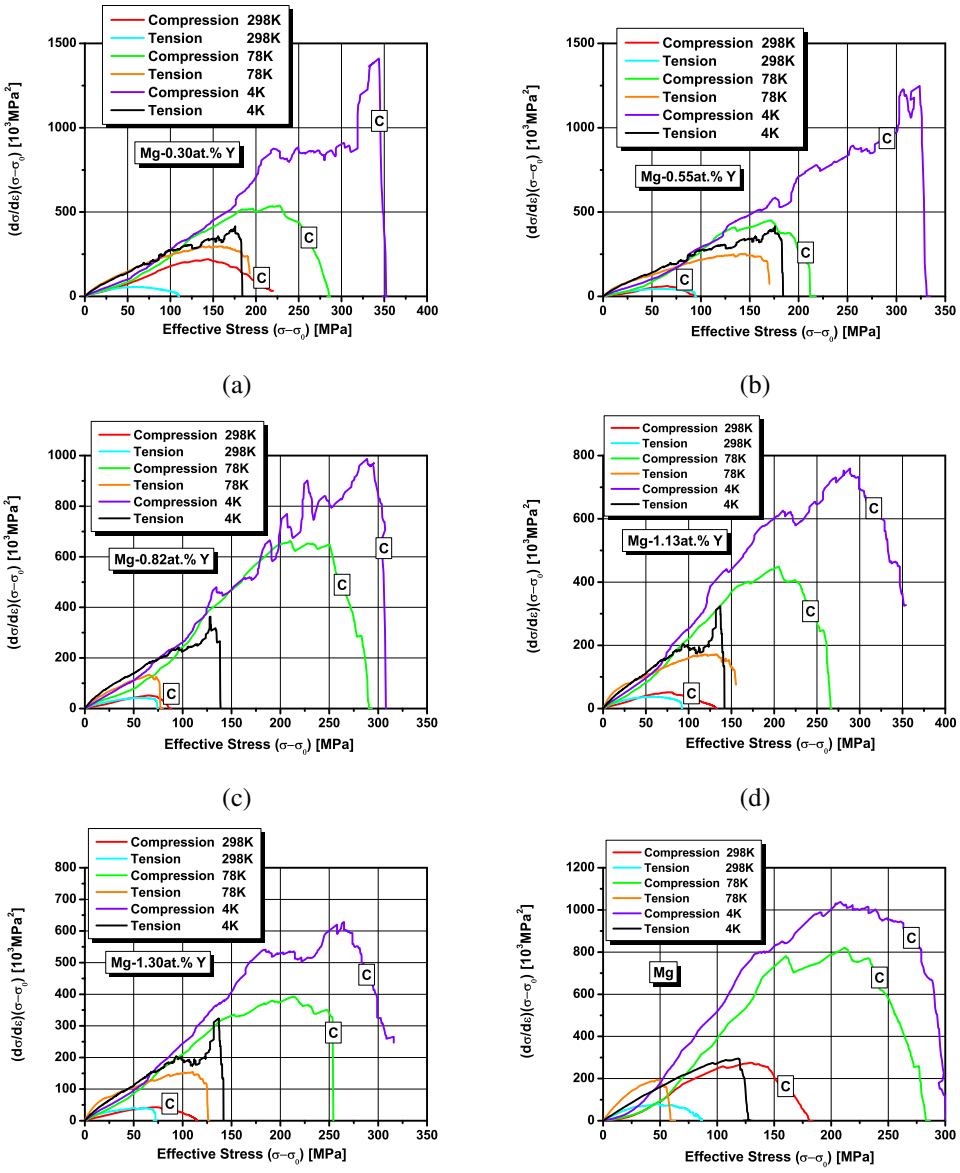

Figure 4.9: Comparison of (σ - σ_0) Θ versus effective stress (σ - σ_0) characteristics of Mg-Y alloys deformed under tension and compression at 298K, 78K and 4K for different alloy compositions: (a) Mg-0.30at.% Y, (b) Mg-0.55at.% Y, (c) Mg-0.82at.% Y, (d) Mg-1.13at.% Y, (e) Mg-1.30at.% Y, (f) pure Mg.

4.2 Strain rate sensitivity

The apparent activation area swept by dislocations during dislocation glide is calculated from the relationship:

$$\Delta a' = \frac{MkT}{b}\frac{\partial ln\dot{\varepsilon}}{\partial \sigma}|_{\Sigma,T} = \frac{MkT}{mb(\sigma - \sigma_0)} \tag{4.16}$$

where Taylor factor M=2.88, is used in this work. Apparent activation volume, another description of thermal activation of dislocation, can be calculated as:

$$\Delta V' = b\Delta a' = MkT\frac{\partial ln\dot{\varepsilon}}{\partial \sigma}|_{\Sigma,T} = \frac{MkT}{m(\sigma - \sigma_0)} \tag{4.17}$$

where Burgers vector b=0.3196 nm for basal dislocation is used in this work.

Figure 4.10 shows evolution of apparent activation volume for Mg-Y alloys as a function of effective stress deformed under tension at 78K. The right axis on the figures represents apparent activation volume normalized with respect to b^3, where b is Burgers vector. The apparent activation volume for all alloys shows similar trend. In all cases, the activation volume decreases at the beginning of deformation from about $120b^3$ to about 30-40 b^3. The apparent activation volume evaluated from stress rise and stress drop exhibit similar characteristics. The apparent activation volume shows strong dependence on solute atoms. The presence of Y content reduces the apparent activation volume.

Figure 4.11 shows evolution of apparent activation volume for Mg-Y alloys as a function of effective stress deformed under compression at 78K and 4K. In all cases, the apparent activation volume decreases with flow stress. The apparent activation volume decreases from about 210 b^3 to about 30 b^3 and from about 50 b^3 to about 18 b^3 at 78K and 4K, respectively. The apparent activation volume exhibits strong temperature dependence indicating that temperature helps in overcoming the obstacles that dislocations meet on their

paths. For example, at the effective stress of 50 MPa, the apparent activation volume for Mg-0.82at.%Y alloy determined from stress rise decreases from about 100 b^3 to about 31 b^3. For 78K, apparent activation volume for pure Mg is larger than that of Mg-Y alloys, once again, indicating that solute content reduces the apparent activation volume.

The apparent activation volume can be expressed as:

$$\Delta V' = b\Delta a' = bld = \frac{bd}{\sqrt{\rho}} = \frac{M\alpha\mu b^2 d}{\sigma - \sigma_0} \tag{4.18}$$

where b is Burgers vector, l is the average dislocation spacing, d is the activation distance, ρ is dislocation density, α is a constant, μ is shear modulus and M is Taylor factor. The activation distance can be calculated from the slope of apparent activation volume plotted as a function of the reciprocal of the effective stress. The slope of $\Delta V' = f(1/\sigma - \sigma_0)$ is proportional to $M\alpha\mu b^2 d$, thus activation distance, d, can be determined. In this analysis, α = 0.3, μ = 16.4 GPa, 18.4 GPa and 18.6 GPa for 298K, 78K and 4K, b = 0.3196 nm and M = 2.88 are used. The activation distance gives information about the dominant mechanism of thermally activated dislocation glide and is a fingerprint characterizing the strength of different obstacles.

The activation distance values for alloys deformed under tension at 78K and compression at 78K and 4K are depicted in Table 4.5. The activation distance for pure Mg is found as d$\sim$0.514b and d$\sim$0.065b at 78K and 4K, respectively. The value of activation distance, d$\sim$0.514b, is taken as a representative of the characteristic dislocation-dislocation interaction distance, although impurities present in Mg could also affect this value. According to Bhattacharya and Niewczas (B.Bhattacharya, 2006), the low d-value at 4K suggests that the obstacle structure is represented by a very narrow energy barrier, and the overcoming of such obstacle structure by mobile dislocations may be controlled by tunneling effects.

Table 4.5: Activation distance for Mg-Y alloys deformed under tension and compression.

Composition at.%	Tension	Compression	
	78K	78K	4K
Mg	—	0.514 b	0.065b
0.30	0.510 b	0.520 b	0.039 b
0.55	0.208 b	0.522 b	0.031 b
0.82	0.172 b	0.421 b	0.029 b
1.13	0.080 b	0.204 b	0.035 b
1.30	0.019 b	0.125 b	0.045 b

For 78K, in all cases, the activation distance decreases with increasing Y solute content, suggesting that solute atoms reduce the activation distance of dislocations. For pure Mg and Mg-Y alloys whose activation distance is around 0.5b, dislocation - dislocation interaction is the dominant mechanism of thermally activated dislocation glide. The effect of solute - dislocation interaction increases gradually with the increase of Y content. For 4K, it is difficult to find any trend of the activation distance as a function of Y, and all alloys consistently show the activation distance is in the range of 0.065b - 0.019b, suggesting that perhaps tunneling effects dominate the process of thermally activated obstacle passing.

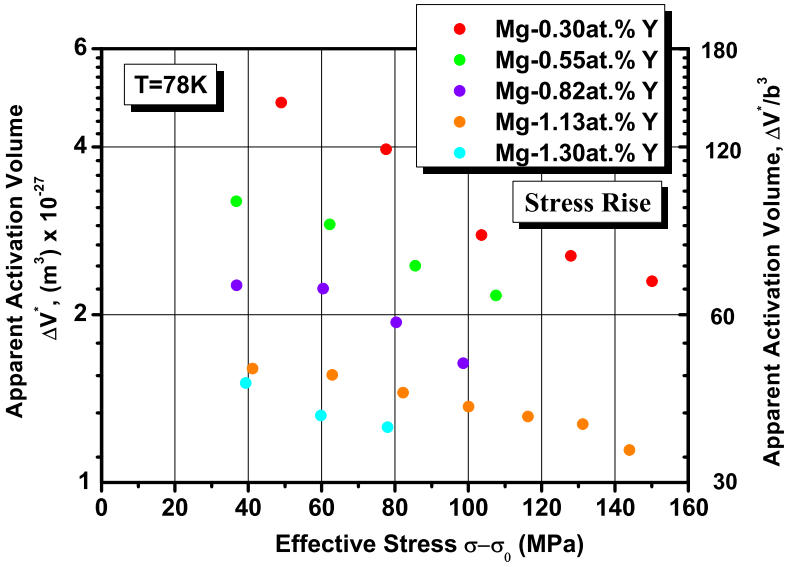

(a)

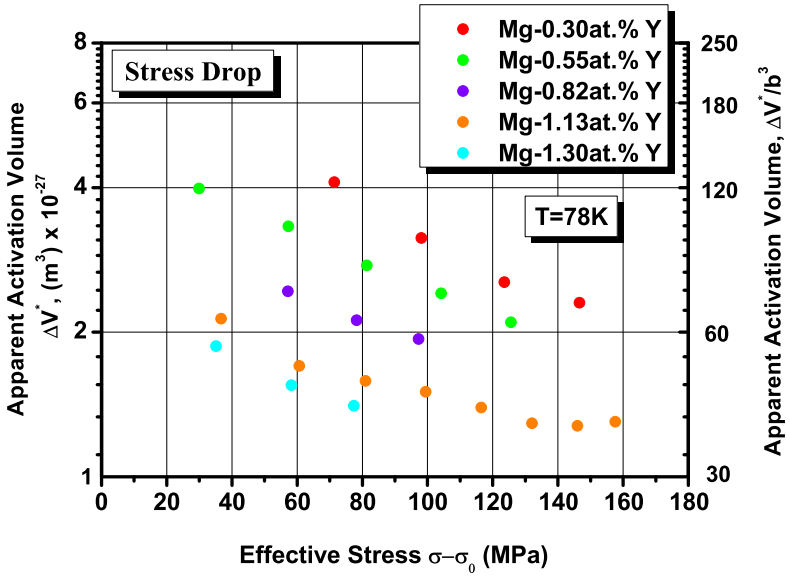

(b)

Figure 4.10: Apparent activation volume as a function of the effective flow stress on a log scale determined from (a) the stress rise and (b) the stress drops under tension at 78K.

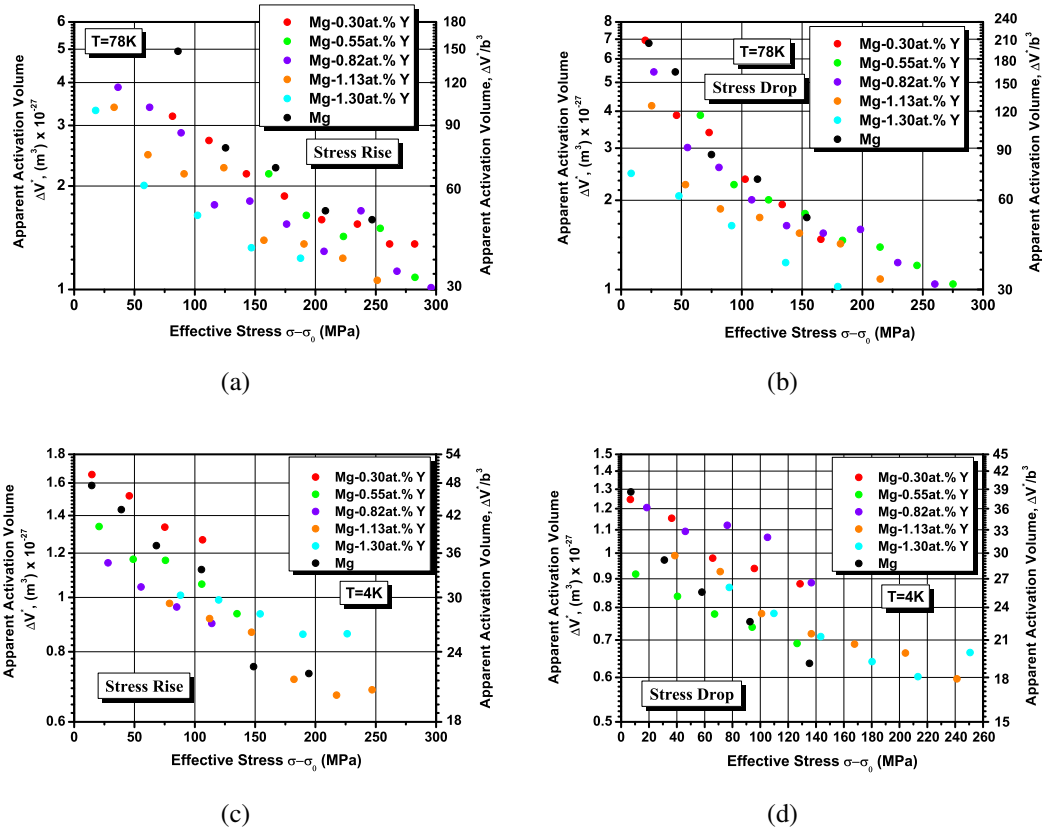

Figure 4.11: Apparent activation volume as a function of the effective flow stress on a log scale determined from (a) (c) the stress rise and (b) (d) the stress drops under compression at (a) (b) 78K, and (c) (d) 4K.

4.3 Texture

Figure 3.18, Figure 3.19 and Figure 3.20 show the texture of Mg-Y alloys before deformation and after deformation. Under the same conditions, the texture type of five Mg-Y alloys and pure Mg is similar to each other and the maximum intensity of texture components is similar. In order to analyze quantitatively evolution of the texture, the distribution of basal planes as a function of tilt angle from rolling direction (deformation direction) were calculated from orientation distribution function (ODF), calculated from incomplete pole figures using MTex software. The data points in the distribution of basal planes, represent the volume fraction of basal planes in the range of (θ-10)° to θ°.

Figure 4.12 shows the distribution of basal planes for annealed and deformed samples. For annealed samples, all alloys and pure Mg have the same initial texture, which is represented by the spectrum of basal poles in the range from 70° to 90° to the rolling direction. The distribution of basal planes for Mg-Y alloys are broader than that of pure Mg, which is consistent with the observation that the maximum intensity of pure Mg is higher than that of Mg-Y alloys. For compressed samples, all alloys and pure Mg have the same texture after compression, with the basal poles oriented in the range between 20° to 40° to the compression direction (rolling direction). Pure Mg exhibits the narrowest orientation distribution of basal planes, while the distribution of basal planes for Mg-Y alloys is much broader. Compared to pure Mg, the volume percent peak of Mg-Y alloys shifts towards higher angles and decreases with the increase of Y content, suggesting that the compression texture is weakened by Y content. For tension samples, all alloys and pure Mg have the same texture after tension and there is no obvious difference between pure Mg texture and alloys' texture.

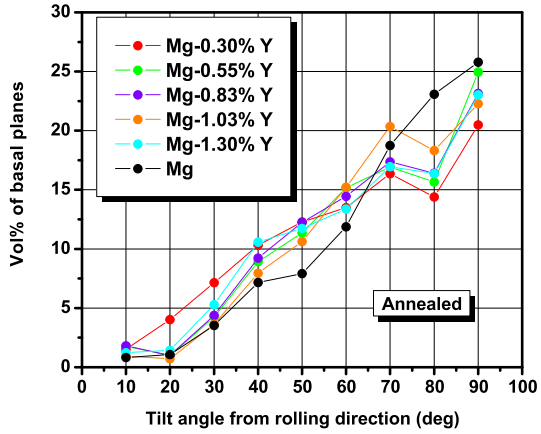

(a)

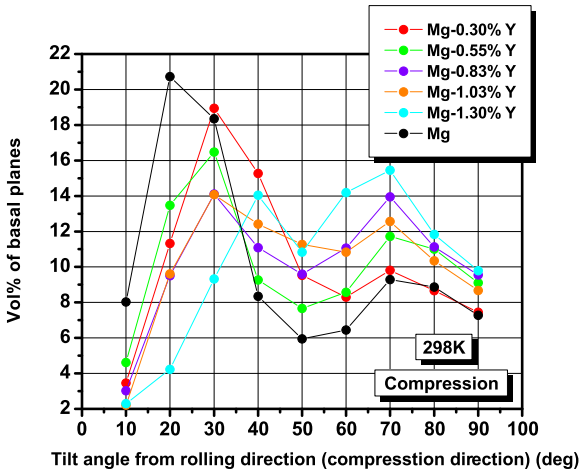

(b)

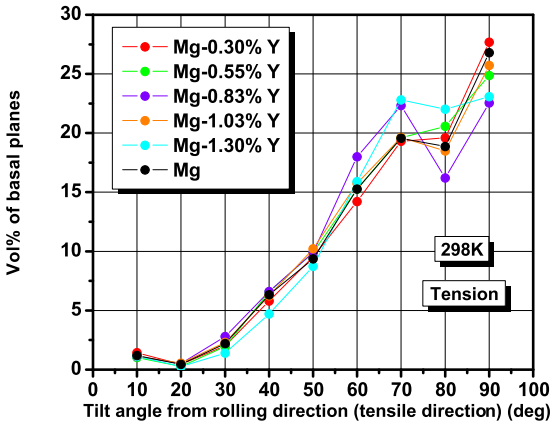

(c)

Figure 4.12: Volume percent of basal planes for (a) annealed, (b) compressed and (c) tensioned samples as a function of tilt angle from rolling direction.

Figure 4.13 shows the evolution of the distribution of basal planes during compression of Mg-0.55at. % Y and Mg-1.13at. %Y alloys. Texture was measured before deformation, after 3% deformation, after 8% deformation and after maximum deformation in compression corresponding to 16% strain and 30% strain, respectively. It can be seen that the volume percent peak of both alloys shifts from high angle to low angle as the strain rises, indicating that basal texture becomes stronger and stronger with increasing strain. The texture evolution trend of Mg-0.55at. % Y and Mg-1.13at. %Y alloys seems similar. If we compare the distribution curves of these two alloys at 3% deformation and 8% deformation, it can be seen that the distribution curves are similar after 3% deformation. However, after 8% deformation, the volume percent peak of Mg-0.55at. % Y alloy already moves to 30°, while the peak of Mg-1.13at. %Y alloy just moves to 70°. It is suggested that Y content retards the formation of basal texture in Mg-Y alloys. Twinning, especially tensile twinning, whose misorientation angle is 86°, induces a rapid rotation of grain orientation during compression, which contributes to the development of sharp basal texture. The Y alloying element, presumably decreases the activation energy of pyramidal slip, causing more slip systems and less twinning to be activated during compression. This conclusion will have to be verified independently by appropriate electron microscopy observations of the microstructure, which were beyond the scope of this work.

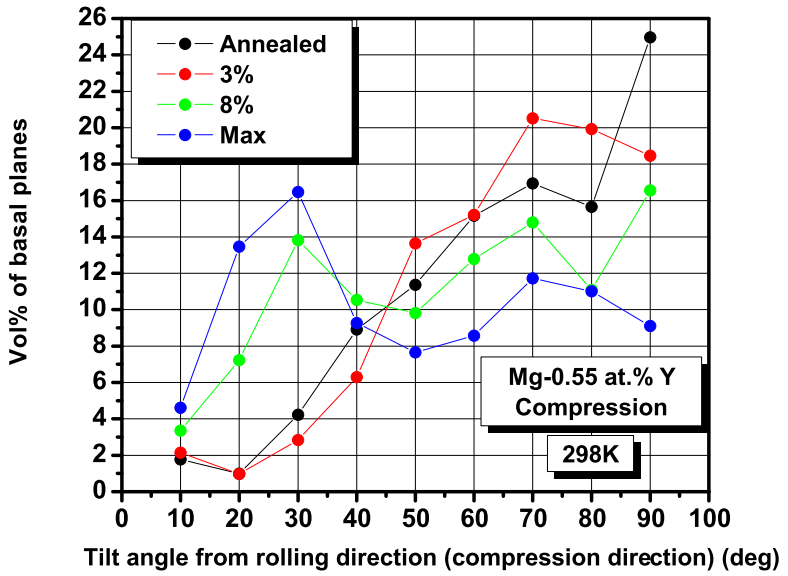

(a)

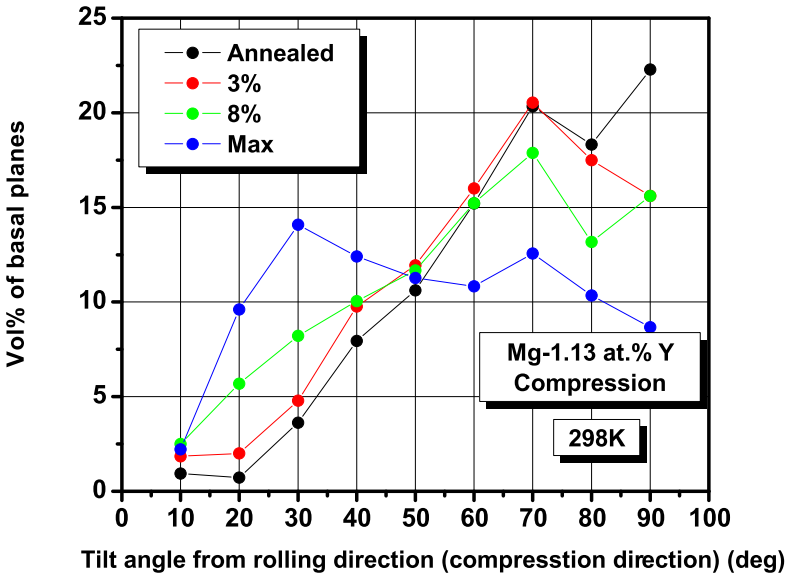

(b)

Figure 4.13: Volume percent of basal planes for (a) Mg-0.55at. % Y and (b) Mg-1.13at. %Y alloys at different strains as a function of tilt angle from rolling direction.

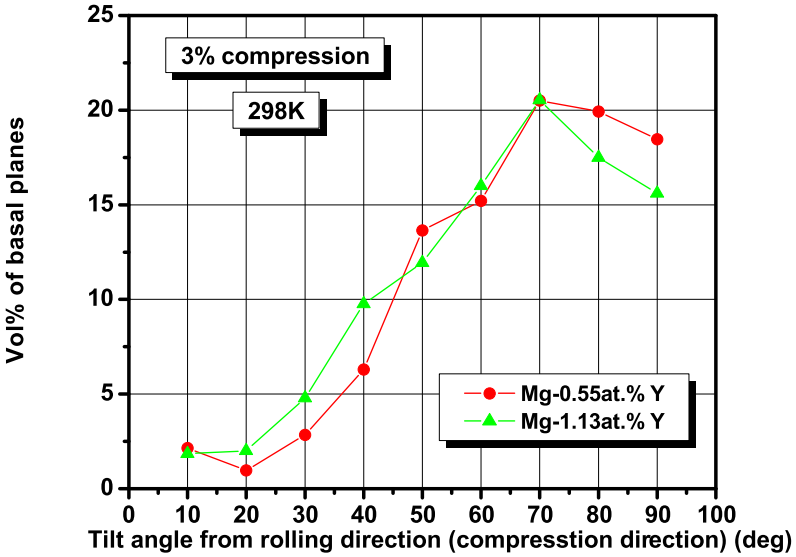

(a)

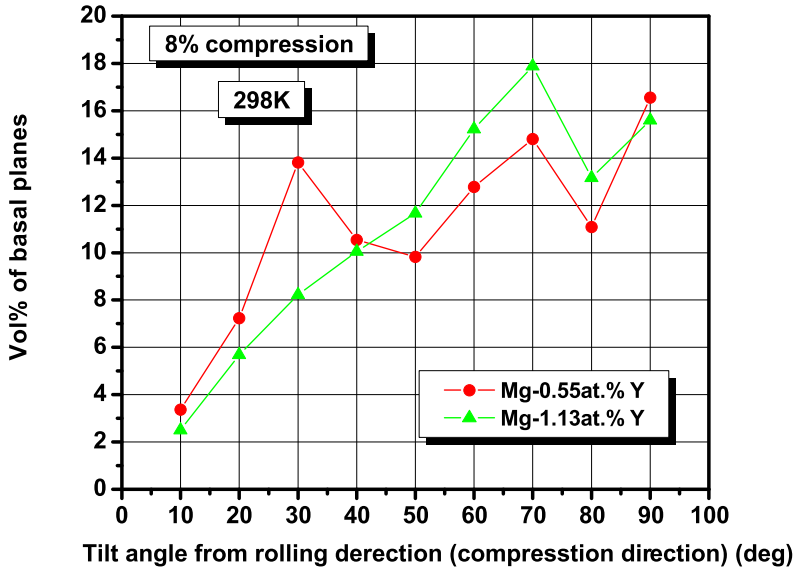

(b)

Figure 4.14: Volume percent of basal planes for Mg-0.55at. % Y and Mg-1.13at. %Y alloys at (a) 3% compression and (b) 8% compression as a function of tilt angle from rolling direction.

4.4 Analysis of Yield Asymmetry

Figure 4.15 shows the comparison of true stress-true strain characteristics of pure Mg and five Mg-Y alloys deformed under tension and compression at 298K. For pure Mg, the tension-compression yield asymmetry is very huge; both the yield stress and the flow stress exhibit substantial differences. With addition of Y, in Mg-0.30at. %Y alloy, the yield stress of tension and compression become similar and so does the flow stress at low strains. Both the yield stress and flow stress of tension and compression become more and more similar as the Y content increases. If we define the yield asymmetry as 1 - σ_{yC}/σ_{yT}, the yield asymmetry can be expressed quantitatively. From this definition, the yield asymmetries of pure Mg and five Mg-Y alloys are summarized in Table 4.6. It can be seen that the yield asymmetry of pure Mg, 0.843, is almost seven fold of the lowest yield asymmetry for Mg-Y alloys. All these results suggest that Y content reduces the tension - compression yield asymmetry. This behaviour is related to the crystallographic texture, which has a broader distribution of the basal planes of Mg-Y alloys than that of pure Mg. For a rolled sheet, most of the basal planes in the samples should be oriented parallel to the rolling direction. This kind of crystallographic texture induces different dominant deformation modes for tension and compression. In this case, both tensile stress and compressive stress are applied perpendicular to c-axis. It is known that when compressive stress is applied perpendicular to c-axis or tensile stress is applied along c-axis, the activation energy of twinning is much lower than slip, but not in the opposite loading direction. This means that twinning dominates the compression deformation and slip dominates the tensile deformation, while the activation stress of twinning is lower than that of slip. This is the reason why σ_{yC} of pure Mg is much lower than σ_{yT}. Y content broadens the distribution of basal planes, which decreases the twinning preference in compression deformation. So, the weakened texture

induced by Y content reduces the tension-compression yield asymmetry.

As mentioned in section 1.6, three main mechanisms of texture weakening induced by rare earth element have been proposed in previous studies: particle-simulated nucleation (PSN) of recrystallization (E.A.Ball & P.B.Prangnell, 1994; L.W.F.Machenzie *et al.*, 2007), recrystallization at shear bands (N.Stanford & M.R.Barnett., 2008; K.Hantzsche *et al.*, 2010) and grain boundary mobility (Bohlen *et al.*, 2007; L.W.F.Machenzie *et al.*, 2007; N.Stanford, 2010; S.A.Farzadfar *et al.*, 2011). Hantzsche et al., (K.Hantzsche *et al.*, 2010) found that texture can be weakened in Mg-Y alloys without any precipitation, indicating that PSN is not a significant texture weakening mechanism. The volume fraction of precipitation in the alloys is extremely small and the precipitates can be neglected as important structural elements. Therefore, it is concluded that PSN is not responsible for the texture weakening phenomenon. Barrett et al., (M.R.Barnett *et al.*, 2004) found that Mg-0.2Ce alloy, which has same volume fraction of shear bands as pure Mg, exhibits weaker cold rolling texture than pure Mg, suggesting that shear band recrystallization is also not responsible for texture weakening. Alternatively, it is hypothesized that the change of grain boundary mobility may be responsible for the texture weakening of Mg-Y alloys. Yttrium has large atoms with low diffusivity in solid solution with Mg. The existence of solute drag in Mg-Y alloys in this work has been proven by the strain rate test. It is known that solute drag has a strong effect on grain boundary mobility for different grain boundary orientations, which may induce a form of growth advantage of non-basal grains over basal ones. Therefore, it is speculated that texture weakening during recrystallization is attributed to the change of grain boundary mobility induced by Y solute drag. To confirm this theory, detailed study of the microstructure should be performed.

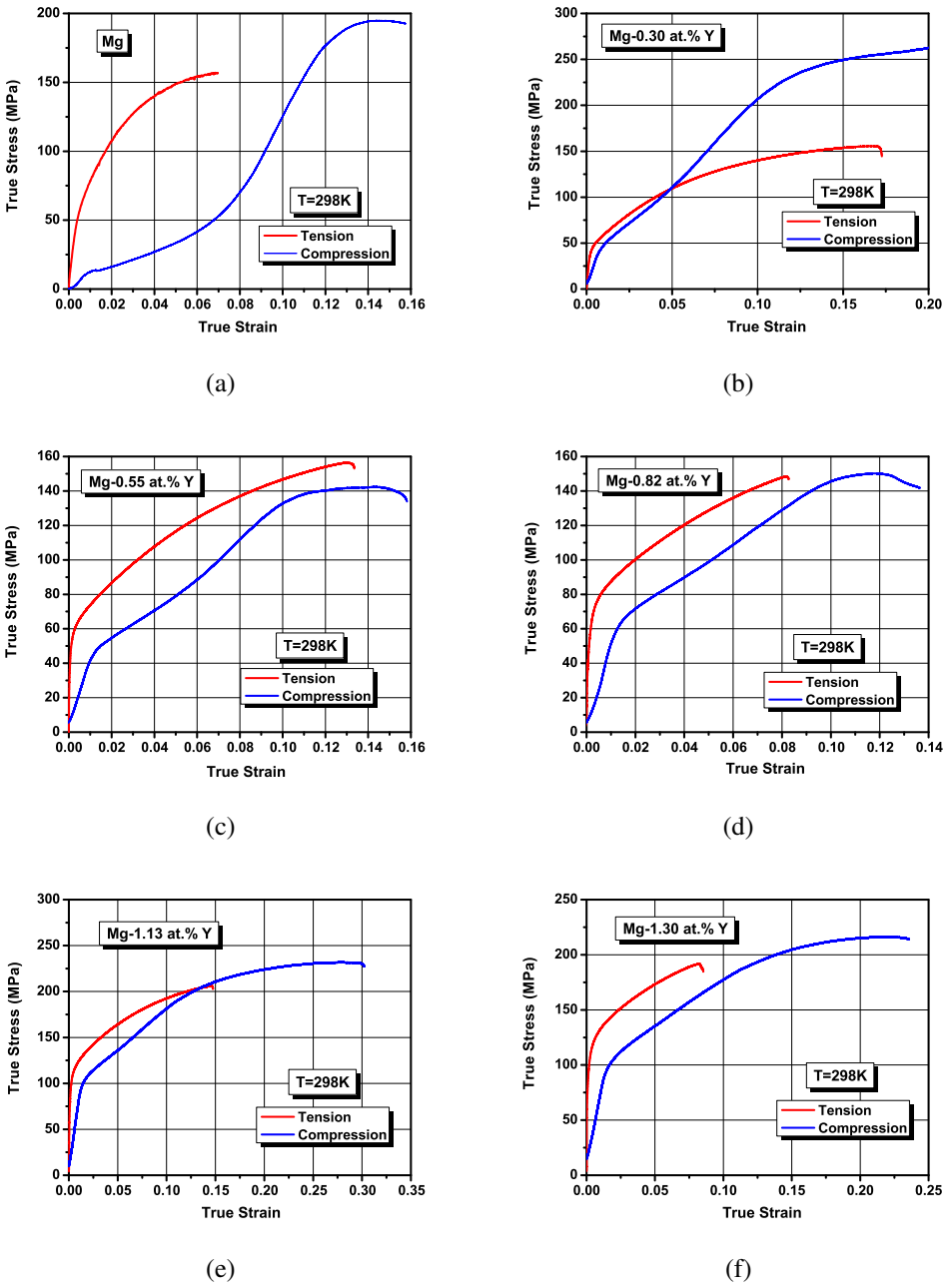

Figure 4.15: Comparison of true stress versus true strain characteristics of Mg-Y alloys deformed under tension and compression at 298K for different alloy compositions: (a) pure Mg, (b) Mg-0.30at. % Y, (c) Mg-0.55at. % Y, (d) Mg-0.82at. % Y, (e) Mg-1.13at. % Y, (f) Mg-1.30at. % Y.

Table 4.6: Yield asymmetry, 1 - σ_{yC}/σ_{yT}, of pure Mg and Mg-Y alloys.

Composition at.%	Yield asymmetry
Mg	0.843
0.30	0.227
0.55	0.241
0.82	0.181
1.13	0.126
1.30	0.145

Chapter 5

Summary and conclusions

Tension and compression experiments have been carried out on a series of Mg-Y alloys with Y content up to 1.30 at. %, in a range of temperatures between 4.2K and 298K to study the effect of Y on mechanical properties of these alloy systems. The focus was on understanding solid solution strengthening, work hardening behaviour, strain rate sensitivity, fracture surface and texture evolution and in general, the effect of temperature on mechanical properties.

The study on Mg-Y alloys revealed an anomalous change of ductility in the temperature range from 4K to 298K. The ductility of Mg-Y alloys deformed under tension and compression decreases when the deformation temperature decreases from 298K to 78K. While, the ductility at 4K is similar to 78K or a slightly higher than at 78K, but it is still lower than at 298K. It is known that the ductility of FCC materials increases with decreasing deformation temperature due to the enhanced work hardening capacity (Park & Niewczas, 2008; Isaev *et al.*, 2012). In this case, the ductility decreases as the temperature decreases. This is a completely different fundamental observation. In HCP materials, such as Mg alloys,

CRSS for prismatic and pyramidal slip systems increases rapidly as the temperature decreases from about 250K (A.Akhtar & E.Teghtsoonian, 1969a,b; Ward *et al.*, 1961; Hiura, 2008). Consequently, prismatic and pyramidal slip systems are suppressed at low temperature due to their high CRSS. Generally, only basal slip and twinning is available at low temperature, which lead to the decrease in ductility of the alloys.

For Mg-Y alloys deformed under tension and compression, higher flow stress, higher yield stress, higher work hardening and lower dynamic recovery were observed at lower deformation temperature. Additionally, for pure Mg deformed under tension, anomalous flow and yield stress behaviour were observed, which rely on the phenomenon that the flow stress is lower at 4K than that at 78K. This was also observed in Bhattacharya's studies on Mg single and polycrystals (B.Bhattacharya, 2006). Bhattacharya explained this anomalous flow stress behaviour due to enhanced activity of <c+a> slip system.

Large tension-compression yield asymmetry was observed in pure Mg deformed at 298K. Compared to pure Mg, the tension- compression yield asymmetry for Mg-Y alloys is reduced. The reduction of yield asymmetry is due to the weakened texture induced by Y content. Generally, it is known that when compressive stress is applied perpendicular to c-axis or tensile stress is applied along c-axis, activation of twinning is easier than slip. Due to the type of texture formed during the rolling procedure, twinning dominates the compression deformation and slip dominates the tensile deformation. The difference between activation stress for slip and twinning, which is lower for twinning, induces the yield asymmetry. Y content weakens the texture by broadening the distribution of basal planes, which decreases the twinning preference in compression deformation. As a result, the weakened texture induced by Y content reduces the tension-compression yield asymmetry.

The main results of this study are summarized as follows:

(1) After correcting for grain size strengthening effects, the yield strength scales with concentration of the solute as c^n, where c is the concentration of the solute in atomic percent and $n \sim 2/3$. The yield strength increases linearly with c^n. Comparing with the effect of Al, Zn and Gd, solid solution strengthening of Y is much stronger. The results suggest that in addition to the atomic size and modulus misfit effects, the valence effect and prismatic slip system strengthening may be responsible for the enhanced strengthening of Y in Mg. At room temperature, the hardness increases with the Y content as the relationship: $H_{v0.1}$ = 43.59 + 21.33 Y.

(2) Kocks-Mecking analysis reveals that the initial hardening rate, Θ_0 value, increases with both the increase of Y content and the decrease of deformation temperature, indicating that the ability of dislocation storage increases with increasing Y content and decreasing deformation temperature. In Lukác and Balík model, C values for alloys are much smaller than that of pure Mg and decrease with increasing Y content. The substitutional Y atoms inhibit the motion of dislocations. Therefore, dislocation annihilation process is retarded.

(3) Strain rate sensitivity measurements carried out under tension and compression reveal that Mg-Y alloys show decreasing ESRS with increasing Y content at 298K and exhibit a negative ESRS in highly concentrated alloys. The negative ESRS is attributed to the interaction between solute atoms and dislocations. At low temperatures the alloys show positive ESRS, increasing with Y content, suggesting that the solute atoms - dislocation interactions control the flow stress and deformation behaviour.

(4) In all cases, the activation volume decreases at the beginning of deformation from about $120b^3$ to about 30-40 b^3. The apparent activation volume shows strong dependence on solute atoms. The presence of Y content reduces the apparent activation volume. For

78K, in all cases, the activation distance decreases with the increase of Y solute content, suggesting that solute atoms reduce the activation distance of dislocations. For 4K, the activation distance is in the range 0.055b - 0.010b and it suggest that the tunnelling effects during thermally activated dislocation glide become the controlling mechanisms. For compression, activation distance exhibits temperature dependence. The activation distance at 78K is larger than at 4K.

(5) Fracture surface analysis reveals that the fracture mode shows dependence on deformation temperature. At 298K and 78K, the failure is a mixture of ductile and cleavage type which is dominated by ductile and cleavage, respectively. At 4K, failure occurs predominantly by cleavage fracture. The observations correlate well with the view that with the decrease of the deformation temperatures various glide and twinning modes in Mg-Y alloys are suppressed and this leads to the early failure by cleavage.

(6) Texture measurements reveal that the initial texture with c-axis perpendicular to deformation axis (rolling direction) is transformed to the twin texture with c-axis aligned parallel to compression axis after compression. After tension, c-axis is still perpendicular to tensile axis, while some texture components due to tensile twinning appear at about 90° rotated from the initial components. This has strong effect on the flow stress and work-hardening properties as discussed in section 4.1.2.

(7) The distribution of basal planes reveals that increasing Y content in alloys decreases the amount of basal component and enhances non-basal orientations. Y additions broaden the distribution of basal poles and retard the formation of basal texture. The weakened texture induced by Y content reduces the tension-compression yield asymmetry.

(8) Solute drag has a strong effect on grain boundary mobility of different grain boundary orientations, which may induce a form of growth advantage of non-basal grains over basal

ones. Therefore, it is speculated that texture weakening is attributed to the change of grain boundary mobility induced by Y solute drag.

Bibliography

A.Akhtar, & E.Teghtsoonian. 1969a. Solid solution strengthening of magnesium single crystals-I Alloying behaviour in basal slip. *Acta Metallurgica*, **17**, 1339–1349.

A.Akhtar, & E.Teghtsoonian. 1969b. Solid solution strengthening of magnesium single crystals-II The effect of solute on the ease of prismatic slip. *Acta Metallurgica*, **17**, 1351–1356.

A.A.Salem, S.R.Kalidindi, & R.D.Doherty. 2002. Strain hardening regimes and microstructure evolution during large strain compression of high purity titanium. *Scripta Materialia*, **46**, 419–423.

Ashby, M.F. 1970. The deformation of plastically non-homogeneous materials. *Phil. Mag.*, **21**, 399–424.

Basinski, Z.S., Szczerba, M.S., Niewczas, M., Embury, J.D., & Basinski, S.J. 1997. The transformation of slip dislocations during twinning of copper-aluminum alloy crystals. *Rev.Metall.*, **94**, 229.

B.Bhattacharya. 2006. Plastic deformation behavior of pure magnesium in the temperatre range 4.2K–300K. *PhD Thesis, McMaster University*.

Bohlen, Jan, R.Nurnberg, Marcus, W.Senn, Jeremy, Letzig, Dietmar, & R.Agnew, Sean. 2007. The texture and anisotropy of magnesiumzincrare earth alloy sheets. *Acta Materialia*, **55**, 2101–2112.

C.H.Cáceres, & A.Blake. 2002. The Strength of Concentrated MgZn Solid Solutions. *Phys.Stat.Sol.(a)*, **194**, 151–156.

C.H.Cáceres, & D.M.Rovera. 2001. Solid solution strengthing in concentrated Mg-Al alloys. *Journal of Light Metals*, **1**, 147–158.

C.H.Cáceres, P.Lukác, & A.Blake. 2008. Strain hardening due to$\{10\bar{1}2\}$ twinning in pure magnesium. *Philosophical Magazine*, **88**, 991–1003.

Chen, Kuiying, & P.Boyle, Kevin. Elastic properties, thermal expansion coefficients, and electronic structures of Mg and Mg-based alloys. *The Minerals, Metals & Materials Society and ASM International*.

Chen, Kuiying, & P.Boyle, Kevin. 2012. Alloy solid solution strengthening of Mg alloys: Valence effect. *Phys. Status Solidi B*, **249**(11), 2089–2095.

E.A.Ball, & P.B.Prangnell. 1994. Tensile-compressive yield asymmetry in high strength wrought magnesium alloys. *Scripta Metallurgica et Materialia*, **31**, 111–116.

Hauser, F.E., Landon, P.R., & Dorn, J.E. 1956. Fracture of magnesium alloys at low temperature. *AIME Trans*, **206**, 589–593.

Hiura, Fumiaki. 2008. Latent Hardening in Pure Magnesium Single Crystals. *Master Thesis, McMaster University*.

H.Mecking, & U.F.Kocks. 1981. Kinetics of flow and strain-hardening. *Acta Metallurgica*, **29**, 1965–1875.

Hosford, William F. 2009. *Mechanical behavior of materials*. Cambridge University Press.

Isaev, N. V., Zabrodin, P. A., Spuskanyuk, V. Z., Davydenko, A. A., & Pustovalov, V. V. 2012. Microstructure and low-temperature plastic deformation of AlLi alloy. *Low Temp. Phys.*, **38**, 80–87.

Kalidindi, S.R., Salem, A.A., & Doherty, R.D. 2003. Role of deformation twinning on strain hardening in cubic and hexagonal polycrystalline metals. *Adv.Eng.Mater*, **5**, 229–232.

Kaschner, G.C., Tomé, C.N., Beyerlein, I.J., Vogel, S.C., Brown, D.W., & McCabe, R.J. 2006. Role of twinning in the hardening response of zirconium during temperature reloads. *Acta Materialia*, **54**, 2887–2896.

K.Hantzsche, J.Bohlen, J.Wendt, K.U.Kainer, S.B.Yi, & D.Letzig. 2010. Eect of rare earth additions on microstructure and texture development of magnesium alloy sheets. *Scripta Materialia*, **63**, 725–730.

L.Gao, R.S.Chen, & E.H.Han. 2009a. Effects of rare-earth elements Gd and Y on the solid solution strengthening of Mg alloys. *Journal of Alloys and Compounds*, **481**, 379–384.

L.Gao, R.S.Chen, & E.H.Han. 2009b. Solid solution strengthening behaviors in binary Mg-Y single phase alloys. *Journal of Alloys and Compounds*, **472**, 234–240.

L.L.Rokhlin. 2003. *Magnesium Alloys Containing Rare Earth Metals: Structure and Properties*. Advances In Metallic Alloys, vol. 3. Taylor and Francis.

L.W.F.Machenzie, B.Davis, F.J.Humphreys, & G.W.Lorimer. 2007. *Materials Science and Technology*, **23**, 1173–1180.

M.R.Barnett, M.D.Nave, & C.J.Bettles. 2004. Deformation microstructures and textures of some sold rolled Mg alloys. *Materials Science and Engineering A*, **386**, 205–211.

N.F.Mott, & F.R.N.Nabarro. 1940. An attempt to estimate the degree of precipitation hardening, with a simple model. *Proc.Phys.Soc.Lond.*, **52**, 86–89.

Niewczas, M., Basinski, Z. S., Basinski, S. J., & D.Embury, J. 2001. Deformation of copper single crystals to large strains at 4.2K. *Philosophical Magazine A*, **81**, 1121–1142.

N.Stanford. 2010. Micro-alloying Mg with Y, Ce, Gd and La for texture modicationA comparative study. *Materials Science and Engineering A*, **527**, 2669–2677.

N.Stanford, & M.R.Barnett. 2008. The origin of rare earth texture development in extruded Mg-based alloys and its effect on tensile ductility. *Materials Science and Engineering A*, **496**, 399–408.

N.Stanford, & M.R.Barnett. 2013. Solute strengthening of prismatic slip, basal slip and $\{10\bar{1}2\}$ twinning in Mg and MgZn binary alloys. *International Journal of Plasticity*, http://dx.doi.org/10.1016/j.ijplas.2013.01.012.

Park, Dong-Yeob, & Niewczas, Marek. 2008. Plastic deformation of Al and AA5754 between 4.2K and 295K. *Materials Science and Engineering A*, **491**, 88–102.

P.Lukác, & J.Balík. 1994. Kinetics of Plastic Deformation. *Key Engineering Materials*, **97/98**, 307–322.

R.Labusch. 1970. A statistical theory of solid solution hardening. *Phys.Stat.Sol.*, **41**, 659–669.

R.L.Fleischer. 1961. Solution hardening. *Acta Metallurgica*, **9**, 996–1000.

R.L.Fleischer. 1963. Substitutional solution hardening. *Acta Metallurgica*, **11**, 203–209.

R.Muraliraja, H.Vettrivel, & Dr.R.Elansezhian. 2013. Synthesis and characterization of magnesium alloy added with Yttrium and to study the microstructure and mechanical properties. *International Journal of Engineering and Innovative Technology*, **2**, 338–392.

S.A.Farzadfar, M.Sanjari, amd E.Essadiqi, I.-H.Jung, & S.Yue. 2011. Role of yttrium in the microstructure and texture evolution of Mg. *Materials Science and Engineering A*, **528**, 6742–6753.

S.Sandlöbes, M.Friák, S.Zaefferer, A.Dick, S.Yi, D.Letzig, Z.Pei, L.F.Zhu, J.Neugebauer, & D.Raabe. 2012. The relation between ductility and stacking fault energies in Mg and Mg-Y alloys. *Acta Materialia*, **60**, 3011–3021.

Stanford, Nicole, Atwell, Dale, & R.Barnett, Matthew. 2010. The effect of Gd on the recrystallisation, texture and deformation behaviour of magnesium-based alloys. *Acta Materialia*, **58**, 6773–6783.

U.F.Kocks, & H.Mecking. 2003. Physics and phenomenology of strain hardening : the FCC case. *Progress in Materials Science*, **48**, 171–273.

Ward, P. Flynn, Mote, J., & Dorn, J.E. 1961. On the thermally activated mechanism of prismatic slip in Mg single crystals. *Trans. TMS-AIME*, **221**, 1148–1154.

W.Senn, Jeremy, & R.Agnew, Sean. 2008. Texture randomization of magnesium alloys containing rare earth elements. *Magnesium Technology*, 153–158.

Wu, Yurong, & Hu, Wangyu. 2008. Comparison of the solid solution properties of Mg-RE(Gd, Dy, Y) alloys with atomistic simulation. *Research Letters in Physics*, **2008**, 1–4.